

**A New Multiple Scattering Technique for X-Ray  
Photoelectron Diffraction**

A thesis submitted for the degree of  
Doctor of Philosophy  
at the University of Leicester

by

John Francis Hart  
Department of Physics and Astronomy  
University of Leicester

April 1997

UMI Number: U087379

All rights reserved

INFORMATION TO ALL USERS

The quality of this reproduction is dependent upon the quality of the copy submitted.

In the unlikely event that the author did not send a complete manuscript and there are missing pages, these will be noted. Also, if material had to be removed, a note will indicate the deletion.



UMI U087379

Published by ProQuest LLC 2013. Copyright in the Dissertation held by the Author.  
Microform Edition © ProQuest LLC.

All rights reserved. This work is protected against  
unauthorized copying under Title 17, United States Code.



ProQuest LLC  
789 East Eisenhower Parkway  
P.O. Box 1346  
Ann Arbor, MI 48106-1346

# A New Multiple Scattering Technique for X-Ray Photoelectron Diffraction

by

John Francis Hart

## Abstract

This thesis is concerned with the development and application of a new method of performing multiple scattering calculations of X-ray Photoelectron Diffraction (XPD) from periodic surfaces. The technique is based on the dynamical theory of Reflection High Energy Electron Diffraction (RHEED), allowing more efficient access to high photoelectron energies (1000eV and above) than is available using present calculational schemes. Convergence tests have been performed to identify the limitations of the present method.

The method is applied to two overlayer systems for which XPD experimental data is available,  $c(2 \times 2)\text{S}$  and  $c(2 \times 2)\text{O}$  on Ni(001). For the  $c(2 \times 2)\text{S}$  system, which is relatively well understood and therefore a good test system, data at four emission (take-off) angles is fitted, giving optimum agreement with the S atoms occupying hollow sites at a vertical adsorption height of between 1.30Å and 1.35Å. The agreement is improved slightly for the lowest two take-off angles by an outward relaxation in the top Ni-Ni layer spacing. Comparison is made with single scattering calculations for the system and the present method shown to be far superior at the lowest take-off angle. This clearly demonstrates the importance of multiple scattering at grazing emission angles.

For the  $c(2 \times 2)\text{O}$  system, data at two take-off angles is fitted giving optimum agreement with the O atoms in hollow sites at an adsorption height of 0.75Å. By allowing a small outward relaxation in the top Ni-Ni layer spacing, an almost equally good fit to the data is found at an adsorption height of 0.80Å. An off-centre bonding site which has been proposed, in which the O atoms are displaced from their hollow sites by 0.3Å in the [110] direction has been considered and ruled out.

# Contents

<b>List of Figures</b>	<b>ix</b>
<b>List of Tables</b>	<b>x</b>
<b>Acknowledgements</b>	<b>xi</b>
<b>1 Introduction</b>	<b>1</b>
1.1 Surface Science . . . . .	2
1.2 Photoelectron Diffraction . . . . .	3
1.3 X-Ray Photoelectron Diffraction (XPD) . . . . .	7
1.4 Structure of the Thesis . . . . .	9
<b>2 X-Ray Photoelectron Diffraction</b>	<b>12</b>
2.1 Experimental Arrangement . . . . .	13
2.2 Forward Scattering . . . . .	14
2.3 Current XPD Computational Schemes . . . . .	17
2.3.1 Single Scattering Calculations . . . . .	17
2.3.2 Multiple Scattering Calculations . . . . .	20
2.4 A New Multiple Scattering Scheme for XPD . . . . .	22
2.4.1 The XPD Pattern . . . . .	22
2.4.2 Wave Functions . . . . .	26

<i>Contents</i>	iii
2.4.3 Calculation of Matrix Elements . . . . .	28
2.4.4 Finite Angular Resolution . . . . .	35
<b>3 Multiple Scattering Theory and Application to XPD</b>	<b>38</b>
3.1 Multiple Scattering Theory of RHEED . . . . .	39
3.1.1 Introduction . . . . .	39
3.1.2 The Scattering Potential . . . . .	41
3.1.3 The Scattering Matrix . . . . .	43
3.1.4 The Layer Doubling Method . . . . .	47
3.2 Application to XPD Calculations . . . . .	50
3.2.1 The RHEED Computer Program . . . . .	50
3.2.2 Matrix Element Integrals (i): A Simplified Case . . . . .	52
3.2.3 Matrix Element Integrals (ii): Realistic Case . . . . .	56
3.2.4 The XPD Calculation . . . . .	60
<b>4 Initial Calculations</b>	<b>62</b>
4.1 The Doyle-Turner Potential . . . . .	63
4.2 Convergence . . . . .	65
4.2.1 Ni(001)c(2 × 2)O . . . . .	68
4.2.2 Si(111)-√3 × √3 Sb . . . . .	70
4.2.3 Discussion . . . . .	72
<b>5 Application to Ni(001)c(2 × 2)S</b>	<b>74</b>
5.1 Comparison of Theory with Experiment . . . . .	75
5.1.1 Normalisation . . . . .	75
5.1.2 Reliability Factors . . . . .	76
5.2 Ni(001)c(2 × 2)S . . . . .	77

<i>Contents</i>	iv
5.2.1 An Experimental XPD Study . . . . .	79
5.3 Calculations . . . . .	80
5.3.1 Non-Structural Parameters . . . . .	81
5.3.2 Adsorption Height . . . . .	82
5.3.3 Adsorption Site . . . . .	91
5.3.4 Substrate Relaxation . . . . .	92
5.3.5 Comparison with Single Scattering Theory . . . . .	96
<b>6 A Study of Ni(001)<math>c(2 \times 2)</math>O</b>	<b>101</b>
6.1 Introduction . . . . .	101
6.2 The Ni(001) $c(2 \times 2)$ O Surface . . . . .	102
6.2.1 Problems . . . . .	102
6.2.2 Proposed Models . . . . .	103
6.2.3 XPD Studies . . . . .	105
6.3 Calculations . . . . .	106
6.3.1 Hollow-Site Calculations . . . . .	106
6.3.2 The Pseudobridge Site . . . . .	112
6.3.3 Substrate Relaxation . . . . .	116
6.4 Discussion . . . . .	118
<b>7 Summary and Conclusions</b>	<b>120</b>
<b>A Evaluation of Integral <math>\mathcal{I}</math></b>	<b>126</b>

## List of Figures

1.1	The low and high energy modes of photoelectron diffraction. Diagram (a) is for a low energy photoelectron emitted from the adatom, where backscattering from the substrate is utilised. Diagram (b) is for a high energy photoelectron. In this case near-forward scattering is the dominant mechanism and hence diffraction may only be seen at shallow emission angles relative to the substrate. (From Woodruff [29]) . . . . .	6
2.1	The experimental arrangement for photoelectron diffraction. For angle scans the photoelectron intensity is monitored as $\theta$ or $\phi$ is varied at a fixed $h\nu$ . For energy scans, the geometry is fixed and $h\nu$ is varied. . . . .	14
2.2	A model calculation to demonstrate the "forward focussing" of high energy photoelectrons. A 1000eV photoelectron is emitted from one Cu atom, part of which scatters from the other (upper diagram). Observed intensity is plotted as a function of scattering angle $\Theta$ (lower diagram), showing interference fringes and a forward focussing peak along the interatomic axis. . . . .	16
2.3	The polarisation vector, positioned in the $y'-z'$ plane of system $(x',y',z')$ by the angle $\beta$ . . . . .	25

2.4 Averaging to simulate the finite angular resolution of the experiment. The circles represent calculated points on a  $\theta$ - $\phi$  grid separated by  $1^\circ$  in each direction, with the shaded circle being the point of interest. High resolution experimental data is simulated by averaging points within the  $\pm 1^\circ$  square, while lower resolution data uses points within the  $\pm 2^\circ$  square. . . . . 37

3.1 Schematic diagram of the wave amplitudes entering and leaving a layer. The vectors **I** and **R** are composed of the amplitudes  $Q_{\kappa}^-(z_t)$  and  $Q_{\kappa}^+(z_t)$  respectively, and **X** and **T** are composed of  $Q_{\kappa}^+(z_b)$  and  $Q_{\kappa}^-(z_b)$ . . . . . 45

3.2 Schematic diagram of the layer doubling method. The scattering matrices for the  $\alpha$  and  $\beta$  sections are calculated separately. The layer doubling algorithm is then used to find the composite  $\alpha\beta$  scattering matrix. . . . . 49

3.3 Determination of the waves entering and leaving the surface and bulk layers using the surface (superscript s) and bulk (superscript b) scattering matrices. To calculate the integrals involving the  $\phi_{\kappa}(z)$  over the surface layer, the waves leaving the layer must be known. The surface region is shown in two parts to highlight the contribution of the backscattering from the bulk region. Matrix **X** is defined in Eq. (3.33) . . . . . 55

3.4 The division of the surface integration range into three segments for a general beam set. The superscripts on the scattering matrices indicate the segment they represent. The matrix element integrals are performed in segment (b), so the important quantities are the waves leaving (b). The matrices  $M, M', M'', X, X'$  and  $X''$  are defined in Eq. (3.37). . . . . 58

4.1	Comparison between a calculated potential of a 1100eV electron in a Cu atom (solid line) including exchange and correlation effects, and the analytic form given by the Doyle-Turner expression in Eq. (4.2), (line with diamonds). . . . .	65
4.2	The exchange and correlation contribution to the potential plotted for different electron energies. The Hartree potential, which is the classical electrostatic potential and is energy independent, is shown for reference. . . . .	66
4.3	Calculated XPD intensities from the O 1s core level of $c(2 \times 2)O/Ni(001)$ for various different beam sets. Calculations at the three azimuthal angles shown can all be seen to converge to asymptotic values for large beam sets. (Photoelectron energy=954eV) . . . . .	69
4.4	Calculated XPD intensities from the Sb 3d core level of $(\sqrt{3} \times \sqrt{3})Sb/Si(111)$ for various different beam sets. Calculations at the two azimuths shown can be seen to converge for large beam sets. (Photoelectron energy=738eV) . . . . .	71
5.1	Schematic diagram showing adsorbates well above the substrate. The angles involved with scattering from the substrate can be seen to be much greater than for scattering within the adlayer. The substrate signal is therefore much weaker. . . . .	80
5.2	Theoretical XPD curves (solid lines) for different adsorption heights of the $c(2 \times 2)S$ overlayer on a bulk terminated Ni(001) substrate at take-off angle $\theta = 6^\circ$ . Experimental data is from ref. [18]. . . . .	84
5.3	Same as Fig. 5.2 but for take-off angle $\theta = 10^\circ$ . . . . .	85
5.4	Same as Fig. 5.2 but for take-off angle $\theta = 12^\circ$ . . . . .	86
5.5	Same as Fig. 5.2 but for take-off angle $\theta = 16^\circ$ . . . . .	87

5.6 Reliability factors R1 - R5 for calculations on Ni(001)c(2×2)S. Points on each curve are the average R-factor for the four take-off angles. The curves indicate that the an overlayer height of 1.30Å-1.35Å gives best agreement with the data. Note the multiplying factors which have been used to display all five curves on the same range as R2 . . . . . 90

5.7 The three different bonding sites for which calculations have been performed. Large circles represent the top layer of Ni(001). Position (a) is the hollow site, (b) the bridge site and (c) the on top site. . . . . 92

5.8 Results of a calculation at a fixed adsorption height of 1.35Å, for three different adsorption sites. The solid lines are calculated curves, the dotted lines the same set of experimental data. The values of R1 are shown for each site as an indication of the agreement. . . . . 93

5.9 Summed R1 factors using calculations at  $\theta = 6^\circ$  and  $\theta = 10^\circ$ , for various adsorption heights. The solid line is with  $d_{12}$  having the bulk spacing of 1.76Å and the broken line is with  $d_{12}$  relaxed to 1.86Å. The arrow at 1.30Å indicates the minimum of both curves. . . . . 95

5.10 The best fit single scattering (SS) calculation of Saiki, and the best fit multiple scattering (MS) calculation using the present method at take-off angle  $\theta = 10^\circ$ . Solid lines are the calculated curves, the dotted lines the same set of experimental data. . . . . 97

5.11 The best fit single scattering (SS) calculation of Saiki, and the best fit multiple scattering (MS) calculation using the present method at take-off angle  $\theta = 6^\circ$ . Solid lines are the calculated curves, the dotted lines the same set of experimental data. The MS calculation can be seen to be a far superior fit to the data than the SS calculation, resulting a significantly lower value of R1. . . . . 98

6.1	Theoretical XPD curves (solid lines) for different adsorption heights of the $c(2 \times 2)$ O overlayer on a bulk terminated Ni(001) substrate at take-off angle $\theta = 8^\circ$ . Experimental data (broken line) is from ref. [31] . . . . .	107
6.2	Same as Fig. 6.1 but for take-off angle $\theta = 11^\circ$ . . . . .	108
6.3	The R1 analysis of the calculations in Figs. 6.1 and 6.2 . . . . .	111
6.4	Schematic diagram of the pseudobridge geometry proposed by Demuth <i>et al.</i> [83]. The O atom (filled circle) is displaced from the hollow site by $0.30\text{\AA}$ in the $[110]$ direction. . . . .	112
6.5	Theoretical XPD curves (solid lines) for different adsorption heights of the $c(2 \times 2)$ O overlayer, with the O atoms occupying the pseudobridge sites as shown in Fig. 6.4. The take-off angle is $8^\circ$ . . . . .	113
6.6	Same as Fig. 6.5, but at a take-off angle of $11^\circ$ . . . . .	114
6.7	The R1 analysis of the calculations in Figs. 6.5 and 6.6. The best pseudobridge site is at $0.85\text{\AA}$ , but has a far higher minimum R1 compared with the hollow site. . . . .	116
6.8	R1 curves for $d_{12}=1.76\text{\AA}$ (bulk value) and $d_{12}=1.86\text{\AA}$ (5.7% expansion). Both are for the O atoms occupying hollow sites. The two curves have approximately the same minimum R1, occurring at different $z$ values . . . . .	117

## List of Tables

2.1	The first few spherical harmonics $Y_{lm}(\theta, \phi)$ and the corresponding $\mathcal{Y}_{lm}(\hat{x}, \hat{y}, z)$ . The $\mathcal{Y}_{lm}(\hat{x}, \hat{y}, z)$ are the quantities $r^l Y_{lm}(\theta, \phi)$ in a Cartesian representation, with $x$ and $y$ replaced by the differential operators $\hat{x}$ and $\hat{y}$ . . . . .	33
-----	---	----

## Acknowledgements

I would like to express my thanks to all members of the theory group at Leicester for making my time here so enjoyable, and to my family for their support throughout my education. I also wish to thank the University of Leicester for the provision of a scholarship and JSPS for the award of a research fellowship. The warm hospitality of Professor Shozo Kono and the members of his group at the Research Institute for Scientific Measurements at Sendai, Japan is also greatly appreciated. Special thanks are due to Professor John Beeby for his excellent supervision during the course of this work, and to Dr. Peter Maksym for the use of his RHEED computer program and for many useful discussions.

## Chapter 1

### Introduction

During the last thirty years, the enormous interest in surface science, due in large measure to the many practical applications, has led to the the development of experimental techniques to study atomic arrangement at surfaces. Numerous such techniques utilise electrons in some way: low energy electron diffraction (LEED), reflection high energy electron diffraction (RHEED), photoelectron diffraction and Auger electron diffraction to name but a few. The interaction between electrons and the atoms of a crystal is much stronger than that of X-rays and neutrons, meaning that electrons are far more likely to undergo multiple scattering events, and that they have a much shorter inelastic mean free path. Electrons are therefore an excellent surface probe, but the consequence of using them is that a multiple scattering theory is often needed to analyse experimental data. This thesis is concerned with the surface technique of X-ray photoelectron diffraction, in which relatively high energy photoelectrons (500-1500eV) are used. A full multiple scattering theoretical treatment will be developed which is based on RHEED theory. This is a rather different approach compared to current multiple scattering methods which tend to be based on methods suitable for low energy electrons.

## 1.1 Surface Science

As already noted, the study of surfaces, defined as the top few atomic layers of a solid, has become a hugely important area of research in both physics and chemistry. Many physical properties of solids can be understood because, in the bulk, solids are essentially periodic in the three spatial dimensions. The formation of a surface breaks this periodicity resulting in changes of geometric and electronic structure there. The arrangement of atoms at the surface is, in general, not what would be expected by an abrupt termination of the bulk lattice. The surface atoms may relax outwards or inwards, or may rearrange themselves in the plane of the surface in order to minimise their energy. Indeed most semiconductor surfaces display some form of atomic reconstruction in an attempt to satisfy their dangling bonds. The formation of a surface and the subsequent rearrangement of atoms results in strong modifications of the electronic structure in this vicinity. Localised surface states are created which lie in forbidden bulk energy bands, and electrons in these states are trapped in the surface region.

As well as these fundamental reasons for studying surfaces, many technological applications depend on the use of solid surfaces, and could be improved with a better understanding of the role played by the surface. Understanding heterogeneous catalysis is a commonly cited reason for surface research. Certain chemical reactions display marked increases in reaction rate when in the presence of a solid surface. Furthermore, the pre-adsorption of certain species on the surface can promote or poison the catalytic reaction. Thermionic emission provides another technological application. When a metal is heated, conduction band electrons may be ejected from the surface. The effect is used in many electrical devices, and provides the source of electrons in cathode ray tubes.

Surfaces also play an important role in the manufacture and operation of semiconductor devices. Fabrication is performed by the epitaxial growth of one material onto another. The operation of such devices depends crucially upon electronic properties across the various interfaces, for example at the junction of  $p$ -type and  $n$ -type semiconducting layers or at the junction between a semiconducting material and a metallic contact. An understanding of the electronic structure and growth modes at surfaces is therefore essential to the design and fabrication of these components. The applications mentioned here and others, along with other aspects of surface science in general have been discussed by Prutton [1].

## 1.2 Photoelectron Diffraction

A variety of techniques have been developed which give information about the atomic structure of surfaces. These can be divided into three categories: techniques which probe the real-space lattice such as Field Ion Microscopy (FIM) and Scanning Tunneling Microscopy (STM), diffraction techniques (LEED, RHEED, Surface X-Ray Diffraction) which probe the reciprocal lattice, and techniques which give indirect information about atomic structure. Methods which fall into this final category include Surface X-ray Absorption Fine Structure (SEXAFS), Auger electron diffraction and photoelectron diffraction, a technique which will be discussed in more detail.

When a sample is illuminated with electromagnetic radiation, a core level electron may be photoemitted from a surface atom. Interference can be observed between the directly emitted component of the photoelectron wave field and the components which are scattered elastically from the surrounding atoms. This

produces variations in the photoemitted signal when measured either as a function of emission angle or of energy, and analysis of the signal can give information about the local atomic environment of the emitting atom. The surface sensitivity of the technique comes from the relatively short inelastic mean free path of electrons, which from a universal curve such as in ref. [2] is found to be between 5-15Å for 50-1000eV electrons. Therefore, although the incident radiation may create photoelectrons deep within the structure, only those created close to the surface will escape and contribute to the elastic signal. The remainder undergo an inelastic scattering event at some point and are absorbed by the crystal or are emitted with a reduced energy to form part of the inelastic background.

The idea that the variations in the photoelectron signal from adsorbed atoms could be used to determine surface structure was first proposed in a theoretical paper by Leibsch published in 1974 [3], although strong diffraction effects had been observed from single crystal substrates some years earlier. Verification of Leibsch's ideas came in 1978, with the publication of the first sets of adsorbate photoelectron diffraction experimental data. Woodruff *et al.* [4] demonstrated the angular dependence of Na 2p photoemission signal (kinetic energy 46eV) from Na adsorbed on Ni(001), Kono *et al.* [5] showed the angular dependence of the O 1s signal (kinetic energy 951eV) from O adsorbed on Cu(001), while Kevan *et al.* [6] measured the variation of the Se 3d signal from Se adsorbed on Ni(001) as a function of photoelectron energy.

Since these first quantitative measurements, photoelectron diffraction has become an accepted method in quantitative surface structural analysis. The technique has been used to study ordered overlayer systems [14-22], and also to study disordered adsorbate species [7-11]. The latter application is one of the

strengths of photoelectron diffraction: conventional diffraction techniques such as LEED require long range order in the structure parallel to the surface, whereas photoelectron diffraction, being a local structural technique does not require this. There are several other advantages of photoelectron diffraction. The technique is element specific, as core level binding energies are characteristic of the emitter species. This allows each different element present to be studied separately. With enough energy resolution, core binding energy shifts can be used to independently study atoms of the same element in different chemical states. Such a study was recently performed by Weiss *et al.* [11]. In a similar way, energy level splitting in magnetic atoms allows the diffraction patterns of photoelectrons with different spins to be studied separately, a method termed spin polarised photoelectron diffraction [23].

The experiments mentioned above which first demonstrated photoelectron diffraction [4, 5, 6] were conducted rather differently. The methods employed by Woodruff and Kevan, although different in that Woodruff measured the angular photoelectron dependence and Kevan the energy dependence, both utilise photoelectrons in the low energy range of roughly less than 200eV. The measurements of Kono used a much higher photoelectron energy of 951eV. The physics involved with low and high energy photoelectron diffraction is rather different, and the two have developed into distinct experimental techniques. Low energy experiments are based on the fact that electrons below about 200eV have a relatively large cross-section for backscattering. Hence if a photoelectron is emitted from an adsorbate above the surface, components of the wave field will be backscattered from substrate atoms allowing the desired interference with the direct wave to be observed. Experiments utilising backscattering are

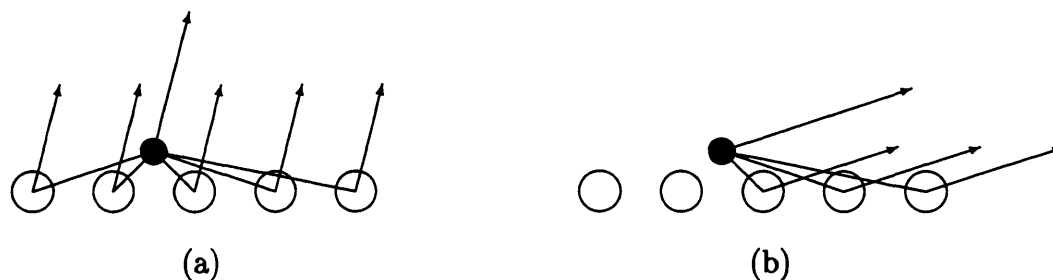


Figure 1.1: The low and high energy modes of photoelectron diffraction. Diagram (a) is for a low energy photoelectron emitted from the adatom, where backscattering from the substrate is utilised. Diagram (b) is for a high energy photoelectron. In this case near-forward scattering is the dominant mechanism and hence diffraction may only be seen at shallow emission angles relative to the substrate. (From Woodruff [29])

generally performed in the LEED-like geometry shown in Fig. 1.1(a). The alternative technique is to use high energy photoelectrons of around 500-1500eV. For electrons of such energy, atomic scattering is strongly focussed in the forward direction, within a cone with half angle of approximately  $30^\circ$ . For a high energy photoelectron emitted from an adsorbed atom, components of the wave field scattered from the substrate are large only at grazing angles with respect to the surface, giving an experimental geometry similar to RHEED. This is illustrated in Fig. 1.1(b). Excellent reviews of the low and high energy modes of photoelectron diffraction have been published by Woodruff [30] and by Fadley [31] respectively.

The general method of determining a structure by these two methods of photoelectron diffraction is similar to that used in LEED. Trial structures are taken, and their photoemission signals predicted by performing a scattering calculation. The calculations are quantitatively compared with experimental data to find the structure for which the calculation best agrees with the data. Recently it has been proposed that a full hemispherical photoelectron diffraction pattern

can be thought of as a photoelectron hologram, the interference pattern between a reference wave (the direct component) and scattered object waves (scattered waves from surrounding atoms) [33]. Much current work, especially at high photoelectron energies, is concerned with finding mathematical reconstruction schemes (closely related to Fourier transformation) to directly give the real-space atomic co-ordinates, thereby removing the need to perform trial-and-error scattering calculations [34].

### 1.3 X-Ray Photoelectron Diffraction (XPD)

The high energy mode of photoelectron diffraction, which is the subject of this thesis, is usually called X-ray photoelectron diffraction (XPD) because laboratory soft X-ray sources are normally used to create the photoelectrons. One of the advantages of using high energy photoelectrons is the relatively simple first order theoretical interpretation. Some features can be directly interpreted qualitatively: when other atoms lie above the emitter, the strong forward nature of the scattering from them can produce what have been called "forward focussing" peaks, large experimental peaks in emitter-scatterer bond directions. Simple geometric considerations then allow some information about the emitter-scatterer registry to be derived.

For adsorbate systems, the emitting atoms usually lie above the surface, and the forward scattering features tend to be directed along or into the surface and cannot be observed. There have been numerous studies of such overlayer systems using grazing emission XPD over recent years [14-19], and analysis of such data requires comparison with a scattering calculation. The higher energies involved with XPD means that some progress can be made with a single scattering theory:

the wave function of the photoelectron in the far field is taken to be composed of an unscattered wave, and a number of waves which propagate to a neighbouring atom before being scattered into the same direction as the unscattered wave. A more detailed description of this approach can be found in chapter 2. The single scattering theoretical approach has proved to be quite successful in describing experimental data for many systems, and was assumed to be generally valid for photoelectrons approaching the 1000eV range. Recently however, experiments have been performed which cannot be reconciled by a single scattering treatment [14, 16, 36, 37] at energies where single scattering was previously assumed to be applicable. Complicated multiple scattering calculations are required to analyse such data.

Several multiple scattering schemes have been developed for XPD [24-27], a topic which is also discussed in greater depth in the next chapter. Precise details of the calculational schemes vary from author to author, but a common feature of them is that atomic scattering of the photoelectron is described by phase shifts of a partial wave expansion of the photoelectron wave function. This kind of approach requires only a few phase shifts at low energies but requires more as the energy is increased. The computational time required for calculations of this type scales approximately as  $l^4$ , where  $l$  is the number of phase shifts included [26]. As XPD naturally involves high energies, such calculations tend to require great computational effort because of the  $l^4$  scaling. Approximations have been introduced in some cases [26] to reduce the size of the calculations at energies greater than around 500eV.

The aim of the present work is to develop an alternative approach to XPD multiple scattering calculations, which is hoped could be particularly useful for

relatively high energy photoelectrons of approximately 1000eV and above. The method is based on RHEED theory, in which the wave function is expanded in plane waves rather than spherical waves, and is suitable for periodic surfaces only. This approach provides an economical solution in the RHEED energy range of about 10keV and above. The XPD energy range of roughly 500-1500eV lies inbetween the low and high energy limits, making calculations based on either limiting expansion more complicated. Although the lower end of this energy range will be inaccessible using a plane wave expansion, it is expected that the method will be quite suitable for higher energies of about 1000eV and above. The XPD calculations based on RHEED theory will be more computationally demanding at around 1000eV than at typical RHEED energies, but they are expected to be significantly less demanding than the spherical wave approach at the same energy. Hence the possibility of more efficient and accurate analysis of XPD data in the high energy range.

#### 1.4 Structure of the Thesis

In the next chapter, a brief review of current theoretical techniques is given, including single scattering and multiple scattering methods. The theoretical framework for the new XPD scheme is then set up, the required formulae being derived from dipole transitions to a dynamical final state which is obtained from a RHEED computer program.

The first part of chapter 3 is devoted to the multiple scattering theory of RHEED. A detailed description of the 2-D Bloch wave approach of Maksym and Beeby will be presented, introducing the concepts of slicing a crystal into layers parallel to the surface and the scattering properties of each being represented by a

scattering matrix. The second part of the chapter is concerned with extracting the quantities from the RHEED computer code required to perform the numerical matrix element integrations derived in chapter 2. A practical problem in the numerical integration is encountered, stemming from the need to retain numerical accuracy when dealing with rapidly decaying exponential terms. A method for overcoming this problem is presented.

In chapter 4, some practical questions regarding the XPD calculation are addressed. The calculation is based on a RHEED wave function which converges quickly at electron energies of about 10keV and above. It is therefore important to determine how quickly the calculation converges in the 1000eV energy range. This is done by performing convergence calculations for two systems, one at 738eV in the lower part of the XPD range, and one at a higher energy of 954eV. The validity of using the high energy potential of RHEED in the XPD energy range is also investigated.

The XPD program is applied to a real system in chapter 5. The Ni(001)c(2×2)S surface has been studied at length in the literature and its structure is quite accurately known. An experimental XPD study had yielded a set of high resolution data, thus providing an excellent opportunity to test the theory. Comparison between the theory and experimental data is provided by an R-factor analysis. This also allows a comparison with the single scattering calculations published with the data.

In chapter 6, the program is applied to a somewhat less accurately known adsorption system. Ni(001)c(2×2)O surface has been studied extensively in the literature however there remains some controversy as to the bonding site and the height of the adlayer. Calculations are presented which investigate

the adsorption height of the overlayer, a proposed asymmetric bonding site and relaxation in the top Ni-Ni layer spacing by quantitative comparison with XPD data from the literature.

## Chapter 2

# X-Ray Photoelectron Diffraction

In this chapter, a new method for performing XPD calculations from periodic surfaces will be developed. It has been explained in the previous chapter how single scattering theoretical models have failed to account for certain experimental results due to multiple scattering of the photoelectron. Computer programs have been developed to account for multiple scattering, but tend to be based on theoretical techniques suitable for low energy electrons, and require large amounts of memory and CPU time when applied to XPD energies of  $>500\text{eV}$ . The present method is based on the multiple scattering theory of RHEED, and provides a way of performing more efficient calculations in the upper XPD range of around  $1000\text{eV}$ .

The photoelectron diffraction experiment will be described first, allowing some angles to be defined which will be required in the later derivations. Some features of XPD introduced in chapter 1 will then be expanded upon. Existing theoretical methods, including both single and multiple scattering procedures will be quickly reviewed and the new method then described in detail.

## 2.1 Experimental Arrangement

Any photoelectron diffraction experiment involves illuminating a sample with electromagnetic radiation and monitoring the resulting photoelectron flux as a function of emission angle or energy. The schematic arrangement of a photoelectron diffraction experiment is shown in Fig. 2.1. Several angles have been indicated, which will be required later in the chapter. A cartesian coordinate system has been defined with the surface lying in the  $x$ - $y$  plane. The angles  $\theta$  and  $\phi$  define the direction of observation: the azimuthal angle  $\phi$  is measured from the  $x$ -axis, and polar angle  $\theta$  measured from the  $x$ - $y$  plane. The polar angle defined like this is sometimes referred to as the "take-off" angle. Angle  $\alpha$  is defined to be the angle the incident radiation beam makes with the surface. The polarisation vector of the radiation, which lies in a plane normal to the direction of propagation, has also been indicated. The directions of X-ray incidence and electron emission have been shown in the same plane in Fig. 2.1 in order to coincide with experiments considered in forthcoming chapters. This may not be the case in general, but these incidence and exit directions are fixed with respect to one another and angles  $\theta$ ,  $\phi$  (and consequently  $\alpha$ ) adjusted by rotating the sample.

A synchrotron radiation source is usually required to access low photoelectron kinetic energies (about 200eV and below) for backscattering experiments. The experiment then can be performed in scanned angle and scanned energy modes. In scanned angle mode, the photon energy is fixed and photoelectron signal monitored as a function of  $\theta$  or  $\phi$ . Alternatively, scanned energy mode can be used where the experimental geometry is fixed and the incident photon energy  $h\nu$  varied. In this case the photoelectron signal is measured as a function of final

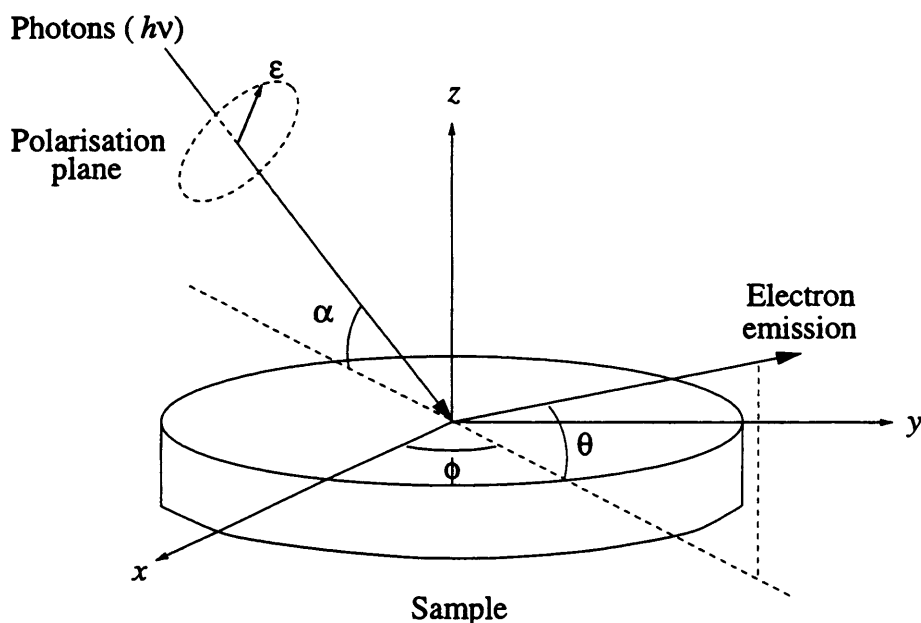


Figure 2.1: The experimental arrangement for photoelectron diffraction. For angle scans the photoelectron intensity is monitored as  $\theta$  or  $\phi$  is varied at a fixed  $h\nu$ . For energy scans, the geometry is fixed and  $h\nu$  is varied.

kinetic energy. XPD experiments are usually performed using laboratory sources of soft X-rays, removing the need for synchrotron radiation. The photon energy is then fixed, and the experiment is performed in scanned angle mode.

## 2.2 Forward Scattering

A feature which is sometimes seen in XPD experimental data is a forward focussing peak, and is one of the more directly interpretable features of XPD [12, 32]. The effect is caused by the strong forward nature of the scattering at energies greater than about 500eV, and can be demonstrated by means of a simple model calculation. Consider two isolated Cu atoms taken to be separated by  $5\text{\AA}$ . A high energy photoelectron (1000eV) represented by a spherical wave, is emitted from one of the atoms. Part of the outgoing wave encounters the other Cu atom

and scatters from it, while part remains unscattered. The angular distribution of the scattering is determined by the scattering factor, which for this calculation has been taken from the tables in [28]. The scattered and unscattered components are then allowed to interfere, and the intensity calculated as a function of scattering angle. The situation is illustrated in Fig. 2.2, and the results of the calculation plotted. Clear interference fringes are seen, but the most striking feature is the large peak centered at a scattering angle of  $0^\circ$ , the interatomic direction. This is the forward focussing peak.

Forward focussing peaks are most readily seen in XPD data when the emitting atom lies below the outermost layer, such as in an overlayer consisting of more than one atomic layer. A photoelectron created in a lower layer will scatter from an atom (or chain of atoms) above it giving rise to a peak in that direction, as seen in the earlier example. Identification of forward focussing features, which are usually found at relatively high take-off angles, allows information regarding emitter-scatterer bond directions to be derived directly by simple geometric considerations. For example, the effect has been used to study the tilt angle of CO adsorbed on Ni(001) [13].

A common use of XPD is to investigate sub-monolayer adsorption systems with a view to identifying the adsorption site of the foreign species [12, 15, 18]. In such applications, forward focussing features caused by scattering from atoms in the overlayer are in directions parallel to the surface and are not readily observed. Strong modulations in the photoemitted signal can still be observed at low take-off angles ( $< 20^\circ$ ) however, due to near forward scattering events within the overlayer and scattering from the substrate, although this second contribution is weaker due to the larger scattering angles involved. Sensitivity to the substrate generally

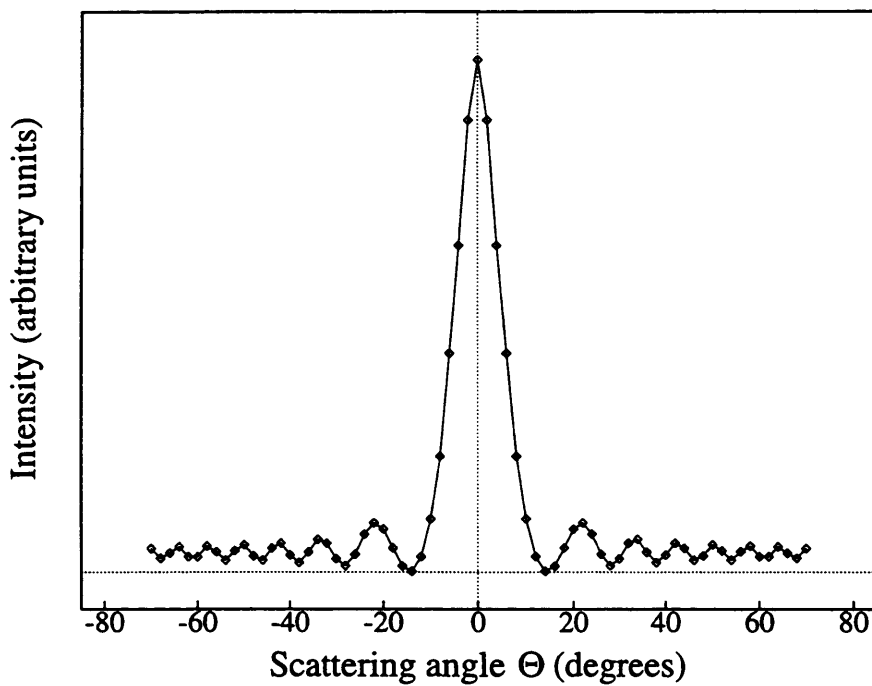
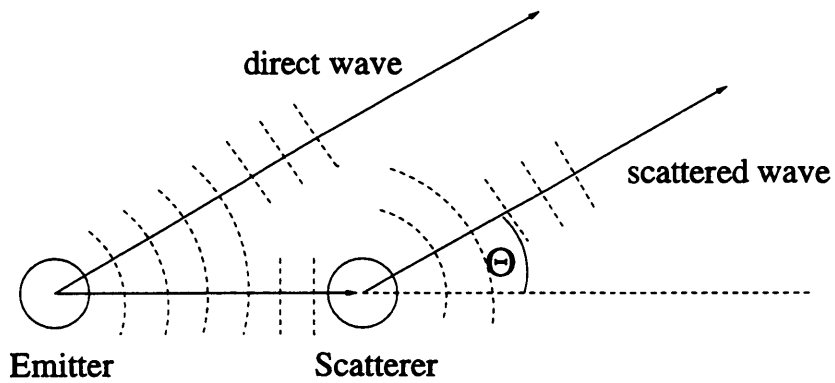


Figure 2.2: A model calculation to demonstrate the "forward focussing" of high energy photoelectrons. A 1000eV photoelectron is emitted from one Cu atom, part of which scatters from the other (upper diagram). Observed intensity is plotted as a function of scattering angle  $\Theta$  (lower diagram), showing interference fringes and a forward focussing peak along the interatomic axis.

depends on the adsorption height of the overlayer and the take-off angle at which the measurements are taken [18]. Deriving structural information from such data requires quantitative comparison of the data with scattering calculations, a topic which is now discussed further.

## 2.3 Current XPD Computational Schemes

### 2.3.1 Single Scattering Calculations

Forward focussing features provide useful, but largely qualitative information about surface structure. In general it is necessary to perform scattering calculations and compare them with experiment to determine structural parameters. The most common theoretical model used to interpret XPD data over recent years has been the single scattering cluster (SSC) model.

In the SSC framework, the scattering is restricted to a cluster of atoms centred on the emitter, and so does not require that the structure possess translational symmetry parallel to the surface. The intensity is calculated from the interference between the direct wave and one scattered wave from each atom in the cluster. Even this simplified model requires sophisticated computer programs to treat accurately: a full treatment should include spherical wave scattering, and two interfering final state channels corresponding to  $l_i + 1$  and  $l_i - 1$  (allowed dipole transitions), where  $l_i$  is the initial state angular momentum quantum number [25]. Such programs can be demanding on CPU time, and so some treatments have used plane wave scattering, assumed an initial  $s$ -state so that the final state involves only a  $p$ -wave, or used both of these approximations.

The outline presented here is the approach given by Fadley [31], to which the reader is referred to for a more comprehensive discussion. The model uses

plane wave scattering and a  $s$ -wave initial state, and as such represents the most simplified approach to SSC calculations. The review by Fadley also discusses the accuracy of the approximations used. The intensity in a given direction  $I(\mathbf{k})$  is derived from a dipole transition between an initial core state  $\psi_c(\mathbf{r})$  and a final state  $\psi(\mathbf{r}, \mathbf{k})$ ,

$$I(\mathbf{k}) \propto |\langle \psi(\mathbf{r}, \mathbf{k}) | \boldsymbol{\epsilon} \cdot \mathbf{r} | \psi_c(\mathbf{r}) \rangle|^2,$$

where  $\boldsymbol{\epsilon}$  is the polarisation of the incident radiation. The single scattering approximation comes with the description of the final state wave function, which is written as

$$\psi(\mathbf{r}, \mathbf{k}) = \phi_0(\mathbf{r}, \mathbf{k}) + \sum_j \phi_j(\mathbf{r}, \mathbf{r}_j \rightarrow \mathbf{k}).$$

This final state can be seen to be composed of a wave  $\phi_0(\mathbf{r}, \mathbf{k})$  which propagates directly to the detector along  $\mathbf{k}$ , and all waves  $\phi_j(\mathbf{r}, \mathbf{r}_j \rightarrow \mathbf{k})$  which result from the initial  $\phi_0$  wave propagating towards a scatterer  $j$  at  $\mathbf{r}_j$ , being subsequently scattered into the direction  $\mathbf{k}$ . The detector essentially lies at infinity along  $\mathbf{k}$  and so the waves  $\phi$  are taken to be of the limiting spherical form of  $\phi_0 \propto \exp(ikr)/r$  and  $\phi_j \propto f_j(\theta_j) \exp(ik|\mathbf{r} - \mathbf{r}_j|)/|\mathbf{r} - \mathbf{r}_j|$ .

The quantity  $f_j(\theta)$  is the electron-atom scattering factor for atom  $j$ , and this approach takes it to be a plane wave scattering factor. This assumes that although  $\phi_0$  is spherical, the portion incident upon scatterer  $j$  has sufficiently low curvature to be treated as a plane wave (known as the "small atom approximation"[35]). The scattering factor may be written as the complex number

$$f_j(\theta_j) = |f_j(\theta_j)| \exp[i\psi_j(\theta_j)],$$

meaning the overall phase shift of a scattered wave  $\phi_j$  relative to  $\phi_0$  is  $kr_j(1 - \cos\theta_j) + \psi_j(\theta_j)$ , due to the path length difference and the scattering

phase shift. The final expression using an  $s$ -initial state for the observed intensity in direction  $\mathbf{k}$  for an X-ray beam with polarisation  $\boldsymbol{\epsilon}$  is given by

$$I(\mathbf{k}) \propto \left| \boldsymbol{\epsilon} \cdot \mathbf{k} e^{-\gamma L} + \sum_j \frac{\boldsymbol{\epsilon} \cdot \mathbf{r}_j}{r_j} |f_j(\theta_j)| W_j e^{-\gamma L_j} \{ \exp i[kr_j(1 - \cos \theta_j) + \psi_j(\theta_j)] \} \right|^2 \\ + \sum_j (\boldsymbol{\epsilon} \cdot \mathbf{r}_j)^2 \frac{|f_j(\theta_j)|^2}{r_j^2} (1 - W_j^2) e^{-2\gamma L_j}.$$

The  $W_j$  are Debye-Waller factors to account for thermal motion of the atoms in the structure, and the  $\exp(-\gamma L)$ ,  $\exp(-\gamma L_j)$  are attenuation factors which simulate the decay of the outgoing waves due to inelastic scattering. This decaying nature means that scatterers further away from the emitter contribute less to the calculated signal. Calculations therefore converge as the cluster size is increased, the size of the converged cluster being determined by trial calculations.

The single scattering formalism of photoelectron diffraction, even with the refinements described earlier, does not include all orders of scattering and as such breaks down for certain systems when strong multiple scattering effects are present [14, 15]. It is difficult to say exactly when single scattering approaches fail. At shallow angles of emission, dynamical effects are expected to be more significant, since the photoelectron travels almost parallel to the surface, thus encountering more scatterers. This effect has been shown to be strongest along azimuths corresponding to closed packed atomic rows [15], where the photoelectron may undergo multiple small-angle scatterings before emerging from the crystal. The type of atoms present in the structure is also important, heavy strong-scattering atoms increasing the likelihood of multiple scattering.

### 2.3.2 Multiple Scattering Calculations

Much of the early work on multiple scattering schemes for angle resolved photoemission was aimed at low energy electrons. Leibsch [3], Pendry [38] and Li *et al.* [39] proposed methods for calculating photoemission spectra, all of which were based on techniques from LEED theory. More recently methods have been developed to perform multiple scattering calculations for the higher energy XPD. Most of these methods exploit the short inelastic scattering length for electrons of this energy, thereby restricting the multiple scattering calculation to a cluster of atoms localised around the emitter. Again, translational symmetry parallel to the surface is not required for cluster calculations of this type.

Saldin *et al.* have developed a method called the concentric shell algorithm [26] which can be applied to XPD. In this technique, the volume surrounding the emitting atom is divided into concentric shells, each containing a number of scattering atoms. The photoelectron wave field between each pair of neighbouring shells, say  $q$  and  $q + 1$ , is assumed to take the same form, a linear combination of spherical waves

$$\sum_{l,m} A_{lm}^{(q)} h_l^{(1)}(kr) Y_{lm}(\theta, \phi),$$

where  $A_{lm}^{(q)}$  are the expansion coefficients and  $h_l^{(1)}$  is a spherical Hankel function of the first kind. A matrix  $\mathbf{S}^{(q)}$  is calculated which relates the coefficients  $A_{lm}^{(q)}$  to the coefficients  $A_{lm}^{(0)}$  via the relation

$$\mathbf{A}^{(q)} = \mathbf{S}^{(q)} \mathbf{A}^{(0)}$$

$\mathbf{A}^{(q)}$  and  $\mathbf{A}^{(0)}$  being vectors whose elements are the corresponding expansion coefficients. The elements of  $\mathbf{A}^{(0)}$  are determined from a dipole transition between the core state  $(l, m)$  and the quantum numbers  $(l', m')$  of the partial wave.

The matrix  $\mathbf{S}^{(q)}$  describes the full multiple scattering of the photoelectron wave between the origin and shell  $q$ . For an  $N$ -shell system, the aim is to compute the scattering matrix  $\mathbf{S}^{(N)}$  which allows the final outgoing wave field to be determined. A method is given for carrying out a multiple scattering calculation within a shell and between two shells by a Green function method, allowing  $\mathbf{S}^{(q+1)}$  to be determined recursively from  $\mathbf{S}^{(q)}$ . Full details of this process are given in ref. [26].

The computer time required for cluster calculations of this type scales roughly as  $l^4$  where  $l$  is the number of angular momentum states in the spherical wave expansion [26]. The size of  $l$  depends upon the energy of the photoelectron, becoming larger as the energy increases. Other sophisticated methods based on the expansion of an outgoing spherical electron wave about a new centre (the scatterer) have been developed by Friedman and Fadley [25], and by Fritzsche [24]. These methods are also based in the theoretical framework of the partial wave expansion, and in the same way become very computer intensive at XPD energies.

Approximation techniques are sometimes introduced to reduce the scale of the calculations in spherical wave cluster methods. An approach taken by Saldin *et al.* in the concentric shell method is to employ what they term the "forward scattering approximation", based on the forward nature of the scattering in the XPD energy range. All intra-shell multiple scatterings are neglected, as these paths involve quite large scattering angles, and the final amplitudes  $\mathbf{A}^{(N)}$  are found by taking successive transmissions of the initial amplitudes through the shells. This essentially neglects all backscattering ( $\theta > 90^\circ$ ) events either within a shell or between shells. Fritzsche has also described approximate techniques to reduce the scale of full multiple scattering calculations [24].

In summary then, any multiple scattering calculation based on a spherical wave expansion will require a large number of angular momentum states to converge at high energies. The possibility of an alternative calculation which is not based on a spherical wave expansion is therefore an attractive option, and is now addressed.

## 2.4 A New Multiple Scattering Scheme for XPD

A method for calculating XPD patterns from periodic surfaces which includes full multiple scattering will be introduced in this section. The technique is based on the dynamical theory of RHEED, which is given in chapter 3. Plane waves are used as a basis set for the wave function expansion rather than the partial wave expansions described above. The plane wave expansion converges quickly at RHEED energies (10keV and above), requiring only a few terms for simple surfaces. More terms will be needed at XPD energies, a problem which will be addressed in chapter 4, but the method should provide a more efficient way of performing the higher energy XPD calculations without introducing approximations.

### 2.4.1 The XPD Pattern

The starting point for this theory is the electric dipole approximation for atomic transitions. A full treatment of this can be found in standard quantum mechanics texts such as Schiff [44], and is not given here. Within the dipole approximation, the photoelectron intensity predicted in direction  $\mathbf{k}$  far from an emitter is

$$I(\mathbf{k}) \propto |\langle \psi_f(\mathbf{r}, \mathbf{k}) | \boldsymbol{\epsilon} \cdot \mathbf{r} | \psi_{nlm}(\mathbf{r}) \rangle|^2. \quad (2.1)$$

In this expression, the emitter is taken to be at the origin,  $\psi_{nlm}$  is the initial core level wave function,  $\psi_f$  is the unbound photoelectron wave function and  $\boldsymbol{\epsilon}$  is the

polarisation vector of the incident light. It is the modulations of the signal as a function of emission angle that is of interest rather than an absolute value, so only the calculation of this expression is required. For this reason the "proportional to" symbol will be replaced by an "equal to" symbol in the following derivations. There are some factors which need to be considered before any matrix elements are calculated: emitters with different local surroundings, the magnetic sub-levels in a particular orbital and the polarisation of the incident X-ray beam. Each of these will now be treated in turn.

(i) *Inequivalent Emitters.* The observed XPD signal comes from a large number of emitting atoms. The process is incoherent, that is, there is no interference between waves originating from different atoms. The total intensity can therefore be written as the sum of the intensities from each emitting atom. For a system with  $j$  emitting atoms at positions  $\mathbf{r}_j$ , the intensity is

$$I(\mathbf{k}) = \sum_j |\langle \psi_f(\mathbf{r}) | \boldsymbol{\epsilon} \cdot (\mathbf{r} - \mathbf{r}_j) | \psi_{nlm}(\mathbf{r} - \mathbf{r}_j) \rangle|^2,$$

which by a change of integration variable in each matrix element may be written

$$I(\mathbf{k}) = \sum_j |\langle \psi_f(\mathbf{r} + \mathbf{r}_j) | \boldsymbol{\epsilon} \cdot \mathbf{r} | \psi_{nlm}(\mathbf{r}) \rangle|^2. \quad (2.2)$$

It is known that the surface possesses translational symmetry, so this intensity can be thought of as originating from a large number of unit cells. Since each cell is identical, only one need be considered to predict the XPD pattern. The summation over  $j$  in Eq. (2.2) is therefore restricted to run over emitters in a single unit cell only.

(ii) *Magnetic Sub-levels.* By simple energy considerations, the final state energy corresponding to a particular initial orbital can be calculated, and the photoelectron detection apparatus tuned to this energy. This initial orbital has

a degeneracy of  $2 \times (2l + 1)$  in the absence of a magnetic field, and so the  $(2l + 1)$  different spatial wave functions must be taken into account. Each of these states is equally likely to be excited for a filled core level, and as the contributions from different emitters are incoherent, the intensity must be summed over magnetic quantum number  $m$ . Taking this into account gives

$$\begin{aligned} I(\mathbf{k}) &= \sum_{m=-l}^l \sum_j |\langle \psi_f(\mathbf{r} + \mathbf{r}_j) | \boldsymbol{\epsilon} \cdot \mathbf{r} | \psi_{nlm}(\mathbf{r}) \rangle|^2 \\ &= \sum_{m=-l}^l \sum_j |\boldsymbol{\epsilon} \cdot \mathbf{R}_{mj}|^2, \end{aligned} \quad (2.3)$$

where the polarisation vector has been removed from each matrix element and the substitutions

$$\mathbf{R}_{mj} = \langle \psi_f(\mathbf{r} + \mathbf{r}_j) | \mathbf{r} | \psi_{nlm}(\mathbf{r}) \rangle \quad (2.4)$$

have been made.

(iii) *X-Ray Polarisation.* The expressions (2.3) and (2.4) can be used to calculate XPD intensities for incident radiation with polarisation vector  $\boldsymbol{\epsilon}$ . In general however, the X-ray source will produce an unpolarised radiation beam, and so Eq. (2.3) must be integrated over all orientations of the polarisation vector,

$$I(\mathbf{k}) = \sum_{m=-l}^l \sum_j \int |\boldsymbol{\epsilon} \cdot \mathbf{R}_{mj}|^2 d\boldsymbol{\epsilon}. \quad (2.5)$$

Let the plane of polarisation be the  $y'$ - $z'$  plane of a cartesian frame  $(x', y', z')$ . The orientation of polarisation vector  $\boldsymbol{\epsilon}$  can be described by a single angle  $\beta$ , defined to be measured anticlockwise from the  $y'$  axis. This is illustrated in Fig. 2.3. The unit polarisation vector can therefore be expressed

$$\boldsymbol{\epsilon} = \begin{pmatrix} 0 \\ \cos \beta \\ \sin \beta \end{pmatrix}. \quad (2.6)$$

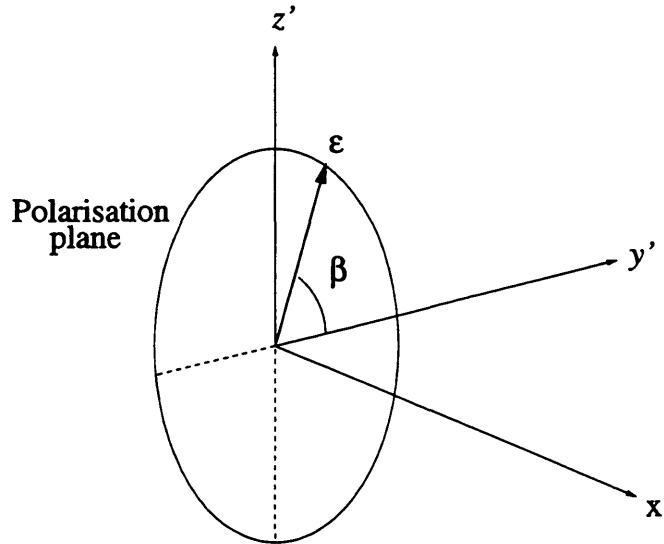


Figure 2.3: The polarisation vector, positioned in the  $y'$ - $z'$  plane of system  $(x', y', z')$  by the angle  $\beta$ .

It is now necessary to express  $\epsilon$  in the frame  $(x, y, z)$ , which is shown in Fig. 2.1. This requires two co-ordinate transformations: a clockwise rotation of  $\phi$  about the  $z'$  axis, followed by an anticlockwise rotation of  $\alpha$  about the new  $y'$  axis. This assumes that X-ray incidence and electron exit are in the same plane as in Fig. 2.1. When this is not the case, the only difference is that the first rotation about the  $z'$  axis will be through a different angle depending on the incident X-ray direction. Using the appropriate rotation matrices,  $\epsilon$  in the  $(x, y, z)$  frame is

$$\epsilon = \begin{pmatrix} -\cos \alpha \sin \phi \cos \beta + \sin \alpha \sin \beta \\ \cos \phi \cos \beta \\ \sin \alpha \sin \phi \cos \beta + \cos \alpha \sin \beta \end{pmatrix}. \quad (2.7)$$

The angles  $\alpha$  and  $\phi$  have been defined at the beginning of the chapter, and are indicated in Fig. 2.1. By using this expression for  $\epsilon$ , the required integration in

Eq. (2.5) is found to be

$$\int |\boldsymbol{\epsilon} \cdot \mathbf{R}_{mj}|^2 d\boldsymbol{\epsilon} = \int_0^{2\pi} |\sin \beta (R_{xmj} \sin \alpha + R_{zmj} \cos \alpha) + \cos \beta (R_{ymj} \cos \phi + R_{zmj} \sin \alpha \sin \phi - R_{xmj} \cos \alpha \sin \phi)|^2 d\beta.$$

Expanding the absolute square and performing the integration gives the result

$$\int |\boldsymbol{\epsilon} \cdot \mathbf{R}_{mj}|^2 d\boldsymbol{\epsilon} = \pi (|A_{mj}|^2 + |B_{mj}|^2), \quad (2.8)$$

where  $A_{mj}$  and  $B_{mj}$  are given by

$$A_{mj} = R_{xmj} \sin \alpha + R_{zmj} \cos \alpha \quad (2.9)$$

$$B_{mj} = R_{ymj} \cos \phi + R_{zmj} \sin \alpha \sin \phi - R_{xmj} \cos \alpha \sin \phi. \quad (2.10)$$

For an unpolarised X-ray beam, the photoelectron intensity can be calculated by using Eqs. (2.8), (2.9) and (2.10) in (2.5).

### 2.4.2 Wave Functions

The state  $\psi_f$  in the matrix elements defined in Eq. (2.4) is the photoelectron final state. This can be described as a time-reversed scattering state: the angle resolved measurement of the photoemission signal defines  $\mathbf{k}_{\parallel}$ , the component of final wave vector parallel to the surface, which is analagous to the  $\mathbf{k}_{\parallel}$  defined by an incident beam of electrons. This approach is often called the "one-step" model of photoemission. The scattering wave function consists of an incident plane wave, orientated to give the correct  $\mathbf{k}_{\parallel}$ , which is allowed to scatter from the crystal surface, giving rise to a set of scattered waves in the vacuum matched onto a set of Bloch waves in the crystal. The time-reversed counterpart is a set of incoming "scattered" waves and a single outgoing plane wave travelling towards the detector in the vacuum, and is found by forming the complex conjugate of the scattering

state. Previous theoretical work at low energies in photoelectron diffraction and spectroscopy have made use of a time-reversed LEED wave function in similar calculations [40, 41, 42, 43]. As previously explained, because of the higher energies involved in the present work, RHEED theory is used to calculate the final state. A full treatment of the dynamical theory of RHEED is given in chapter 3, and for the moment only the form of the wave function is required. For a surface periodic in the parallel dimensions ( $x$  and  $y$ ) with reciprocal mesh vectors  $\boldsymbol{\kappa}$ , the RHEED wave function can be written

$$\psi(\mathbf{r}) = \exp(i\mathbf{k}_{\parallel} \cdot \boldsymbol{\rho}) \sum_{\boldsymbol{\kappa}} \phi_{\boldsymbol{\kappa}}(z) \exp(i\boldsymbol{\kappa} \cdot \boldsymbol{\rho}), \quad (2.11)$$

where  $\mathbf{k}_{\parallel}$  is the the component of incident wave vector parallel to the surface and  $\boldsymbol{\rho}$  is a 2-D position vector ( $x, y$ ). The final state, found by complex conjugation, is therefore

$$\psi_f(\mathbf{r}) = \exp(-i\mathbf{k}_{\parallel} \cdot \boldsymbol{\rho}) \sum_{\boldsymbol{\kappa}} \phi_{\boldsymbol{\kappa}}^*(z) \exp(-i\boldsymbol{\kappa} \cdot \boldsymbol{\rho}). \quad (2.12)$$

This wave function accounts for all possible scattering between emission and detection, since the coefficients  $\phi_{\boldsymbol{\kappa}}(z)$  are computed by a numerical integration of the Schrödinger equation of the system.

The core-level wave functions,  $\psi_{nlm}$  in Eq. (2.4), can be expected to be described reasonably well by those of a free atom. Clementi and Roetti [45] have expressed Roothaan-Hartree-Fock atomic wave functions in the analytic form

$$\psi_{nlm}(\mathbf{r}) = \sum_s c_s \chi_s(\mathbf{r}), \quad (2.13)$$

where the basis states  $\chi_s$  are Slater orbitals, which take the form

$$\chi_s(\mathbf{r}) = N_s r^{n_s-1} \exp(-\alpha_s r) Y_{lm}(\theta, \phi). \quad (2.14)$$

The factor  $N_s$  in (2.14) is a normalisation constant given by the expression

$$N_s = \frac{(2\alpha_s)^{n_s + \frac{1}{2}}}{[(2n)!]^{\frac{1}{2}}}, \quad (2.15)$$

and the  $Y_{lm}(\theta, \phi)$  are normalised spherical harmonics in complex form. The expansion coefficients  $c_s$  are such that the full expression for  $\psi_{nlm}(\mathbf{r})$  is normalised to unity. The coefficients  $c_s$ , orbital exponents  $\alpha_s$  and principal quantum numbers of the individual basis states  $n_s$  are all tabulated.

### 2.4.3 Calculation of Matrix Elements

The total intensity from the periodic system of emitters has been shown to depend on the matrix elements  $\mathbf{R}_{mj}$ , defined in Eq. (2.4). In this section it will be shown how these matrix elements can be calculated. Writing the  $\mathbf{R}_{mj}$  in integral form gives

$$\mathbf{R}_{mj} = \int \psi_f^*(\mathbf{r} + \mathbf{r}_j) \mathbf{r} \psi_{nlm}(\mathbf{r}) d\mathbf{r}. \quad (2.16)$$

The initial and final state wave functions, Eqs. (2.13), (2.14) and (2.12), can be substituted into Eq. (2.16) to give the rather complicated expression

$$\begin{aligned} \mathbf{R}_{mj} &= \exp(i\mathbf{k}_{\parallel} \cdot \boldsymbol{\rho}_j) \sum_{\boldsymbol{\kappa}, s} c_s N_s \exp(i\boldsymbol{\kappa} \cdot \boldsymbol{\rho}_j) \\ &\times \int \phi_{\boldsymbol{\kappa}}(z + z_j) \exp[i(\mathbf{k}_{\parallel} + \boldsymbol{\kappa}) \cdot \boldsymbol{\rho}] \mathbf{r} r^{n_s - 1} \exp(-\alpha_s r) Y_{lm}(\theta, \phi) d\mathbf{r}. \end{aligned} \quad (2.17)$$

It is convenient to simplify this expression by defining the vector quantities  $\mathbf{P}_{m\boldsymbol{\kappa}j}$  as

$$\mathbf{P}_{m\boldsymbol{\kappa}j} = \sum_s c_s N_s \int \phi_{\boldsymbol{\kappa}}(z + z_j) \exp[i(\mathbf{k}_{\parallel} + \boldsymbol{\kappa}) \cdot \boldsymbol{\rho}] \mathbf{r} r^{n_s - 1} \exp(-\alpha_s r) Y_{lm}(\theta, \phi) d\mathbf{r}, \quad (2.18)$$

allowing the matrix elements  $\mathbf{R}_{mj}$  to be written as

$$\mathbf{R}_{mj} = \exp(i\mathbf{k}_{\parallel} \cdot \boldsymbol{\rho}_j) \sum_{\boldsymbol{\kappa}} \exp(i\boldsymbol{\kappa} \cdot \boldsymbol{\rho}_j) \mathbf{P}_{m\boldsymbol{\kappa}j}. \quad (2.19)$$

The aim now is to calculate the  $\mathbf{P}_{m\kappa j}$ . For computational reasons, it is necessary to work in the cartesian co-ordinate system in which the final state wave function is represented, shown in Fig. 2.1. The quantity  $r^l Y_{lm}(\theta, \phi)$  can be straightforwardly expressed in the cartesian frame using the usual co-ordinate transformations between the spherical and rectangular systems. Let the cartesian form of  $r^l Y_{lm}(\theta, \phi)$  be denoted by  $\mathcal{Y}_{lm}(x, y, z)$ . Eq. (2.18) can now be written as

$$\mathbf{P}_{m\kappa j} = \sum_s C_s \int \phi_{\kappa}(z + z_j) \exp(i\mathbf{q}\kappa \cdot \boldsymbol{\rho}) \mathbf{r} r^{n'_s} \exp(-\alpha_s r) \mathcal{Y}_{lm}(x, y, z) d\mathbf{r}, \quad (2.20)$$

where, for notational convenience, the substitutions

$$\mathbf{q}\kappa = \mathbf{k}_{\parallel} + \kappa, \quad (2.21)$$

$$n'_s = n_s - l - 1 \quad (2.22)$$

have been made and the product  $c_s N_s$  has been denoted  $C_s$ . To proceed, vector  $\mathbf{r}$  is written in component form, giving

$$\mathbf{P}_{m\kappa j} = \begin{pmatrix} \sum_s C_s \int \phi_{\kappa j} \exp(i\mathbf{q}\kappa \cdot \boldsymbol{\rho}) x r^{n'_s} \exp(-\alpha_s r) \mathcal{Y}_{lm} dx dy dz \\ \sum_s C_s \int \phi_{\kappa j} \exp(i\mathbf{q}\kappa \cdot \boldsymbol{\rho}) y r^{n'_s} \exp(-\alpha_s r) \mathcal{Y}_{lm} dx dy dz \\ \sum_s C_s \int \phi_{\kappa j} \exp(i\mathbf{q}\kappa \cdot \boldsymbol{\rho}) z r^{n'_s} \exp(-\alpha_s r) \mathcal{Y}_{lm} dx dy dz \end{pmatrix}. \quad (2.23)$$

The presence of the exponential factors  $\exp(i\mathbf{q}\kappa \cdot \boldsymbol{\rho})$  and  $\exp(-\alpha_s r)$  in the integrands of Eq. (2.23) makes it possible to introduce some simplifications. It is clear that

$$r \exp(-\alpha_s r) = -\frac{\partial}{\partial \alpha_s} \{ \exp(-\alpha_s r) \},$$

and so the factor  $r^{n'_s}$  can be generated by operating with

$$\hat{r} = -\frac{\partial}{\partial \alpha_s} \quad (2.24)$$

$n'_s$  times on  $\exp(-\alpha_s r)$ . In exactly the same way, since

$$\exp(i\mathbf{q}\kappa \cdot \boldsymbol{\rho}) = \exp[iq\kappa_x x + iq\kappa_y y],$$

the differential operators  $\hat{x}$  and  $\hat{y}$ , defined as

$$\hat{x} = \frac{\partial}{\partial(iq_{\kappa_x})}, \quad \hat{y} = \frac{\partial}{\partial(iq_{\kappa_y})}, \quad (2.25)$$

can be introduced into Eq. (2.23) to generate occurrences of  $x$  and  $y$  by operating on  $\exp(i\mathbf{q}_{\kappa} \cdot \boldsymbol{\rho})$ . Replacing  $r$ ,  $x$  and  $y$  in Eq. (2.23) by their appropriate operators gives

$$\mathbf{P}_{m\kappa_j} = \begin{pmatrix} \sum_s C_s \int \phi_{\kappa_j} \hat{x} \mathcal{Y}_{lm} \exp(i\mathbf{q}_{\kappa} \cdot \boldsymbol{\rho}) \hat{r}^{n'_s} \exp(-\alpha_s r) dx dy dz \\ \sum_s C_s \int \phi_{\kappa_j} \hat{y} \mathcal{Y}_{lm} \exp(i\mathbf{q}_{\kappa} \cdot \boldsymbol{\rho}) \hat{r}^{n'_s} \exp(-\alpha_s r) dx dy dz \\ \sum_s C_s \int \phi_{\kappa_j} z \mathcal{Y}_{lm} \exp(i\mathbf{q}_{\kappa} \cdot \boldsymbol{\rho}) \hat{r}^{n'_s} \exp(-\alpha_s r) dx dy dz \end{pmatrix}, \quad (2.26)$$

with  $\mathcal{Y}_{lm}$  now being  $\mathcal{Y}_{lm}(\hat{x}, \hat{y}, z)$ . The advantage of introducing operators  $\hat{r}$ ,  $\hat{x}$  and  $\hat{y}$  is that they may be removed from the integral over  $x$  and  $y$  co-ordinates, leaving a simpler integral to evaluate. Operating on the result then generates the full  $x$ - $y$  integral. Adopting this procedure, Eq. (2.26) becomes

$$\mathbf{P}_{m\kappa_j} = \begin{pmatrix} \sum_s C_s \int \phi_{\kappa_j} [\hat{x} \mathcal{Y}_{lm} \hat{r}^{n'_s} \int \exp(i\mathbf{q}_{\kappa} \cdot \boldsymbol{\rho}) \exp(-\alpha_s r) dx dy] dz \\ \sum_s C_s \int \phi_{\kappa_j} [\hat{y} \mathcal{Y}_{lm} \hat{r}^{n'_s} \int \exp(i\mathbf{q}_{\kappa} \cdot \boldsymbol{\rho}) \exp(-\alpha_s r) dx dy] dz \\ \sum_s C_s \int \phi_{\kappa_j} z [\mathcal{Y}_{lm} \hat{r}^{n'_s} \int \exp(i\mathbf{q}_{\kappa} \cdot \boldsymbol{\rho}) \exp(-\alpha_s r) dx dy] dz \end{pmatrix}. \quad (2.27)$$

The two dimensional integral

$$\mathcal{I} = \int \exp(i\mathbf{q}_{\kappa} \cdot \boldsymbol{\rho}) \exp(-\alpha_s r) dx dy \quad (2.28)$$

which appears in all three components parenthesised in Eq. (2.27) may be performed analytically. The details of the integration are given in Appendix A, the result being

$$\mathcal{I} = 2\pi\alpha_s \frac{\exp(-|z|b_{\kappa_s})}{b_{\kappa_s}^3} (1 + |z|b_{\kappa_s}), \quad (2.29)$$

where the parameter  $b_{\kappa_s}$  is defined by

$$b_{\kappa_s}^2 = \alpha_s^2 + q_{\kappa}^2. \quad (2.30)$$

It is convenient at this point to define a set of functions of the  $z$  co-ordinate and some parameter  $b$ , by the relations

$$f^{(n)} = \frac{\exp(-|z|b)}{b^{2n+1}} \sum_{p=0}^n a_p |z|^p b^p \quad (2.31)$$

$$f^{(n+1)} = -\frac{1}{b} \frac{\partial f^{(n)}}{\partial b}, \quad (2.32)$$

where  $n \geq 1$  and  $a_p$  are a set of real coefficients. The lowest order function,  $n = 1$ , is defined to be

$$f^{(1)} = \frac{\exp(-|z|b)}{b^3} (1 + |z|b). \quad (2.33)$$

The definitions (2.31) and (2.32) allow a relationship between the coefficients in the summations of any two consecutive functions  $f^{(n)}$  and  $f^{(n+1)}$  to be found. Let  $a_p$  and  $a'_p$  be the expansion coefficients in  $f^{(n)}$  and  $f^{(n+1)}$  respectively. By substituting (2.31) into (2.32) and performing the differentiation, an explicit expression for  $f^{(n+1)}$  in terms of  $a_p$  can be found. As Eq. (2.31) dictates that  $f^{(n+1)}$  takes the form

$$f^{(n+1)} = \frac{\exp(-|z|b)}{b^{2n+3}} \sum_{p=0}^{n+1} a'_p |z|^p b^p, \quad (2.34)$$

this expression may be compared to the explicit expression, which leads to the relations

$$\begin{aligned} a'_0 &= (2n+1)a_0 \\ a'_p &= a_{p-1} + (2n+1-p)a_p \quad (1 \leq p \leq n) \\ a'_{n+1} &= a_n = 1. \end{aligned} \quad (2.35)$$

The coefficient  $a'_{n+1}$  is always equal to unity because of the definition of the lowest order function  $f^{(1)}$  in (2.33). As the coefficients of  $f^{(1)}$  are defined by (2.33), the coefficients of any function  $f^{(n)}$  can be calculated by repeated use of relations (2.35).

Using the definition (2.33), the result of integral (2.28) can be written as

$$\mathcal{I} = 2\pi\alpha_s f_{\kappa_s}^{(1)}, \quad (2.36)$$

$f_{\kappa_s}^{(1)}$  having the subscripts  $\kappa_s$  because of its dependence on the parameter  $b_{\kappa_s}$ , defined by Eq. (2.30). Substituting this result into Eq. (2.27) gives

$$\mathbf{P}_{m\kappa_j} = \begin{pmatrix} 2\pi \sum_s C_s \int \phi_{\kappa}(z + z_j) [\hat{x} \mathcal{Y}_{lm}(\hat{x}, \hat{y}, z) \hat{r}^{n_s} \alpha_s f_{\kappa_s}^{(1)}(z)] dz \\ 2\pi \sum_s C_s \int \phi_{\kappa}(z + z_j) [\hat{y} \mathcal{Y}_{lm}(\hat{x}, \hat{y}, z) \hat{r}^{n_s} \alpha_s f_{\kappa_s}^{(1)}(z)] dz \\ 2\pi \sum_s C_s \int \phi_{\kappa}(z + z_j) z [\mathcal{Y}_{lm}(\hat{x}, \hat{y}, z) \hat{r}^{n_s} \alpha_s f_{\kappa_s}^{(1)}(z)] dz \end{pmatrix}, \quad (2.37)$$

where explicit dependence on the  $z$  co-ordinate has been indicated. By changing the order of the integrations and summations and employing a change of integration variable, Eq. (2.37) can be re-written in the form

$$\mathbf{P}_{m\kappa_j} = \begin{pmatrix} \int \phi_{\kappa}(z) g_{m\kappa}^x(z - z_j) dz \\ \int \phi_{\kappa}(z) g_{m\kappa}^y(z - z_j) dz \\ \int \phi_{\kappa}(z) g_{m\kappa}^z(z - z_j) dz \end{pmatrix}, \quad (2.38)$$

using the definitions

$$\begin{aligned} g_{m\kappa}^x(z) &= 2\pi \sum_s C_s \hat{x} \mathcal{Y}_{lm}(\hat{x}, \hat{y}, z) \hat{r}^{n_s} \alpha_s f_{\kappa_s}^{(1)}(z) \\ g_{m\kappa}^y(z) &= 2\pi \sum_s C_s \hat{y} \mathcal{Y}_{lm}(\hat{x}, \hat{y}, z) \hat{r}^{n_s} \alpha_s f_{\kappa_s}^{(1)}(z) \\ g_{m\kappa}^z(z) &= 2\pi \sum_s C_s z \mathcal{Y}_{lm}(\hat{x}, \hat{y}, z) \hat{r}^{n_s} \alpha_s f_{\kappa_s}^{(1)}(z). \end{aligned} \quad (2.39)$$

The integrals in Eq. (2.38) are now in the correct form for numerical evaluation, once the functions in Eq. (2.39) have been evaluated by applying the differential operators. To do this it is necessary to know the result of operating on a function  $f_{\kappa_s}^{(n)}$  with  $\hat{x}$ ,  $\hat{y}$  and  $\hat{r}$ , defined in Eqs. (2.24) and (2.25). The dependence of a function  $f_{\kappa_s}^{(n)}$  on the quantities  $\alpha_s$  and the components  $q_{\kappa_x}$  and  $q_{\kappa_y}$ , is held

$l, m$	$Y_{lm}(\theta, \phi)$	$\mathcal{Y}_{lm}(\hat{x}, \hat{y}, z)$
0, 0	$\sqrt{\frac{1}{4\pi}}$	$\sqrt{\frac{1}{4\pi}}$
1, 0	$\sqrt{\frac{3}{4\pi}} \cos \theta$	$\sqrt{\frac{3}{4\pi}} z$
1, $\pm 1$	$\mp \sqrt{\frac{3}{8\pi}} \sin \theta e^{\pm i\phi}$	$\mp \sqrt{\frac{3}{8\pi}} (\hat{x} \pm i\hat{y})$
2, 0	$\sqrt{\frac{5}{16\pi}} (3 \cos^2 \theta - 1)$	$\sqrt{\frac{5}{16\pi}} (2z^2 - \hat{x}^2 - \hat{y}^2)$
2, $\pm 1$	$\mp \sqrt{\frac{15}{8\pi}} \cos \theta \sin \theta e^{\pm i\phi}$	$\mp \sqrt{\frac{15}{8\pi}} (\hat{x} \pm i\hat{y}) z$
2, $\pm 2$	$\frac{1}{2} \sqrt{\frac{15}{8\pi}} \sin^2 \theta e^{\pm 2i\phi}$	$\sqrt{\frac{15}{32\pi}} (\hat{x} \pm i\hat{y})^2$
3, 0	$\sqrt{\frac{7}{16\pi}} (5 \cos^3 \theta - 3 \cos \theta)$	$\sqrt{\frac{7}{16\pi}} (2z^2 - 3\hat{x}^2 - 3\hat{y}^2) z$
3, $\pm 1$	$\mp \sqrt{\frac{21}{64\pi}} \sin \theta (5 \cos^2 \theta - 1) e^{\pm i\phi}$	$\mp \sqrt{\frac{21}{64\pi}} (4z^2 - \hat{x}^2 - \hat{y}^2) (\hat{x} \pm i\hat{y})$
3, $\pm 2$	$\sqrt{\frac{105}{32\pi}} \sin^2 \theta \cos \theta e^{\pm 2i\phi}$	$\sqrt{\frac{105}{32\pi}} (\hat{x} \pm i\hat{y})^2 z$
3, $\pm 3$	$\mp \sqrt{\frac{35}{64\pi}} \sin^3 \theta e^{\pm 3i\phi}$	$\mp \sqrt{\frac{35}{64\pi}} (\hat{x} \pm i\hat{y})^3$

Table 2.1: The first few spherical harmonics  $Y_{lm}(\theta, \phi)$  and the corresponding  $\mathcal{Y}_{lm}(\hat{x}, \hat{y}, z)$ . The  $\mathcal{Y}_{lm}(\hat{x}, \hat{y}, z)$  are the quantities  $r^l Y_{lm}(\theta, \phi)$  in a Cartesian representation, with  $x$  and  $y$  replaced by the differential operators  $\hat{x}$  and  $\hat{y}$ .

completely within the parameter  $b_{\kappa_s}$ , defined in Eq. (2.30). Hence the required differentiations can be performed via the chain rule,

$$\begin{aligned} \hat{r} f_{\kappa_s}^{(n)} &= -\frac{\partial b_{\kappa_s}}{\partial \alpha_s} \frac{\partial f_{\kappa_s}^{(n)}}{\partial b_{\kappa_s}} \\ \hat{x} f_{\kappa_s}^{(n)} &= \frac{\partial b_{\kappa_s}}{\partial (iq\kappa_x)} \frac{\partial f_{\kappa_s}^{(n)}}{\partial b_{\kappa_s}} \\ \hat{y} f_{\kappa_s}^{(n)} &= \frac{\partial b_{\kappa_s}}{\partial (iq\kappa_y)} \frac{\partial f_{\kappa_s}^{(n)}}{\partial b_{\kappa_s}}. \end{aligned}$$

From Eq. (2.32), it is known that

$$\frac{\partial f_{\kappa_s}^{(n)}}{\partial b_{\kappa_s}} = -b_{\kappa_s} f_{\kappa_s}^{(n+1)},$$

and by differentiating Eq. (2.30) appropriately, the relations

$$\begin{aligned}\frac{\partial b_{\kappa_s}}{\partial \alpha_s} &= \frac{\alpha_s}{b_{\kappa_s}} \\ \frac{\partial b_{\kappa_s}}{\partial (iq_{\kappa_x})} &= -\frac{iq_{\kappa_x}}{b_{\kappa_s}} \\ \frac{\partial b_{\kappa_s}}{\partial (iq_{\kappa_y})} &= -\frac{iq_{\kappa_y}}{b_{\kappa_s}}\end{aligned}$$

can easily be shown. The required results are therefore

$$\begin{aligned}\hat{r} f_{\kappa_s}^{(n)} &= \alpha_s f_{\kappa_s}^{(n+1)} \\ \hat{x} f_{\kappa_s}^{(n)} &= (iq_{\kappa_x}) f_{\kappa_s}^{(n+1)} \\ \hat{y} f_{\kappa_s}^{(n)} &= (iq_{\kappa_y}) f_{\kappa_s}^{(n+1)}.\end{aligned}\tag{2.40}$$

The first few  $\mathcal{Y}_{lm}(\hat{x}, \hat{y}, z)$  are shown in Table 2.1. Having selected the one corresponding to the quantum numbers  $l$  and  $m$ , it is a straightforward matter to calculate the functions  $g_{m\kappa}^x(z)$ ,  $g_{m\kappa}^y(z)$  and  $g_{m\kappa}^z(z)$  using results (2.40). For example, assume for simplicity that the initial state summation over index  $s$  in Eq. (2.13) contains terms such that  $n'_s (= n_s - l - 1) = 0$ . This removes all occurrences of the operator  $\hat{r}$ . If the calculation is being performed for say, the quantum numbers  $l = 1$  and  $m = 1$ , then the functions (2.39) may be calculated using the  $l = 1, m = 1$  entry in Table 2.1 to be

$$\begin{aligned}g_{1\kappa}^x(z) &= 2\pi\sqrt{\frac{3}{8\pi}} \sum_s C_s \alpha_s [(q_{\kappa_x}^2 + iq_{\kappa_x} q_{\kappa_y}) f_{\kappa_s}^{(3)} - f_{\kappa_s}^{(2)}] \\ g_{1\kappa}^y(z) &= 2\pi\sqrt{\frac{3}{8\pi}} \sum_s C_s \alpha_s [(q_{\kappa_x} q_{\kappa_y} + iq_{\kappa_y}^2) f_{\kappa_s}^{(3)} - i f_{\kappa_s}^{(2)}] \\ g_{1\kappa}^z(z) &= 2\pi\sqrt{\frac{3}{8\pi}} \sum_s C_s \alpha_s (q_{\kappa_y} - iq_{\kappa_x}) z f_{\kappa_s}^{(2)}.\end{aligned}\tag{2.41}$$

Having determined these functions for the  $l$  and  $m$  required, the final step is to perform the integrations over the  $z$  co-ordinate in Eq. (2.38). These integrations must be performed numerically since the coefficient  $\phi_{\kappa}(z)$  appearing in the integrands is extracted from a computer program used to numerically calculate RHEED intensities. The limits of integration in Eq. (2.38) are strictly  $\pm\infty$ , but in practice, the integrals need only be performed over a finite  $z$  range as the  $g_{m\kappa}^x(z - z_j)$ ,  $g_{m\kappa}^y(z - z_j)$  and  $g_{m\kappa}^z(z - z_j)$  decay rapidly away from the  $z_j$ , the  $z$  co-ordinate of the emitter. This is due to the exponential term in the functions  $f^{(n)}$  defined in Eq. (2.31) and physically is a consequence of the localisation of the initial core state. Details of how the numerical integrations are performed are given in chapter 3.

The  $P_{m\kappa j}$  can therefore be calculated from Eq. (2.38), and the matrix elements  $R_{mj}$  by using Eq. (2.19). The XPD intensity can then be calculated from the equations in 2.4.1.

#### 2.4.4 Finite Angular Resolution

It has been shown in the previous sections how the XPD intensity can be calculated. The formulae are for an ideal system however, in which emission occurs into a direction specified by the angles  $(\theta, \phi)$ . In practice, such perfect angular resolution is not attained, as the detection apparatus will always subtend a small solid angle at the surface. The experiment therefore measures the integrated intensity over this solid angle

$$I_{exp}(\theta, \phi) = \int I(\theta, \phi) d\Omega, \quad (2.42)$$

where  $I_{exp}(\theta, \phi)$  is the measured signal, and  $I(\theta, \phi)$  is the intensity distribution for perfect angular resolution. The calculations must account for this integration

before any comparison with experiment can be made.

Typically, the detector aperture defines a cone of half-angle about  $3.0^\circ$ , although some high resolution measurements have been made in which the half-angle is  $1.0 - 1.5^\circ$  [18, 71]. To account for the finite angular resolution, calculated intensities centred around the direction  $(\theta, \phi)$  are averaged. The process is illustrated in Fig. 2.4, where a  $\theta$ - $\phi$  grid of calculated points separated by  $1^\circ$  in each direction is shown, with the point of interest shaded. High resolution experimental data for this point is simulated by averaging points within  $\pm 1^\circ$  in both the  $\theta$  and the  $\phi$  directions, and lower resolution data simulated by using points within  $\pm 2^\circ$ . These points are indicated in Fig. 2.4.

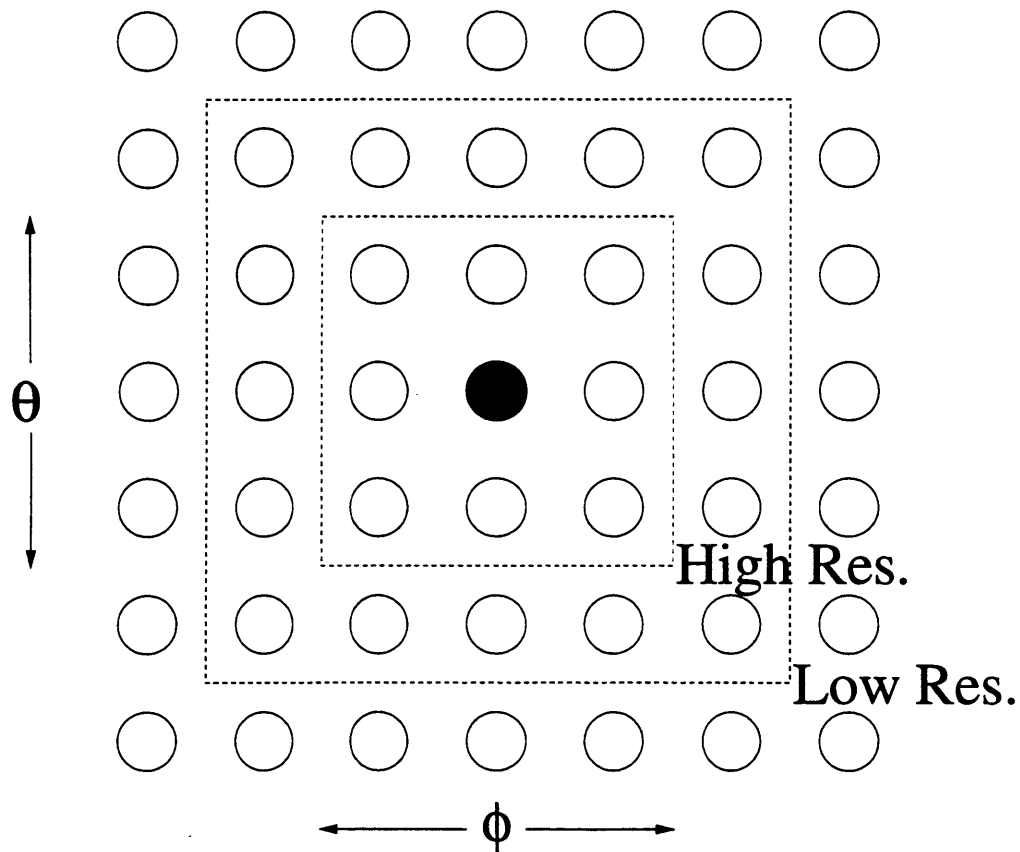


Figure 2.4: Averaging to simulate the finite angular resolution of the experiment. The circles represent calculated points on a  $\theta$ - $\phi$  grid separated by  $1^\circ$  in each direction, with the shaded circle being the point of interest. High resolution experimental data is simulated by averaging points within the  $\pm 1^\circ$  square, while lower resolution data uses points within the  $\pm 2^\circ$  square.

## Chapter 3

# Multiple Scattering Theory and Application to XPD

In chapter 2, the wave function used as the photoelectron final state was of the form of that used in RHEED calculations. This chapter deals with the calculation of the RHEED wave function and the subsequent work required to evaluate the XPD expressions of chapter 2.

The first part of the chapter introduces the theoretical techniques used in elastic RHEED calculations. Typical RHEED experiments utilise electrons in the 10-100keV range, incident upon the surface at a grazing angle of about  $5^\circ$  or below. The low angle of incidence means that despite only penetrating a small distance, the electron encounters many atoms before emerging from the surface. Although the scattering cross section of an isolated atom for such electrons may be small enough to treat by kinematic theory, a full dynamical theory is needed to describe a system of atoms. The first part of the chapter introduces a dynamical theory used to calculate RHEED intensities.

The second part of the chapter is concerned with the modifications to a RHEED computer program required to perform the XPD calculations described in chapter

2. The method devised to do the XPD calculation is described, and some practical problems with its implementation identified and resolved.

### 3.1 Multiple Scattering Theory of RHEED

#### 3.1.1 Introduction

A multiple scattering theory used to calculate RHEED intensities will be introduced here. The basic approach to most of the theoretical work published on RHEED is to divide the system into smaller units by slicing it parallel to the surface [46, 47, 49, 50]. The scattering properties of these units are described by matrices whose elements can be accurately calculated by solving the time independent Schrödinger equation. These matrices are then combined to determine the scattering properties of the system, and hence the RHEED intensities. The theory described here is that of Maksym and Beeby [46, 47], although the precise details of the calculation vary from author to author.

Consider the elastic diffraction of a beam of electrons by a surface which is periodic in the two parallel dimensions ( $x, y$ ), but need not be in the perpendicular dimension ( $z$ ). If the two dimensional vectors describing the periodic surface cell are denoted by  $\mathbf{a} = (a_x, a_y)$  and  $\mathbf{b} = (b_x, b_y)$ , then their reciprocal vectors can be written

$$\mathbf{a}^* = \frac{2\pi}{A_{\parallel}}(b_y, -b_x), \quad \mathbf{b}^* = \frac{2\pi}{A_{\parallel}}(-a_y, a_x). \quad (3.1)$$

The quantity  $A_{\parallel}$  is the area of the real space surface unit cell. The 2D reciprocal mesh is defined by the vectors  $\boldsymbol{\kappa} = l\mathbf{a}^* + m\mathbf{b}^*$ , where  $l$  and  $m$  are integers. The scattering potential  $V(\mathbf{r})$  clearly has the same periodicity as the structure itself

and therefore can be Fourier expanded in terms of the reciprocal mesh vectors as

$$V(\mathbf{r}) = \sum_{\boldsymbol{\kappa}} V_{\boldsymbol{\kappa}}(z) \exp(i\boldsymbol{\kappa} \cdot \boldsymbol{\rho}). \quad (3.2)$$

Vector  $\boldsymbol{\rho}$  is a position vector parallel to the surface  $(x, y)$ , and the expansion coefficients  $V_{\boldsymbol{\kappa}}$  depend on the  $z$  co-ordinate. The electron wave function  $\psi(\mathbf{r})$  does not have the same periodicity as the crystal. By Bloch's theorem in two dimensions, however,  $\psi(\mathbf{r})$  may be written as

$$\psi(\mathbf{r}) = \Phi(\mathbf{r}) \exp(i\mathbf{k}_{\parallel} \cdot \boldsymbol{\rho}),$$

where  $\mathbf{k}_{\parallel}$  is the component of incident electron wave vector parallel to the surface.  $\Phi(\mathbf{r})$  is a function which does have same periodicity as the crystal and so may be Fourier expanded in the same way as  $V(\mathbf{r})$ . Thus the electron wave function becomes

$$\psi(\mathbf{r}) = \exp(i\mathbf{k}_{\parallel} \cdot \boldsymbol{\rho}) \sum_{\boldsymbol{\kappa}} \phi_{\boldsymbol{\kappa}}(z) \exp(i\boldsymbol{\kappa} \cdot \boldsymbol{\rho}). \quad (3.3)$$

The diffracted intensities are found by solving the time-independent Schrödinger equation

$$\nabla^2 \psi(\mathbf{r}) + k^2 \psi(\mathbf{r}) = \frac{2m}{\hbar^2} V(\mathbf{r}) \psi(\mathbf{r}). \quad (3.4)$$

For high energy electrons, there are some small corrections to this equation caused by relativistic effects, which have been discussed by Maksym [52]. Substituting Eqs. (3.2) and (3.3) into Eq. (3.4) gives a coupled system of ordinary differential equations for the  $\phi_{\boldsymbol{\kappa}}(z)$ ,

$$\frac{d^2 \phi_{\boldsymbol{\kappa}}}{dz^2} + k_{\boldsymbol{\kappa}}^2 \phi_{\boldsymbol{\kappa}} = \frac{2m}{\hbar^2} \sum_{\boldsymbol{\kappa}'} V_{\boldsymbol{\kappa}-\boldsymbol{\kappa}'} \phi_{\boldsymbol{\kappa}'}, \quad (3.5)$$

where the  $k_{\boldsymbol{\kappa}}^2$  are the perpendicular components of diffracted wave vectors

$$k_{\boldsymbol{\kappa}}^2(z) = k^2 - |\mathbf{k}_{\parallel} + \boldsymbol{\kappa}|^2. \quad (3.6)$$

To calculate the RHEED intensities, it is necessary to solve Eqs. (3.5) for the wave function coefficients  $\phi_{\mathbf{\kappa}}$ .

### 3.1.2 The Scattering Potential

The coefficients of the Fourier expansion of the potential, Eq. (3.2), are given by the expression

$$V_{\mathbf{\kappa}}(z) = \frac{1}{A_{\parallel}} \int_{A_{\parallel}} V(\mathbf{r}) \exp(-i\mathbf{\kappa} \cdot \boldsymbol{\rho}) d\boldsymbol{\rho}, \quad (3.7)$$

where the integration is taken over the area of the real space surface unit cell. It is necessary to evaluate these coefficients in order to solve the equations (3.5).

For RHEED calculations, it is usual to write the total potential as the sum of atomic or ionic potentials

$$V(\mathbf{r}) = \sum_j \varphi(|\mathbf{r} - \mathbf{r}_j|), \quad (3.8)$$

$\mathbf{r}_j$  being the position vector of atom  $j$ . Although writing the potential in this form neglects the redistribution of charge due to chemical bonding, fast moving electrons are primarily scattered by the atomic nuclei and core electrons, and so equation (3.8) is expected to give a reasonably accurate description. Substituting this into Eq. (3.7) gives after some slight manipulation

$$V_{\mathbf{\kappa}}(z) = \frac{1}{A_{\parallel}} \sum_{\alpha} \exp(-i\mathbf{\kappa} \cdot \boldsymbol{\rho}_{\alpha}) \int \varphi(\boldsymbol{\rho}, z - z_{\alpha}) \exp(-i\mathbf{\kappa} \cdot \boldsymbol{\rho}) d\boldsymbol{\rho}, \quad (3.9)$$

where the summation index  $\alpha$  runs over atoms in the surface unit cell and the integration is now over the entire plane. Using the definition of the atomic form factor

$$\begin{aligned} f(\mathbf{q}) &= -\frac{1}{4\pi} \int U(\mathbf{r}) \exp(-i\mathbf{q} \cdot \mathbf{r}) d\mathbf{r} \\ &= -\frac{1}{4\pi} \frac{2m}{\hbar^2} \int \varphi(r) \exp(-i\mathbf{q} \cdot \mathbf{r}) d\mathbf{r}, \end{aligned} \quad (3.10)$$

$\mathbf{q}$  being the momentum transfer and  $U(\mathbf{r})$  the reduced potential, the expression for the potential coefficients can be re-written as

$$V_{\boldsymbol{\kappa}}(z) = -\frac{\hbar^2}{2m} \frac{4\pi}{A_{\parallel}} \sum_{\alpha} f_{\alpha}(\boldsymbol{\kappa}, z - z_{\alpha}) \exp(-i\boldsymbol{\kappa} \cdot \boldsymbol{\rho}_{\alpha}). \quad (3.11)$$

The quantities  $f_{\alpha}(\boldsymbol{\kappa}, z - z_{\alpha})$  in this expression are found from the definition

$$f_{\alpha}(\mathbf{q}_{\parallel}, z) = \frac{1}{2\pi} \int_{-\infty}^{\infty} f_{\alpha}(\mathbf{q}) \exp(iq_z z) dq_z, \quad (3.12)$$

and these must now be calculated to obtain the potential coefficients.

In the paper of Doyle and Turner [53], the form factor is represented as the sum of  $N$  Gaussian terms

$$f_{\alpha}(\mathbf{s}) = \sum_{i=1}^N a_i \exp(-b_i s^2), \quad (3.13)$$

and the parameters  $a_i, b_i$  tabulated for many neutral atoms and ions. Other authors have also published such parameters [54, 55, 56] which have become known as "Doyle-Turner coefficients". The scattering vector  $\mathbf{s}$  used by Doyle and Turner is related to the vector  $\mathbf{q}$  used above by  $\mathbf{s} = \mathbf{q}/4\pi$ . The effects of thermal motion are accounted for by multiplying the form factor by a Debye-Waller factor  $\exp(-M_{\alpha} s^2)$ , where the quantity  $M_{\alpha}$  is related to the mean square vibrational amplitude of atom  $\alpha$ , and can be found in the literature [54]. Including the Debye-Waller correction and using  $\mathbf{q}$  rather than  $\mathbf{s}$ , the form factor becomes

$$f_{\alpha}(\mathbf{q}) = \sum_{i=1}^N a_i \exp\left(-\frac{[b_i + M_{\alpha}]q^2}{16\pi^2}\right). \quad (3.14)$$

This form of  $f_{\alpha}(\mathbf{q})$  can be used in Eq. (3.12) and the integral performed analytically, giving the result

$$f_{\alpha}(\mathbf{q}_{\parallel}, z) = \sum_i^N 2a_i \left(\frac{\pi}{b_i + M_{\alpha}}\right)^{\frac{1}{2}} \exp\left(-\frac{[b_i + M_{\alpha}]q_{\parallel}^2}{16\pi^2}\right) \exp\left(-\frac{4\pi^2 z^2}{[b_i + M_{\alpha}]}\right). \quad (3.15)$$

The potential coefficients are obtained by using this expression for  $f_\alpha(\kappa, z)$  in Eq. (3.11).

The potential coefficients in Eq. (3.11) are real. Absorptive effects of the crystal are accounted for by having an imaginary component of the potential. All processes which can cause electrons to be scattered out of the Bragg beams into the inelastic background must be considered. Among such contributions are thermal vibrations of atoms (thermal diffuse scattering), statistical defects in the structure and electronic excitations. Each contributes to the imaginary potential in a different way making a fully quantitative analysis of absorption a difficult task, although calculations of the thermal diffuse scattering contribution have been made by Bird and King [57], and also by Dudarev *et al.* [54]. The general approach in high energy electron diffraction however is to approximate the imaginary potential by taking it to be proportional to the real part, and to treat the constant of proportionality as an adjustable parameter. The imaginary part is typically around 10% in RHEED calculations. This approach is used here, and so the coefficients of the full optical potential are given by

$$V_\kappa^{tot}(z) = (1 + ip)V_\kappa(z), \quad (3.16)$$

where  $V_\kappa(z)$  are the coefficients in Eq. (3.11), and  $p$  is the constant of proportionality.

### 3.1.3 The Scattering Matrix

Once the potential coefficients are known, the RHEED intensities can be found by the numerical solution of the coupled equations (3.5). The boundary conditions of the problem are that the  $\phi_\kappa(z)$  take the asymptotic form of the plane waves

$$\phi_\kappa(z) \sim \delta_{\kappa 0} \exp(-ik_\kappa z) + R_\kappa \exp(ik_\kappa z) \quad z \rightarrow \infty$$

$$\sim T_{\kappa} \exp(-ik_{\kappa}z) \quad z \rightarrow -\infty. \quad (3.17)$$

Above the upper surface ( $z \rightarrow \infty$ ) of the structure, this corresponds to an incident wave of unit amplitude and a set of reflected waves with amplitudes  $R_{\kappa}$ . Below the lower surface, there is a set of transmitted waves with amplitudes  $T_{\kappa}$ . To model the real situation of a surface layer on an infinitely thick substrate, the structure should be thick enough so that the transmitted amplitudes  $T_{\kappa}$  are very small.

To solve equations (3.5), it is convenient to make the substitution

$$\phi_{\kappa}(z) = Q_{\kappa}^{+}(z) \exp(ik_{\kappa}z) + Q_{\kappa}^{-}(z) \exp(-ik_{\kappa}z), \quad (3.18)$$

where the  $\phi_{\kappa}(z)$  have been written as the sum of upward and downward propagating waves with  $z$ -dependent amplitudes,  $Q_{\kappa}^{\pm}(z)$ . To uniquely define the  $Q_{\kappa}^{\pm}(z)$ , another relation is required. Choosing this relation to be

$$\exp(ik_{\kappa}z) \frac{dQ_{\kappa}^{+}}{dz} + \exp(-ik_{\kappa}z) \frac{dQ_{\kappa}^{-}}{dz} = 0 \quad (3.19)$$

means that second order derivatives of  $Q_{\kappa}^{\pm}(z)$  do not appear when (3.18) is substituted into (3.5). Introducing the definition (3.18) allows the scattering properties of the various "layers" in the structure to be described by a matrix formalism. A "layer" here is used to mean any two-dimensionally periodic slice of the structure. Consider one such layer in the structure, with top and bottom surfaces at  $z_t$  and  $z_b$  respectively. The vectors  $\mathbf{I}$  and  $\mathbf{R}$  are defined to be composed of ingoing and outgoing wave amplitudes at the upper surface ( $Q_{\kappa}^{-}(z_t)$  and  $Q_{\kappa}^{+}(z_t)$ ) and  $\mathbf{X}$ ,  $\mathbf{T}$  to be the ingoing and outgoing amplitudes at the lower surface ( $Q_{\kappa}^{+}(z_b)$  and  $Q_{\kappa}^{-}(z_b)$ ). The situation is illustrated in Fig. 3.1. The scattering properties of the layer can be described by a scattering matrix  $S$ , which relates

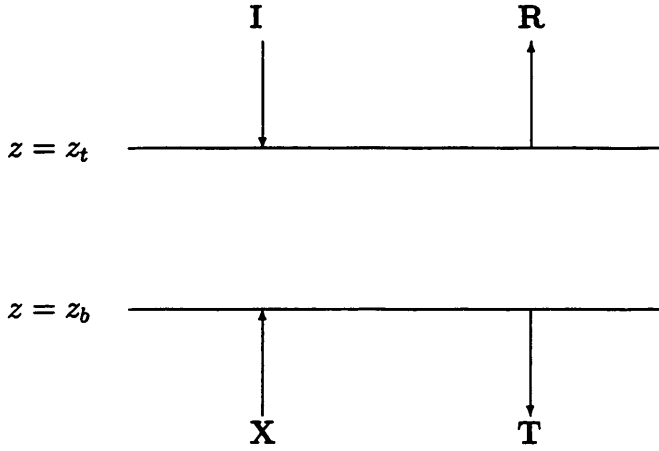


Figure 3.1: Schematic diagram of the wave amplitudes entering and leaving a layer. The vectors  $\mathbf{I}$  and  $\mathbf{R}$  are composed of the amplitudes  $Q_{\mathbf{k}}^-(z_t)$  and  $Q_{\mathbf{k}}^+(z_t)$  respectively, and  $\mathbf{X}$  and  $\mathbf{T}$  are composed of  $Q_{\mathbf{k}}^+(z_b)$  and  $Q_{\mathbf{k}}^-(z_b)$ .

the amplitudes of the beams entering the layer to those leaving it. Hence the scattering matrix is defined by

$$\begin{pmatrix} \mathbf{R} \\ \mathbf{T} \end{pmatrix} = \begin{pmatrix} S_1 & S_2 \\ S_3 & S_4 \end{pmatrix} \begin{pmatrix} \mathbf{X} \\ \mathbf{I} \end{pmatrix}. \quad (3.20)$$

In addition to the scattering matrix, it is necessary to define a further two matrices: the transfer matrix  $M$

$$\begin{pmatrix} \mathbf{R} \\ \mathbf{I} \end{pmatrix} = \begin{pmatrix} M_1 & M_2 \\ M_3 & M_4 \end{pmatrix} \begin{pmatrix} \mathbf{X} \\ \mathbf{T} \end{pmatrix}, \quad (3.21)$$

and its inverse  $N$

$$\begin{pmatrix} \mathbf{X} \\ \mathbf{T} \end{pmatrix} = \begin{pmatrix} N_1 & N_2 \\ N_3 & N_4 \end{pmatrix} \begin{pmatrix} \mathbf{R} \\ \mathbf{I} \end{pmatrix}. \quad (3.22)$$

Each of the four sub-matrices of  $M$ ,  $N$  and  $S$  contains  $n \times n$  elements, where  $n$  is the number of beams retained in the wave function expansion, Eq. (3.3). By substituting equations (3.18) and (3.19) into the coupled set (3.5), the differential

equations satisfied by the amplitudes  $Q_{\kappa}^{\pm}(z)$  can be found. From the paper of Maksym and Beeby [46], the solutions are

$$\begin{aligned} Q_{\kappa}^{+}(z) &= \frac{2m}{\hbar^2} \sum_{\kappa'} \int_{-\infty}^z \frac{k_{\kappa'}}{k_{\kappa}} Q_{\kappa'}^{+}(z'') \int_{z''}^z V_{\kappa-\kappa'}(z') \exp[-i(k_{\kappa} + k_{\kappa'})z'] dz' dz'' \\ &+ \frac{2m}{\hbar^2} \sum_{\kappa'} \int_{-\infty}^z \frac{Q_{\kappa'-\infty}^{-}}{2ik_{\kappa}} V_{\kappa-\kappa'}(z') \exp[-i(k_{\kappa} + k_{\kappa'})z'] dz', \end{aligned} \quad (3.23)$$

$$\begin{aligned} Q_{\kappa}^{-}(z) &= Q_{\kappa'-\infty}^{-} - Q_{\kappa'}^{+}(z) \exp(2ik_{\kappa}z) \\ &+ 2ik_{\kappa} \int_{-\infty}^z Q_{\kappa'}^{+}(z') \exp(2ik_{\kappa}z') dz'. \end{aligned} \quad (3.24)$$

The quantity  $Q_{\kappa'-\infty}^{-}$  is defined as  $\lim_{z \rightarrow -\infty} Q_{\kappa}^{-}(z)$ . From these two expressions it is possible to evaluate the elements of sub-matrices  $M_2$  and  $M_4$ . Starting at  $z_b$ , the bottom surface of the layer (taken to be  $-\infty$ ), the  $Q_{\kappa'-\infty}^{-}$  are set to  $\delta_{\kappa\kappa'}$ , and the integration upwards through the layer performed according to (3.23) and (3.24). At the upper surface, the  $Q_{\kappa}^{+}(z_t)$  form the  $\kappa$ th column of  $M_2$ , and the  $Q_{\kappa}^{-}(z_t)$  the  $\kappa$ th column of  $M_4$ . This corresponds to the amplitudes of the incident and reflected waves at the top surface required to give the transmitted amplitudes  $\delta_{\kappa\kappa'}$ . The integrations may be repeated for the different  $\kappa$  thus generating the remaining columns of  $M_2$  and  $M_4$ . The elements of  $N_1$  and  $N_3$  can be obtained from equations similar to (3.23) and (3.24) in which the integration is performed from the top surface (taken to be  $+\infty$ ) downwards through the layer. The columns of  $N_1$  and  $N_3$  are generated by repeatedly starting the integration with  $Q_{\kappa'+\infty}^{+} = \delta_{\kappa\kappa'}$  for all  $\kappa$ . It is a straightforward matter from equations (3.21) and (3.22) to show that the sub-matrices of  $S$  can be expressed in terms of the sub-matrices of  $M$  and  $N$  as

$$S = \begin{pmatrix} N_1^{-1} & M_2 M_4^{-1} \\ N_3 N_1^{-1} & M_4^{-1} \end{pmatrix}. \quad (3.25)$$

### 3.1.4 The Layer Doubling Method

In principle, it should be possible to compute the scattering matrix for a layer of arbitrary size by the integration procedure previously outlined. In practice however, the integration range which can be used is limited. From equation (3.6), it can be seen that for beams with large enough  $\kappa$ , the corresponding  $k_\kappa$  is imaginary. These so-called "evanescent" beams lead to components in the numerical integration which grow or decay exponentially. The exponentials eventually become too large or too small to represent on a machine with finite precision, and numerical accuracy is lost [52]. The solution to this problem is to divide the integration range into sections over which the integrations can be accurately performed. The scattering matrices for each section can then be found and combined using the layer doubling algorithm of LEED theory [58], which will be described here. Maksym [48] has shown that it is necessary to use the scattering matrix  $S$ , rather than the transfer matrices  $M$  and  $N$  for this combination process to be numerically stable. Consider two layers, labelled  $\alpha$  and  $\beta$ , with known scattering matrices  $S^\alpha$  and  $S^\beta$  respectively. The layer doubling algorithm allows the scattering matrix of the composite layer  $S^{\alpha\beta}$ , to be calculated by using the individual scattering matrices of the  $\alpha$  and  $\beta$  layers. If the  $\beta$  segment is stacked onto the  $\alpha$  segment as shown in Fig. 3.2, it can be seen that the individual scattering matrices by definition obey the equations

$$\begin{pmatrix} \mathbf{R} \\ \mathbf{W} \end{pmatrix} = S^\beta \begin{pmatrix} \mathbf{U} \\ \mathbf{I} \end{pmatrix}, \quad \begin{pmatrix} \mathbf{U} \\ \mathbf{T} \end{pmatrix} = S^\alpha \begin{pmatrix} \mathbf{X} \\ \mathbf{W} \end{pmatrix}, \quad (3.26)$$

and by considering the stacked layers as a single entity, that

$$\begin{pmatrix} \mathbf{R} \\ \mathbf{T} \end{pmatrix} = S^{\alpha\beta} \begin{pmatrix} \mathbf{X} \\ \mathbf{I} \end{pmatrix}. \quad (3.27)$$

The amplitudes at the common boundary are  $\mathbf{U}$  and  $\mathbf{W}$ . By expanding equations (3.26), the amplitudes  $\mathbf{U}$  and  $\mathbf{W}$  may be eliminated, and the four sub-matrices of  $S^{\alpha\beta}$  expressed in terms of the sub-matrices of  $S^\alpha$  and  $S^\beta$ :

$$\begin{aligned} S_1^{\alpha\beta} &= S_1^\beta (1 - S_2^\alpha S_3^\beta)^{-1} S_1^\alpha, \\ S_2^{\alpha\beta} &= S_2^\beta + S_1^\beta (1 - S_2^\alpha S_3^\beta)^{-1} S_2^\alpha S_4^\beta, \\ S_3^{\alpha\beta} &= S_3^\alpha + S_4^\alpha (1 - S_3^\beta S_2^\alpha)^{-1} S_3^\beta S_1^\alpha, \\ S_4^{\alpha\beta} &= S_4^\alpha (1 - S_3^\beta S_2^\alpha)^{-1} S_4^\beta. \end{aligned}$$

These four equations allow the scattering matrix of a stack consisting of any number of segments to be found, and so the integration range is no longer limited. Hence in principle, the integration can be performed through the entire system of surface and substrate. In practice however it is possible to take advantage of the substrate consisting of identical layers of unit cells. To calculate the substrate scattering matrix, only the scattering matrix for one of the unit cell layers needs to be computed. Once the unit cell scattering matrix is known, it can be used together with the layer doubling algorithm (since  $S^\alpha = S^\beta$ ) to generate the scattering matrix of two layers of unit cells. Repeating this procedure gives the scattering matrix of a stack of four unit cell layers, then eight, sixteen and so on. The process converges rapidly providing the system is absorbing, giving the substrate scattering matrix in a substantially reduced CPU time compared with direct integration. The scattering matrix for the surface is computed separately, and finally the layer doubling algorithm is used again to generate the system scattering matrix from the surface and substrate matrices.

When the system scattering matrix has been calculated, it is a simple task to evaluate the reflection coefficients. The boundary conditions in Eq. (3.17) dictate that there are no waves incident at the bottom surface of the structure ( $\mathbf{X} = \mathbf{0}$ ),

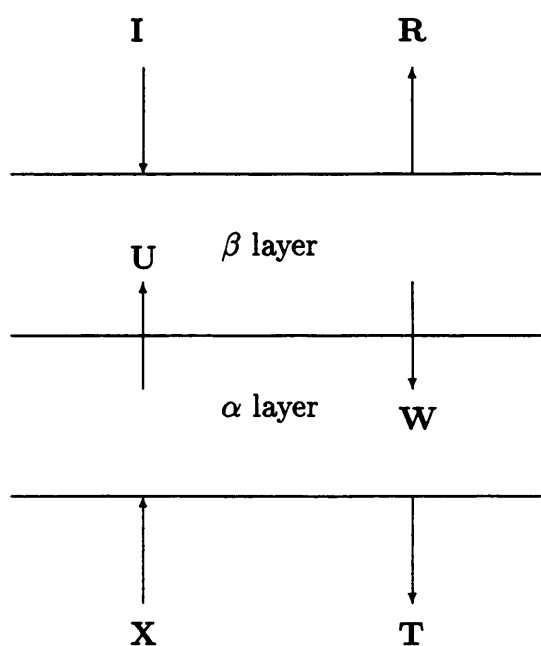


Figure 3.2: Schematic diagram of the layer doubling method. The scattering matrices for the  $\alpha$  and  $\beta$  sections are calculated separately. The layer doubling algorithm is then used to find the composite  $\alpha\beta$  scattering matrix.

and the vector containing the incident amplitudes  $\mathbf{I}$  has elements  $\delta_{\mathbf{\kappa}0}$ . Hence the reflected amplitudes  $\mathbf{R}$  can be readily obtained from the definition (3.20). Finally, the flux reflection coefficients are given by  $|R_{\mathbf{\kappa}}|^2 \text{Re}(k_{\mathbf{\kappa}})/k_0$ .

### 3.2 Application to XPD Calculations

In chapter 2, it was shown that the XPD pattern depends on the calculation of the matrix elements  $\mathbf{R}_{mj}$  defined in Eq. (2.4), the matrix elements of  $\mathbf{r}$  between an initial bound state and a time-reversed RHEED state. The important quantities required to evaluate the  $\mathbf{R}_{mj}$  are the  $\mathbf{P}_{m\mathbf{\kappa}j}$ , which were defined in Eq. (2.18). Each component of  $\mathbf{P}_{m\mathbf{\kappa}j}$  was reduced from a three dimension to a one dimensional integral by analytically performing the integrations parallel to the surface. The numerical evaluation of the remaining integrals is dealt with in this section, and entails the modification of the RHEED computer program.

#### 3.2.1 The RHEED Computer Program

The XPD calculation has been performed by evaluating the quantities  $\mathbf{P}_{m\mathbf{\kappa}j}$  via a modified version of a RHEED computer code. The RHEED program of Maksym essentially follows the theory of Maksym and Beeby presented in this chapter. The slight difference is that instead of working with the amplitudes  $Q_{\mathbf{\kappa}}^+(z)$  and  $Q_{\mathbf{\kappa}}^-(z)$ , the program works with the new variables

$$\begin{aligned}\bar{\psi}_{\mathbf{\kappa}}^+(z) &= Q_{\mathbf{\kappa}}^+(z) \exp(ik_{\mathbf{\kappa}}z), \\ \bar{\psi}_{\mathbf{\kappa}}^-(z) &= Q_{\mathbf{\kappa}}^-(z) \exp(-ik_{\mathbf{\kappa}}z).\end{aligned}$$

This change means that the expansion coefficients of the final state wave function,  $\phi_{\mathbf{\kappa}}$  are now given by

$$\phi_{\mathbf{\kappa}}(z) = \bar{\psi}_{\mathbf{\kappa}}^+(z) + \bar{\psi}_{\mathbf{\kappa}}^-(z), \quad (3.28)$$

and the scattering matrices now relate the "ingoing" values of  $\overline{\psi}_{\mathbf{k}}^{\pm}$  to the "outgoing" values.

The size, composition and structure of the unit cell, the potential data, the direction of beam incidence, the beam set and the operational mode of the calculation (polar or azimuthal scan) are all read in from an input file. As well as allowing the beams in the calculation to be input manually via their labels  $l, m (= l\mathbf{a}^* + m\mathbf{b}^*)$ , there is also an option which allows an area of reciprocal space to be selected. The program then selects all beams within that area for the calculation. The RHEED calculation for a single point proceeds as follows:

- read input data
- select beam set for calculation (if "area" option used)
- calculate Fourier components of the potential which couple beams
- calculate substrate unit cell  $S$ -matrix
- use layer doubling algorithm to convert unit cell  $S$ -matrix to full substrate  $S$ -matrix
- calculate surface  $S$ -matrix
- use layer doubling to combine surface and substrate  $S$ -matrices into system  $S$ -matrix
- find reflection coefficients from system  $S$ -matrix.

If the program is used to calculate the reflection coefficients as a function of polar angle, the beam set and the potential coefficients remain the same for all points, and only the  $S$ -matrix calculations need be repeated for each point. In the

azimuthal mode, the required beam set may change from point to point, so the required beams need to be re-selected and the potential coefficients re-calculated before the  $S$ -matrix calculations.

### 3.2.2 Matrix Element Integrals (i): A Simplified Case

In order to perform the XPD calculation several modifications have been made to the RHEED computer program. From Eq. (2.38), it can be seen that for the XPD calculation it is necessary to numerically accumulate integrals of the type

$$\int \phi_{\kappa}(z) g_{m\kappa}^i(z) dz. \quad (3.29)$$

The function  $g_{m\kappa}^i(z)$  is one of the modulation functions defined in Eq. (2.39), where  $i$  stands for  $x$ ,  $y$  or  $z$ . Although the exact form of  $g_{m\kappa}^i(z)$  depends on several parameters, it is always strongly localised around the emitter. Since the short inelastic scattering length means that even for bulk emission the elastic signal comes from the top few atomic layers only, the matrix element integrations are localised to the surface region. This is convenient from a computational point of view as the substrate  $S$ -matrix can be calculated exactly as it is done in the RHEED calculation. All emitting layers can be put into the "surface" part of the calculation and the required integrals accumulated during the calculation of the surface  $S$ -matrix.

Calculating the required matrix element integrals is complicated by the presence of strong evanescent beams. In such cases the RHEED program splits its integration range into segments small enough to cope with them, calculates the  $S$ -matrix for each segment in turn and uses the layer doubling algorithm to accumulate the  $S$ -matrix of the entire region. Unfortunately this process makes the matrix element integrals more difficult to extract as will be shown in the

following section. Hence as a simplified example to illustrate the underlying technique, the "ideal" case will be dealt with first: that is, a case where the integration range of the RHEED program is unlimited. Such a case would be a calculation including only propagating beams. Having introduced the method via this simplified example, it will be extended to cope with the realistic case in the next section.

In the RHEED computer program, the  $\phi_{\kappa}(z)$  are never explicitly calculated, however it is possible to see how integrals of the type (3.29) may be determined by means of a simple example. Consider photoemission from one ordered plane of atoms. The photoelectron final state is derived from the diffraction of an incident electron beam by the plane of atoms. Assuming that the range for numerical integration is unlimited, the reflected and transmitted waves can be obtained from the transfer matrix definition (3.21)

$$\mathbf{I} = M_4 \mathbf{T} \quad \mathbf{R} = M_2 \mathbf{T}, \quad (3.30)$$

since it is known from the boundary conditions that the elements of  $\mathbf{I}$  are  $\delta_{\kappa 0}$  and those of  $\mathbf{X}$  are all zero. The elements of vectors  $\mathbf{I}$  and  $\mathbf{R}$  can be directly equated with  $\bar{\psi}_{\kappa}^{-}(z \rightarrow +\infty)$  and  $\bar{\psi}_{\kappa}^{+}(z \rightarrow +\infty)$ . Hence if  $\phi$  is a vector composed of the  $\phi_{\kappa}(z)$ , from (3.28), the limiting value of  $\phi$  is

$$\phi(z \rightarrow +\infty) = M_2 \mathbf{T} + M_4 \mathbf{T} = (M_2 + M_4) \mathbf{T}.$$

The matrices which in the limit become  $M_2$  and  $M_4$ , are known at each integration step of the  $S$ -matrix calculation, since it is their elements which are repeatedly incremented during the integration. Denote their values at some general point in the integration by  $M_2(z)$  and  $M_4(z)$ . The vector  $\mathbf{T}$  can only be found at the end of the integration by solving equations (3.30), and so it is not possible to

determine  $\phi$  at some general point. It is possible for an integral of the type (3.29) to be found however. If the matrix

$$\int [M_2(z) + M_4(z)] g_{m\kappa}^i(z) dz \quad (3.31)$$

is accumulated during the integration through the layer, and the vector  $\mathbf{T}$  determined using the final values of  $M_2$  and  $M_4$ , the vector then obtained by performing

$$\left[ \int [M_2(z) + M_4(z)] g_{m\kappa}^i(z) dz \right] \mathbf{T}$$

has elements

$$\int \phi_{\kappa}(z) g_{m\kappa}^i(z) dz.$$

To summarise this example then, in order to compute integrals of the form (3.29), the matrix  $[M_2(z) + M_4(z)] g_{m\kappa}^i(z)$  should be treated as the integrand. At the end of the integration, the vector  $\mathbf{T}$  can be found, and when multiplied by the integrated matrix, yields a vector  $\phi$  whose elements are the required integrals (3.29).

It is quite straightforward to extend this method to calculate the  $\phi_{\kappa}(z)$  integrals. Consider now the same plane of emitting atoms adsorbed onto a semi-infinite substrate. It is convenient to split the structure into a "surface" region which contains the emitting layer, and a "bulk" part. The photoelectron final state this time is derived from the diffraction of an incident electron beam by the full structure. The total wave field in the surface is the combination of the incident wave at the upper boundary and the waves backscattered from the bulk incident at the lower boundary. The situation is shown in Fig. 3.3. In the RHEED program, during the surface  $S$ -matrix calculation, the transfer matrices  $M_2$  and  $M_4$  are calculated as in the previous example, by integrating from the surface-bulk interface up through the layer. In addition to this, the matrices  $N_1$  and  $N_3$

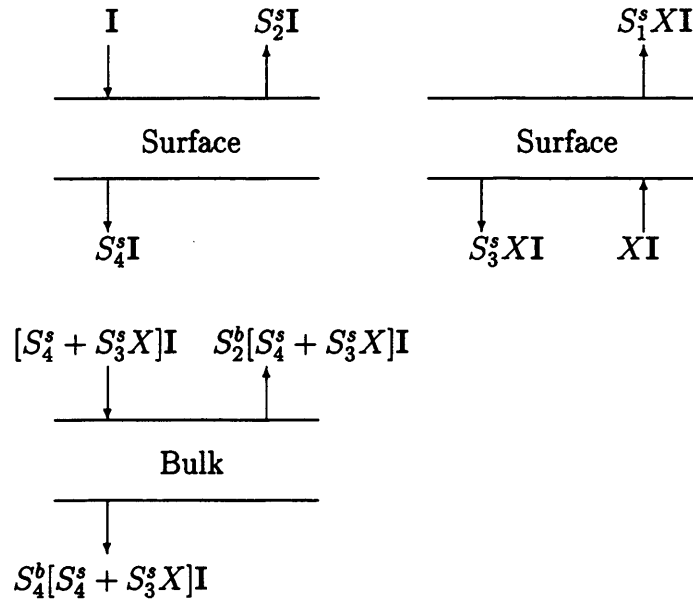


Figure 3.3: Determination of the waves entering and leaving the surface and bulk layers using the surface (superscript s) and bulk (superscript b) scattering matrices. To calculate the integrals involving the  $\phi_{\kappa}(z)$  over the surface layer, the waves leaving the layer must be known. The surface region is shown in two parts to highlight the contribution of the backscattering from the bulk region. Matrix  $X$  is defined in Eq. (3.33)

are calculated by integrating over the same region in the opposite direction. The prescription to find integrals of the type (3.29) requires the "transmitted" waves ( $\mathbf{T}$  in previous example) to be known. Referring to Fig. 3.3, the upper left diagram corresponds to the  $M_2/M_4$  calculation, and the transmitted waves are given by the surface scattering matrix definition as  $S_4^s \mathbf{I}$ . The upper right diagram corresponds to the  $N_1/N_3$  calculation, but finding the transmitted waves is slightly more complicated. The waves entering the surface layer at the surface/bulk interface have been defined as  $X\mathbf{I}$ , where  $X$  is an unknown matrix. The waves entering and leaving the various layers have been labelled by using the scattering matrix

definitions and  $X$ . Clearly, the waves leaving the bulk region are the same waves which enter the surface region at the lower boundary, that is

$$S_2^b(S_4^s + S_3^s X)\mathbf{I} = X\mathbf{I}, \quad (3.32)$$

and solving this equation for  $X$  gives

$$X = (1 - S_2^b S_3^s)^{-1} S_2^b S_4^s. \quad (3.33)$$

Thus the transmitted waves for the upper right diagram are

$$S_1^s(1 - S_2^b S_3^s)^{-1} S_2^b S_4^s \mathbf{I}. \quad (3.34)$$

Hence the problem is solved: for each modulation function  $g_{m\kappa}^i(z)$  the matrices

$$\int [M_2(z) + M_4(z)] g_{m\kappa}^i(z) dz, \quad \int [N_1(z) + N_3(z)] g_{m\kappa}^i(z) dz \quad (3.35)$$

are accumulated, and after the integrations, multiplied by the "transmitted" waves

$$S_4^s \mathbf{I}, \quad S_1^s(1 - S_2^b S_3^s)^{-1} S_2^b S_4^s \mathbf{I} \quad (3.36)$$

respectively. If the resulting vectors are denoted  $\phi^M$  and  $\phi^N$  to indicate the matrices used in the integration, then the elements of  $[\phi^M + \phi^N]$  are the required integrals

$$\int \phi_{\kappa}(z) g_{m\kappa}^i(z) dz.$$

### 3.2.3 Matrix Element Integrals (ii): Realistic Case

The previous section developed a method to calculate the required integrals for the XPD calculation using the RHEED program, with the assumption that the surface  $S$ -matrix could be calculated using a single integration range. In a realistic calculation however the surface  $S$ -matrix integration range can be split into

smaller segments over which it is possible to accurately represent the strongest evanescent waves on the computer. The method of the previous section needs to be modified to handle such cases.

When the surface integration range contains more than one segment, the surface  $S$ -matrix is generated by repeating the process of calculating a segment  $S$ -matrix and using layer doubling to combine it with the others. In such a case the method given in 3.2.2 cannot be used: although the matrix integrals, Eq. (3.35) can be performed, the linear combinations required (i.e. the "transmitted" waves) would be needed for each individual segment. Calculating these would require knowing the remainder of the surface  $S$ -matrix, a quantity which has not been calculated at that point. This clearly poses a problem, especially if the whole range of the surface  $S$ -matrix calculation contributed to the matrix element integrals in Eq. (2.38). Fortunately though, the modulation function  $g_{m\kappa}^i(z)$  is strongly localised around  $z = 0$  and only a small part of the whole integration range contributes significantly to the integrals.

A convenient solution to the problem is to take advantage of the strong localisation of the  $g_{m\kappa}^i(z)$ . The surface integration range can be divided into three regions: a central part around  $z = 0$  which contributes to the integrals in Eq. (2.38), and regions above and below where the  $g_{m\kappa}^i(z)$  is small enough to render the contributions from these regions negligible. The central region is usually small enough to be handled with one integration segment, and the other two regions may contain any number of segments. The matrix integrations, Eq. (3.35) are performed in the central region, leaving the problem of determining the linear combinations required to go with them. As shown in the previous section, these quantities are the waves leaving that region. Fig. 3.4 is a schematic

Figure 3.4: The division of the surface integration range into three segments for a general beam set. The superscripts on the scattering matrices indicate the segment they represent. The matrix element integrals are performed in segment (b), so the important quantities are the waves leaving (b). The matrices  $M, M', M'', X, X'$  and  $X''$  are defined in Eq. (3.37).

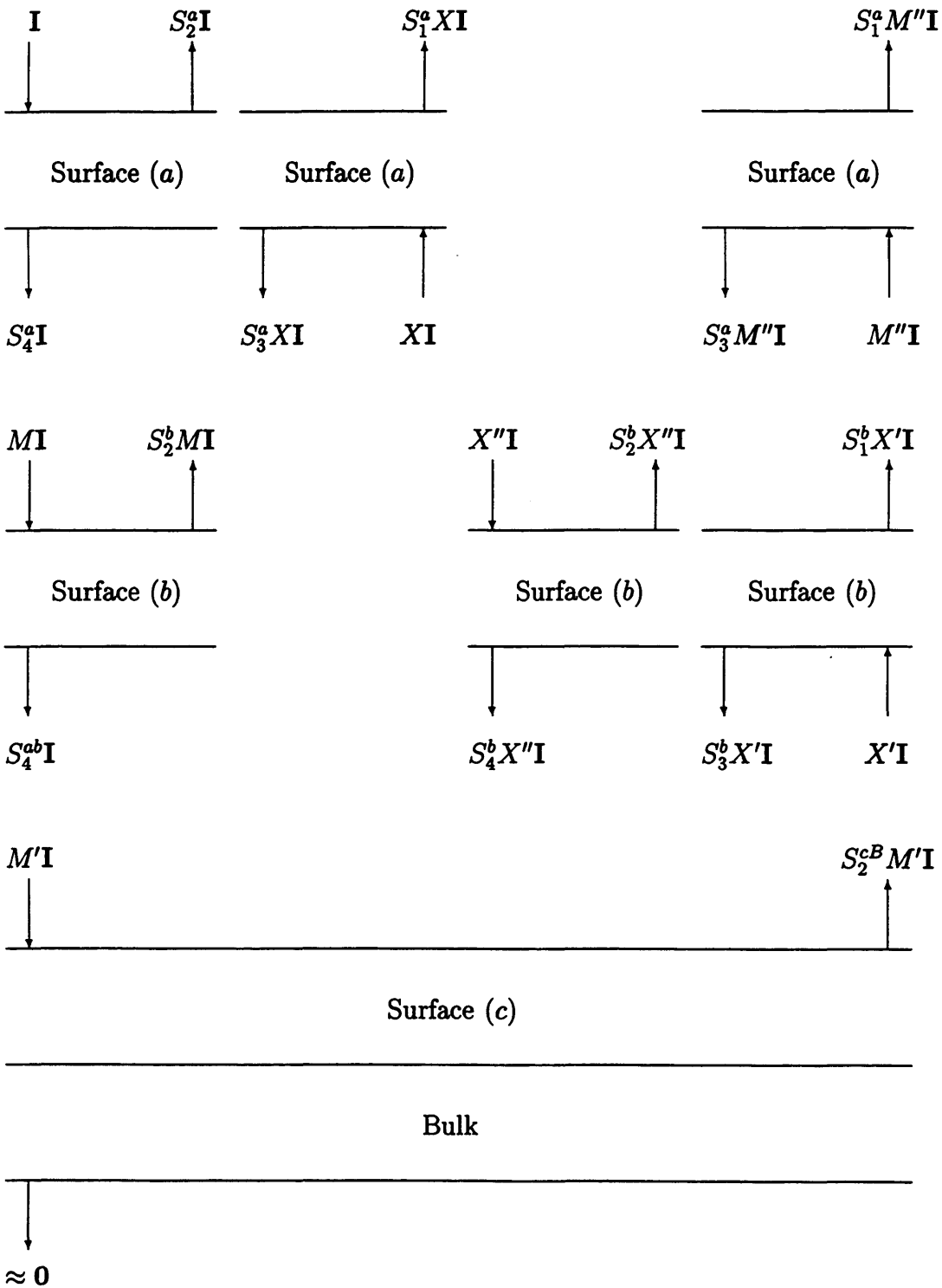


diagram showing the division of the integration range into three segments, labelled (a), (b) and (c). The waves entering and leaving each segment can be easily found by applying the method used in 3.2.2 to a three-layer system, and in Fig. 3.4 are written in terms of the matrices

$$\begin{aligned}
X &= (1 - S_2^b S_3^a)^{-1} S_2^b S_4^a \\
X' &= (1 - S_2^{cB} S_3^{ab})^{-1} S_2^{cB} S_4^{ab} \\
X'' &= (1 - S_3^a S_2^b)^{-1} S_3^a S_1^b X' \\
M &= (1 - S_3^a S_2^b)^{-1} S_4^a \\
M' &= (1 - S_3^{ab} S_2^{cB})^{-1} S_4^{ab} \\
M'' &= (1 - S_2^b S_3^a)^{-1} S_1^b X'.
\end{aligned} \tag{3.37}$$

The superscripts on the  $S$ -matrices in (3.37) denote the corresponding segment in the surface ( $B$  denotes the bulk region). The important quantities in Fig. 3.4 are the waves leaving region (b), which can be seen to be

$$\begin{aligned}
\mathbf{T}_1 &= S_4^{ab} \mathbf{I} \\
\mathbf{T}_2 &= S_4^b X'' \mathbf{I} \\
\mathbf{T}_3 &= S_1^b X' \mathbf{I}.
\end{aligned} \tag{3.38}$$

So, if the quantities

$$\phi^M = \left( \int [M_2^b(z) + M_4^b(z)] g_{m\kappa}^i(z) dz \right) (\mathbf{T}_1 + \mathbf{T}_2) \tag{3.39}$$

and

$$\phi^N = \left( \int [N_1^b(z) + N_3^b(z)] g_{m\kappa}^i(z) dz \right) \mathbf{T}_3 \tag{3.40}$$

are evaluated, then the elements of the vector  $[\phi^M + \phi^N]$  are the required integrals, Eq. (3.29).

The inclusion of stronger and stronger evanescent beams in the calculation have the effect of shortening the maximum integration range. It is possible that the central segment, (b) in Fig. 3.4 over which the modulation functions are significant, exceeds the maximum integration range. A method which allows segment (b) to be composed of two segments has been devised to solve this problem, which uses a double application of the previous three-segment method. For all calculations performed, the extent of the (b) region has never required more than two integration segments. The method can be extended to allow segment (b) to be composed of even more segments, but will become more computationally demanding due to the need to store more matrices or to recalculate some.

### 3.2.4 The XPD Calculation

It is now possible to calculate the components of  $\mathbf{P}_{m\kappa j}$  as defined in Eq. (2.38), shown below

$$\mathbf{P}_{m\kappa j} = \begin{pmatrix} \int \phi_{\kappa}(z) g_{m\kappa}^x(z - z_j) dz \\ \int \phi_{\kappa}(z) g_{m\kappa}^y(z - z_j) dz \\ \int \phi_{\kappa}(z) g_{m\kappa}^z(z - z_j) dz \end{pmatrix}.$$

There are at least three different  $g_{m\kappa}^i(z - z_j)$ , where  $i$  denotes  $x, y$  or  $z$ . This number increases for initial orbitals with  $l \neq 0$  as the magnetic quantum number  $m$  may take on  $2l + 1$  different values, and for surfaces containing  $j$  emitters at different depths  $z_j$ . For each distinct modulation function, vectors  $\phi^M$  and  $\phi^N$  must be calculated, as defined in Eqs. (3.39) and (3.40). Fortunately, although the number of modulation functions required can become quite large for  $l \neq 0$ , a separate pair of integration matrices as defined in Eq. (3.35) is not required for each. The full set of modulation functions can always be generated from linear combinations of a much smaller set of functions. Using this smaller set instead of

the full set greatly reduces the amount of memory needed. The various  $\phi^M$  and  $\phi^N$  can then be generated by taking the corresponding linear combination of the smaller set of integrals. The elements of the vector  $[\phi^M + \phi^N]$  are the  $\kappa$  different integrals for the modulation function. Hence the  $\mathbf{P}_{m\kappa j}$  can be calculated for all  $m$ ,  $\kappa$ , and  $j$ , and the matrix elements  $\mathbf{R}_{mj}$  found from Eq. (2.19). The required intensity can then be calculated by the method given in section 2.4.1.

## Chapter 4

### Initial Calculations

Chapters 2 and 3 have set out the basic theoretical framework for this type of XPD calculation and shown how a RHEED computer program can be modified to perform it. In practice however, the application of the method may be limited by the number of basis states required in the calculation. As has been mentioned elsewhere in the thesis, multiple scattering calculations involving electrons in the XPD energy range of roughly 500-1500eV are notoriously difficult: the energy lies between the low and high energy limits, so calculations using spherical or plane wave expansions will require more basis states than in the limiting cases. This chapter is concerned with the application of the XPD calculation at energies of around 1000eV, which is relatively low compared with typical RHEED energies. First the validity of the high energy Doyle-Turner potential is investigated at XPD energies. The important question of convergence is then addressed by means of trial convergence calculations on experimental systems, and the limitations of the method identified.

## 4.1 The Doyle-Turner Potential

There are several problems involved in performing RHEED-type calculations at lower energies. One such problem is the scattering potential of the crystal. The method used to calculate the coefficients in the 2-D Fourier expansion of Eq. (3.2) of the potential in RHEED has been outlined in chapter 3. This approach makes use of the tabulated representation of the atomic form factor provided by Doyle and Turner [53] to find the real part of each coefficient, and the imaginary part then taken to be proportional to the real part. Potentials derived from the tabulations of Doyle and Turner are known as Doyle-Turner (DT) potentials. A potential constructed this way is independent of electron energy. Strictly however there is an energy dependent contribution to the potential, which is very small energies of several keV, meaning the Doyle-Turner representation is an excellent one for applications such as RHEED. The aim of this section is to investigate how valid the DT potential is at energies in the XPD range.

The standard procedure for calculating the potential for low energy electrons has been given by Pendry [58]. The basic method is to divide the crystal into "muffin tins", the largest possible non-overlapping spheres which can be drawn around the atoms. Each atom is assumed to be spherically symmetric, and the core electronic wave functions modified so that it is electrically neutral within the muffin tin. A Schrödinger equation can be written down for the many-body system of core electrons and incident electron within a muffin tin. The core part of the wave function can be eliminated since the individual atomic core wave functions are known and are not easily polarised, which leaves an equation governing the motion of the incident electron. The equation expresses the direct, or Hartree potential, which is the electrostatic potential due to the core electrons

plus the nucleus, and the exchange potential in terms of the core state wave functions. Computer programs such as MUF POT are available to calculate these potentials [59].

The concern is that the DT potential, while valid for high electron energies, is not a good representation in the XPD range. To check the validity of the DT potential, the DT atomic potentials is compared with the calculated energy dependent potential. It is a straightforward matter to obtain the atomic DT potential. Fourier transformation of the form factor in Eq. (3.10) gives

$$\varphi(r) = -4\pi \frac{\hbar^2}{2m} \frac{1}{(2\pi)^3} \int f(\mathbf{q}) \exp(i\mathbf{q} \cdot \mathbf{r}) d\mathbf{q}. \quad (4.1)$$

The DT representation of  $f(\mathbf{q})$ , Eq. (3.14) can be used in Eq. (4.1) allowing the integrations to be performed analytically, giving the DT atomic potential as

$$\varphi(r) = -\frac{16\pi\hbar^2}{m} \sum_i^N a_i \left(\frac{\pi}{b_i}\right)^{\frac{3}{2}} \exp(-4\pi^2 r^2/b_i). \quad (4.2)$$

The full potential has been calculated by the computer program MUF POT. By making the unit cell dimension and the muffin-tin radius of the calculated potential unrealistically large, the free-atom potential for a particular energy can be obtained. This may then be compared with the DT potential from Eq. (4.2).

Fig. 4.1 is a comparison between the two potentials: the solid line is the calculated potential for a Cu atom at 1100eV, and the line with diamonds is the DT potential. The DT potential can be seen to fit well to the calculated potential. The small discrepancies between the two can be attributed to the energy dependence of the calculated potential, held completely in the exchange term. This exchange contribution to the potential, has been calculated by MUF POT as described above for four different electron energies. These are shown in Fig. 4.2 with the Hartree potential shown for reference. It is clear from

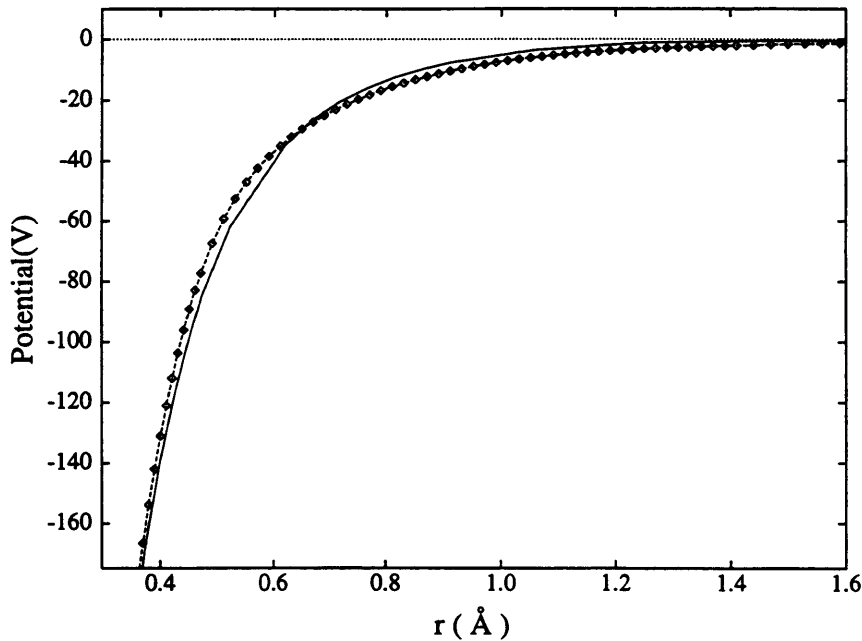


Figure 4.1: Comparison between a calculated potential of a 1100eV electron in a Cu atom (solid line) including exchange and correlation effects, and the analytic form given by the Doyle-Turner expression in Eq. (4.2), (line with diamonds).

these results that as the electron energy is reduced, the exchange contribution becomes more significant, and hence the DT potential becomes less accurate. For calculations around the 1000eV range and above however, the exchange correction can be seen to be small and therefore the DT potential is still a very good representation. Hence it can be assumed that no major errors will arise at energies in the higher part of the XPD energy range by using the DT potential.

## 4.2 Convergence

As has been described in earlier chapters, the final state wave function of the photoelectron is taken to be a time-reversed RHEED state and is written as the expansion (2.12). Although in principle this expansion is over the infinite

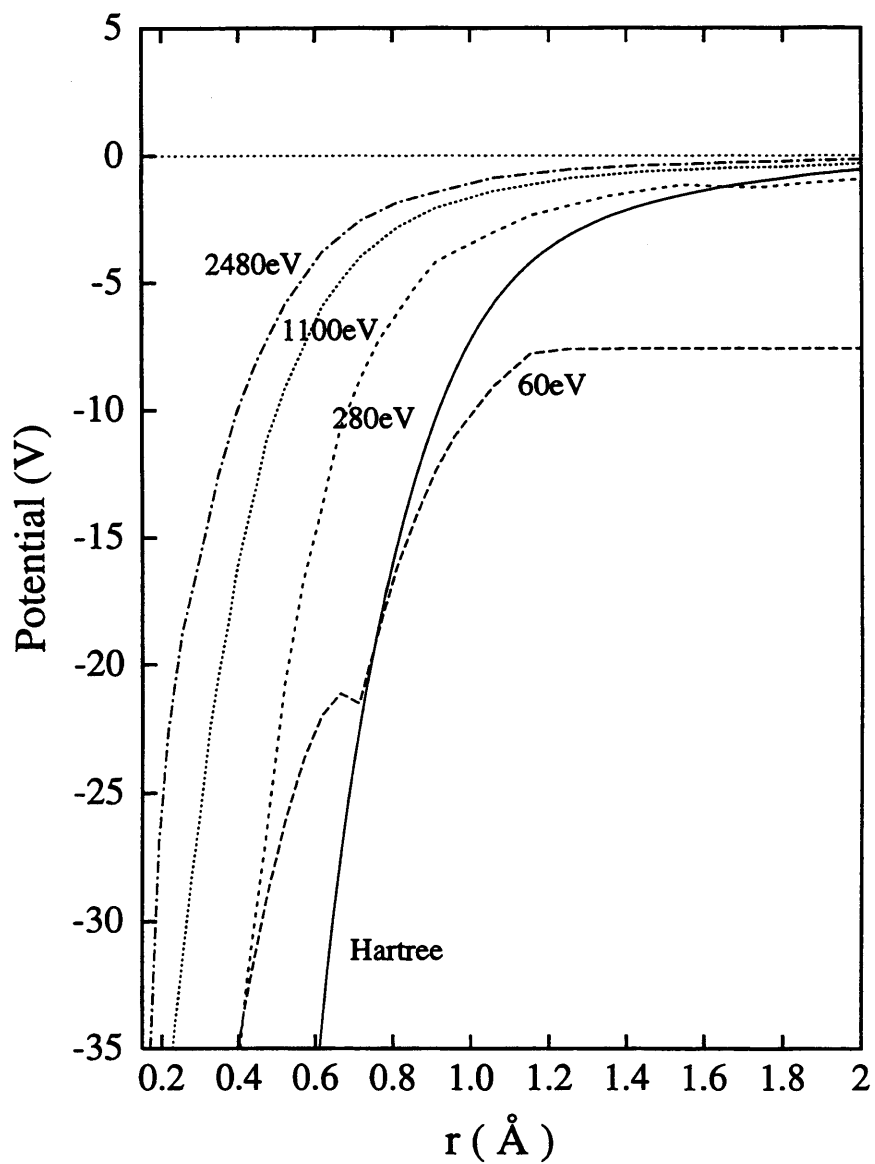


Figure 4.2: The exchange and correlation contribution to the potential plotted for different electron energies. The Hartree potential, which is the classical electrostatic potential and is energy independent, is shown for reference.

set of reciprocal mesh vectors  $\kappa$ , the series may be truncated after a certain number, when the addition of further terms does not affect the results of the calculation. The calculations are said to be converged when this condition is satisfied. The question of convergence is an important one, since when there is a quantitative comparison with experimental data, an unconverged calculation can lead to incorrect structural conclusions. At RHEED energies of 10keV and above, the expansion (2.11) converges very quickly for simple surfaces, that is, only a few terms ("beams") are required. Such calculations are very efficient, requiring only modest amounts of memory. For XPD calculations in the the 1000eV range, a significantly larger number of beams must be included to achieve convergence. The problem to be addressed here is the applicability of this method of XPD: can convergent calculations actually be performed at energies of 1keV or lower? Of course the expansion will always converge if enough beams are taken, but the calculations escalate in computational effort as  $n^3$ , where  $n$  is the number of beams. The XPD calculation also requires more memory than the RHEED calculation: it was shown in chapter 3 that to compute the required matrix elements, a number of matrices must be integrated over part of the surface region. Clearly then a decision must be made as to whether it would be computationally feasible to perform calculations for a given system.

It is difficult to estimate how many beams are required for a particular calculation. The number depends upon the final energy of the photoelectron, the direction in which it is observed (azimuthal angle and take-off angle) and the constituent atoms of the structure, and hence a convergent beam set can only be determined by trial calculations. Two different adsorbate systems will be considered here, both have been studied experimentally by XPD and have final

photoelectron energies approaching 1000eV. They therefore represent potential systems for which this method could be applied. The convergence tests have been carried out in a systematic way. First, beams with the  $\kappa$  vector perpendicular to  $k_{\parallel}$  were included. These beams form the zeroth Laue zone, and correspond to the semi-circle containing the specular spot in a RHEED pattern. It is known from RHEED calculations that beams in this zone tend to be the most important. Once convergence in this zone is found, increasingly higher order zones are included until the full calculation converges. At RHEED energies, the beam set is asymmetric in that only a small number of Laue zones are required compared with the number of beams within each zone. As the energy is lowered down to 1000eV, an increasing number of Laue zones are required to attain convergence. It is worth noting that in the following calculations, all zones contain roughly equal numbers of beams. In practice, the higher order zones may need fewer beams than the lower ones, allowing the full beam set to be reduced.

#### 4.2.1 Ni(001)<sub>c</sub>(2 × 2)O

The surface structures of oxygen adsorbed on the Ni(001) surface has been studied experimentally by many different techniques, and the system will be treated in greater depth in chapter 6. Saiki *et al.* [19] have conducted experiments in which the O 1s core level has been excited by Al K $\alpha$  radiation, giving rise to photoelectrons outside the structure having an energy of 954eV. The trial calculations have been performed for the oxygen overlayer adsorbed 0.8Å above a bulk terminated Ni(001) substrate. The oxygen atoms have been situated in fourfold hollow sites, and the take-off angle set at  $\theta = 11^\circ$ .

The convergence of the calculation can be clearly seen if the calculated intensity

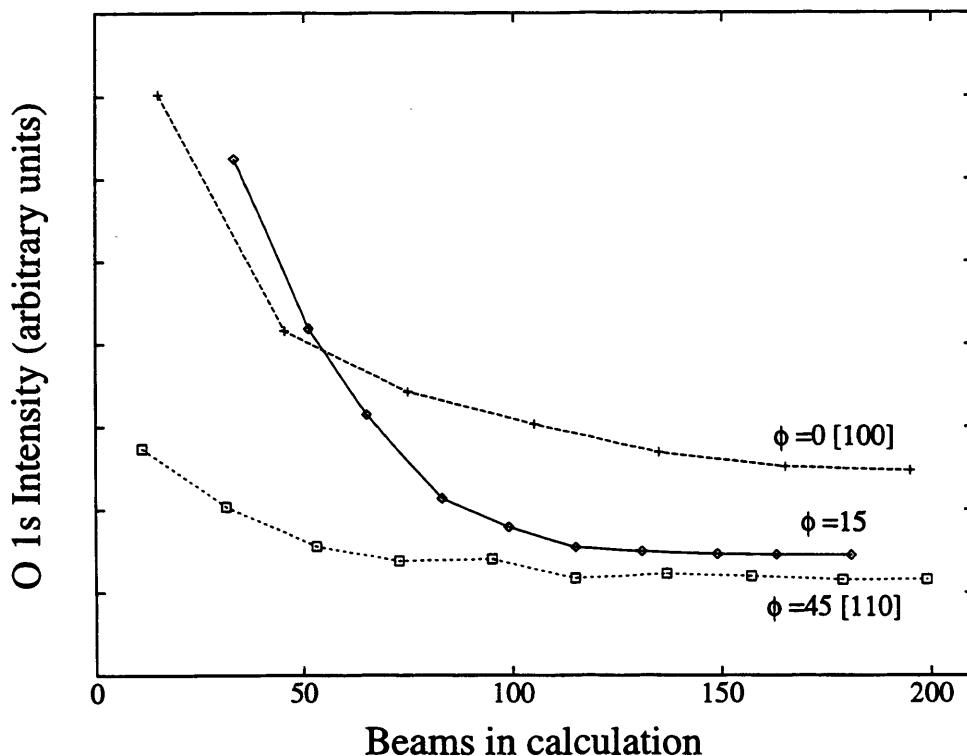


Figure 4.3: Calculated XPD intensities from the O 1s core level of  $c(2 \times 2)O/Ni(001)$  for various different beam sets. Calculations at the three azimuthal angles shown can all be seen to converge to asymptotic values for large beam sets. (Photoelectron energy=954eV)

at a given point is plotted against the number of beams included. This is shown for three different points  $\phi = 0^\circ$ ,  $15^\circ$  and  $45^\circ$  in Fig. 4.3,  $\phi$  being the azimuthal angle measured from [100]. It is known from RHEED calculations that symmetry azimuths normally require more beams due to enhanced multiple scattering effects [60]. The calculations in directions [100] and [110] should therefore represent a worst case for convergence. All three curves can be seen to converge to asymptotic values as more beams are included, the number of beams required being about 150. As a rough guide to the CPU time required to perform a set of calculations for this structure, calculations involving 150 beams require approximately 27 minutes per point on a HP735 workstation. The available XPD data is in the form

of azimuthal scans for various polar angles, requiring calculations to be performed over a  $45^\circ$  azimuthal wedge. Using these figures, a single azimuthal curve would require roughly 20 hours CPU time, sampling every 1 degree. This figure can be reduced to  $\approx 15$  hours (20 minutes/point) by removing some superfluous beams from the higher zones, as described earlier.

These trial calculations show that it is possible to perform convergent calculations on this particular system. The CPU time required of approximately 20 minutes per point is well within the capabilities of the computing resources available, and short enough to enable calculations to be repeated for different surface parameters in order to find the optimum agreement with experimental data.

#### 4.2.2 Si(111)- $\sqrt{3} \times \sqrt{3}$ Sb

The Si(111)- $\sqrt{3} \times \sqrt{3}$  Sb surface is attractive for this method of XPD: experimental data is readily available [16], and, since the surface has been studied by the multiple scattering technique of Saldin *et al.* [26], it would allow direct comparison between two very different theoretical approaches. To perform the convergence calculations, the model of the surface given by Chen *et al.* [16] is used. That is, the Sb atoms relax from  $T_4$  bonding sites to form trimers with a bond length of  $2.9\text{\AA}$ . The overlayer is taken to be  $2.7\text{\AA}$  above an unreconstructed Si(111) surface terminated with a double Si layer. The 3d core level of Sb is excited yielding photoelectrons of 738eV outside the solid. A polar take-off angle of  $6^\circ$  is used.

Calculations are shown for the  $[11\bar{2}]$  and  $[\bar{1}\bar{1}2]$  azimuths, which correspond to two symmetry directions for the surface, and are expected to be worst cases

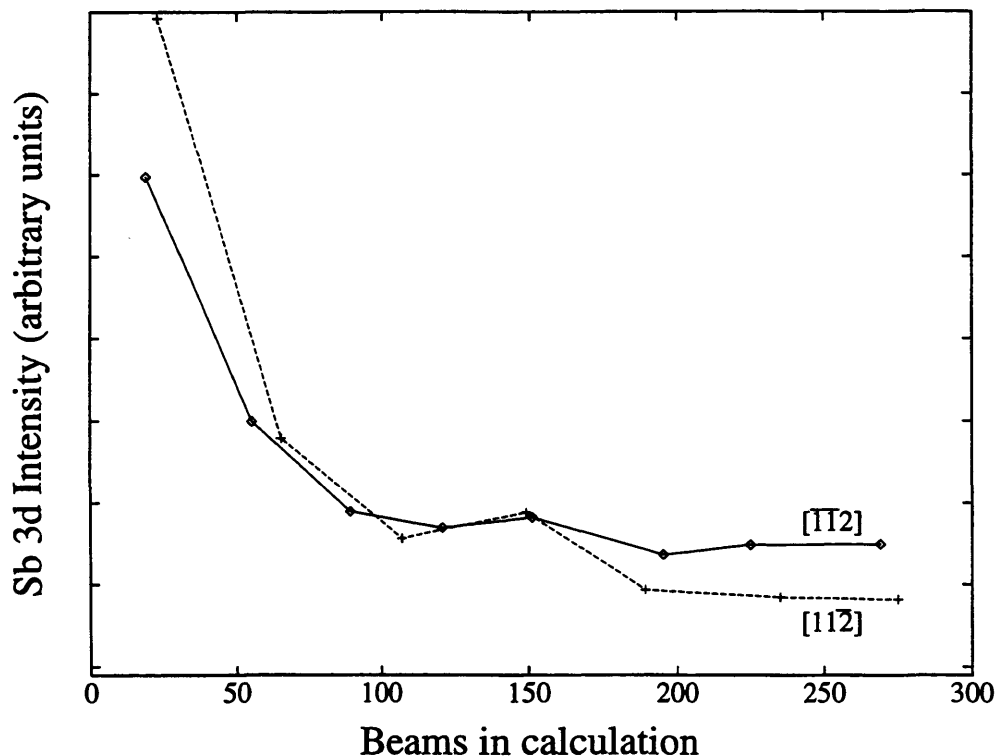


Figure 4.4: Calculated XPD intensities from the Sb 3d core level of  $(\sqrt{3} \times \sqrt{3})\text{Sb/Si}(111)$  for various different beam sets. Calculations at the two azimuths shown can be seen to converge for large beam sets. (Photoelectron energy=738eV)

for convergence. The results are shown in Fig. 4.4, as before in the form of calculated intensity against number of beams in the calculation. The calculations again converge to asymptotic values, but the number of beams required is over 200, which is significantly greater than for the O/Ni system. As a guide to the time needed to perform full calculations for this structure, a calculation involving 235 beams requires roughly 70 minutes per point on a HP735 workstation. The published data on this system, which is, as for the O/Ni system, in the form of azimuthal scans at various polar angles, and the required calculations are over a  $60^\circ$  azimuthal wedge. Therefore, a single curve sampled every 1 degree would take over 70 hours CPU time. Even if this figure was halved by sampling every

2 degrees, the CPU time would still be over double that of the O/Ni system. Performing full calculations for this system would involve producing a family of curves at different polar angles, then varying the surface parameters and repeating the calculations to find the optimum agreement with the experimental data. The amount of time to perform such a task would be too great, so it is concluded that the calculations are too large for the computing resources available.

### 4.2.3 Discussion

The XPD program has been applied to two different adsorbate systems, and it has been concluded that while calculations for the O/Ni(001) system (photoelectron energy 954eV) are quite feasible, calculations for the Sb/Si(111) system (738eV) are not. There are several reasons why the Sb/Si requires more beams to converge, the most obvious one being the low energy. The convergence criterion will naturally vary from system to system, but in general, the scale of the calculations can be expected to rise sharply as the energy is lowered below 1000eV, since the scattering becomes less focussed in the forward direction. Another factor which contributes to the beam set required is the atomic species present. For sub-monolayer adsorbate systems, the photoelectron is scattered predominantly by the atoms in the overlayer. This is especially true for the Sb/Si system, since the overlayer was 2.7Å above the outermost Si layer, and hence scattering from the substrate can be expected to be quite small. Antimony, having an atomic number of 51, represents a fairly strong scatterer, and when coupled with the energy of 738eV it is not surprising that the beam set required is so large. Oxygen on the other hand is a light atom and therefore a relatively weak scatterer, which together with the higher energy represents a more favourable system for convergence.

The motivation behind this work was to investigate the possibility of performing calculations in the higher XPD energy range ( $\approx 1000\text{eV}$  and above), where other methods suffer because they are based on a spherical wave basis. It appears that in the Sb/Si case, this method suffers a similar fate because of the low energy involved. That is not to say that the calculations are impossible: spherical wave methods have been applied to systems having keV energies, although the use of supercomputing facilities was required [61]. Certainly calculations with this method at low energies of  $\approx 700\text{eV}$  would be possible with similar facilities, but it is doubtful as to whether it is the most efficient solution. Before embarking on such a set of calculations however, attention should be paid to the accuracy of the potential. It was shown earlier in the chapter that the Doyle-Turner potential becomes less accurate at lower energies, a factor which could lead to errors in the calculations once significantly below  $1\text{keV}$ .

In summary the trial calculations show features which are expected to be true for most systems, namely full convergence at energies below  $1\text{keV}$  is difficult to achieve. This is especially true for surfaces containing atoms with high atomic number, a rough guide to scattering strength for fast moving electrons. This method for XPD calculations is therefore likely to be of greatest use in the energy range of  $1000\text{eV}$  and above, which is generally inaccessible for calculations based on the spherical wave basis.

## Chapter 5

### Application to Ni(001) $c(2 \times 2)$ S

In this chapter, the theory of XPD presented in chapters 2 and 3 will be applied to an experimental system. There are two main aims of this investigation. The first and foremost is to test the theory. The sub-monolayer adsorbate system Ni(001) $c(2 \times 2)$ S has been the subject of much experimental and theoretical work. As a result its structure is quite well understood, thereby providing an excellent test case. The second aim is to directly compare the results of this full multiple scattering analysis to a single scattering analysis of the same data.

The experimental data used is taken from the literature. High resolution XPD experiments on the system have been performed by Saiki *et al.* [18], the data being in the form of azimuthal scans at four different take-off angles ranging from 6° to 16°. The photoelectron kinetic energy is in the upper part of the XPD range at 1085eV and is therefore suitable for this theoretical approach.

The chapter is structured as follows. First, the process used to normalise a calculated curve to allow direct comparison with an experimental curve is described, followed by definitions of several R-factors for quantitative comparison between theory and experiment. Calculations are then presented for various structures, and the R-factors used to find the optimum structure. Finally, the

calculations are compared with single scattering curves published with the data.

## 5.1 Comparison of Theory with Experiment

### 5.1.1 Normalisation

Before experimental and theoretical curves can be directly compared, the theoretical curve needs to be normalised. The method adopted for this normalisation is the same as that given by Saiki *et al.* [19] whereby the theoretical curve is made to have an anisotropy (defined as  $[I_{max} - I_{min}]/I_{max}$ ) as close as possible to that of the experiment. This method of normalisation has been chosen over other, perhaps more straightforward procedures simply because it has been used in the single scattering analysis accompanying the experimental data. This allows a direct comparison with the single scattering analysis, which can be found later in the chapter.

The normalisation procedure of Saiki *et al.* is as follows. Let the raw experimental and theoretical curves over  $n$  points be denoted by  $I_{exp}(n)$  and  $I_{th}(n)$ . Finite angular resolution of the detector apparatus should already have been accounted for in the theoretical curve by the averaging procedure described in chapter 2. The first step is to scale the experimental curve so that the intensities lie between 0 and 1,

$$I'_{exp}(n) = \frac{I_{exp}(n) - I_{exp}^{min}}{I_{exp}^{max} - I_{exp}^{min}}$$

where  $I_{exp}^{max}$  and  $I_{exp}^{min}$  are the maximum and minimum values of the raw data.

Next, the average value of both the raw theoretical curve and the rescaled experimental curve are subtracted, giving the rescaled sets

$$I''_{exp}(n) = I'_{exp}(n) - \frac{1}{n} \sum_n I'_{exp}(n),$$

$$I'_{th}(n) = I_{th}(n) - \frac{1}{n} \sum_n I'_{th}(n).$$

The rescaled theoretical set  $I'_{th}(n)$  is now forced to have the same  $\pm$  area as the rescaled experimental data set  $I''_{exp}(n)$  by

$$I''_{th}(n) = I'_{th}(n) \times \left( \frac{A_{exp}}{A_{th}} \right),$$

where the areas  $A_{exp}$  and  $A_{th}$  are defined by

$$A_{exp} = \sum_n |I''_{exp}(n)|, \quad A_{th} = \sum_n |I''_{th}(n)|.$$

The final step of the normalisation is to put the theoretical data set  $I''_{th}(n)$  onto the same scale as the original experimental curve. This is done by adding the average of the  $I'_{exp}$  set which was subtracted, and reversing the process which scaled the original experimental set to be between 0 and 1. The normalised theoretical data set,  $I_{th}^N(n)$ , is therefore given by

$$I_{th}^N(n) = \left( I''_{th}(n) + \frac{1}{n} \sum_n I'_{exp}(n) + \frac{I_{exp}^{min}}{I_{exp}^{max} - I_{exp}^{min}} \right) \times (I_{exp}^{max} - I_{exp}^{min}),$$

and can now be directly compared with the raw experimental data  $I_{exp}(n)$ .

### 5.1.2 Reliability Factors

A reliability factor (R-factor) is a formula or prescription which puts a numerical value on the degree of disagreement between two curves, usually a comparison between theoretical and experimental curves. The procedure to determine the best agreement with experimental data is to systematically vary structural parameters in order to find a global minimum in the R-factor, and is a standard method for analysing LEED data [65].

Van Hove *et al.* [72] have defined five R-factors for the analysis of LEED I-V curves with theory, designed to be sensitive to different features of the curves.

These are

$$R1 = \sum_n |I_n^{exp} - I_n^{th}| / \sum_n |I_n^{exp}|$$

$$R2 = \sum_n |I_n^{exp} - I_n^{th}|^2 / \sum_n |I_n^{exp}|^2$$

$R3$  = fraction of energy range with slopes of different sign

$$R4 = \sum_n |I_n'^{exp} - I_n'^{th}| / \sum_n |I_n'^{exp}|$$

$$R5 = \sum_n |I_n'^{exp} - I_n'^{th}|^2 / \sum_n |I_n'^{exp}|^2.$$

In these formulae,  $I'$  denotes the first derivative of an intensity with respect to energy. The set  $R1$ - $R5$  provides sensitivity to all of the features which are considered to be important in an experiment-theory comparison of LEED I-V curves.  $R1$  and  $R2$  tend to emphasise the agreement in the positions, height and width of peaks and troughs.  $R3$ - $R5$ , which involve the gradients of the curves, were introduced to account for the insensitivity of  $R1$  and  $R2$  to other features of the I-V curves such as bumps and shoulders within a single peak, and the actual shape of the peaks.

The R-factors  $R1$ - $R5$  have been used to compare theoretical XPD curves with experiment [18, 19], with the quantities  $I'$  denoting the first derivative of an intensity with respect to azimuthal angle rather than energy. The merits of the individual R-factors when applied to XPD are discussed later in the chapter.

## 5.2 Ni(001) $c(2 \times 2)$ S

The XPD calculation described in chapters 2 and 3 will be applied to an experimental system in this section. The system chosen is the Ni(001) $c(2 \times 2)$ S overlayer system, essentially for two reasons. The first is that there is a general agreement on the structure, which provides a good test system for the theory,

and the second is that there is an excellent set of high resolution XPD data, at a suitable energy for this approach, available in the literature.

Sulphur adsorbed onto clean nickel surfaces is of particular technological interest: it is well known that the presence of small amounts of S can poison certain catalytic reactions over Ni and other transition metal catalysts. The methanation reaction  $\text{CO} + 3\text{H}_2 \rightarrow \text{CH}_4 + \text{H}_2\text{O}$  over a Ni(001) surface is a dramatic example of S poisoning. The presence of only  $\approx 0.2\text{ML}$  of S on the Ni catalyst can result in rate of methane production being slowed by an order of magnitude. The interest in the S-Ni system has therefore led to many studies of the geometry of the  $c(2 \times 2)\text{S}$  and  $p(2 \times 2)\text{S}$  surfaces. The  $c(2 \times 2)$  surface is regarded as one of the better understood adsorption systems in the field of surface science, and as such it is often used as test system. Indeed much contemporary work on various inversion schemes in high energy photoelectron holography use the Ni(001) $c(2 \times 2)\text{S}$  surface as such a test system [18].

Numerous techniques have been used to study the system, including LEED [64, 65, 66], photoelectron diffraction [67], STM [68] and surface extended X-ray absorption fine structure [69]. The general consensus is that the  $c(2 \times 2)\text{S}$  surface is formed with the sulphur atoms bonded in fourfold hollow sites, at a vertical height of between about 1.30 and 1.40 Å above the top Ni layer. There is evidence for a slight increase in the spacing of the outer Ni layers compared with the bulk value [18, 66], and the LEED analysis by Oed *et al.* [66] reports some buckling in the second layer of Ni.

### 5.2.1 An Experimental XPD Study

The XPD study of the system by Saiki *et al.* [18] will be briefly described in this section. The experiment was performed using a high angular resolution electron analyser of  $\pm 1.5^\circ$ , the aim being to assess whether high angular resolution data would allow more information about the bonding site to be determined when the adsorption height is relatively high (roughly  $>1.0\text{\AA}$ ).

The problem of using XPD with such systems is illustrated in Fig. 5.1. A photoelectron emitted from a S atom in the overlayer must be scattered through a large angle by the Ni substrate in order to be detected due to the large adsorbate-substrate registry, and this contribution to the full signal is therefore much weaker than the scattering from within the overlayer. An earlier XPD study on the same system has shown this to be the case. To extract information about the adsorption height and the first to second layer Ni spacing ( $z$  and  $d_{12}$  respectively in Fig. 5.1), the experiment must be able to detect small changes in the diffraction signal caused by scattering from the Ni substrate. It is very difficult to resolve such detail using a standard electron analyser, which typically has resolution of the order  $\pm 3^\circ$ , and so the experiment was conducted using the high angular resolution analyser. The use of such a high angular resolution analyser had been previously shown to increase dramatically the amount of fine structure in the diffraction signal [71].

The XPD experiment was conducted with an experimental arrangement as shown in Fig. 2.1. Unpolarised Mg  $K\alpha$  radiation ( $h\nu=1253.6\text{eV}$ ) was used to excite the S  $2p$  core level, yielding photoelectrons with an energy of  $1085\text{eV}$ . For any adsorbate XPD experiment, the forward nature of the scattering means to attain information regarding the substrate, it is necessary to collect the

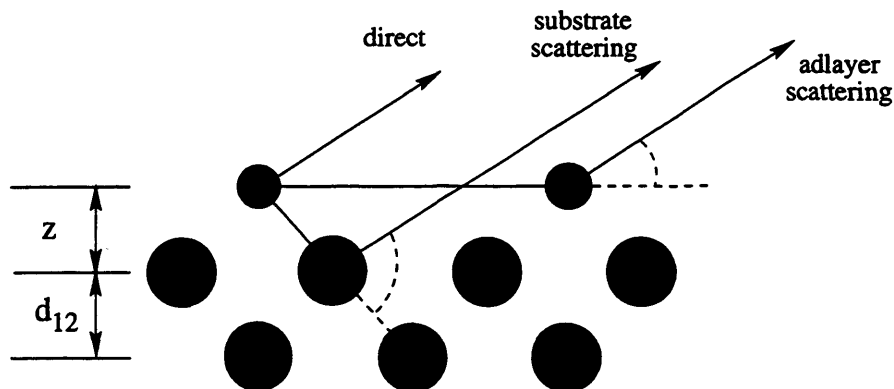


Figure 5.1: Schematic diagram showing adsorbates well above the substrate. The angles involved with scattering from the substrate can be seen to be much greater than for scattering within the adlayer. The substrate signal is therefore much weaker.

photoelectrons at fairly low take-off angles, less than about 20-25°. This is especially true for the present system: as the S atoms lie well above the top Ni layer, grazing take-off angles are required to reduce the angles involved with scattering from the Ni as much as possible. Azimuthal angular-scans were performed at at four different take-off angles, 6°, 10°, 12° and 16°. The angle between X-ray incidence and electron exit was fixed at 48° and data was taken over a 100° azimuthal range encompassing the [100] and [010] azimuths, before being mirror averaged across the [110] symmetry azimuth to improve reliability. Both the raw and mirror averaged data are presented in the paper, the raw data being in very good agreement with the averaged data, indicating a good quality data set.

### 5.3 Calculations

Calculations have been performed for many trial surface structures to find the optimum agreement with the data, allowing the overlayer height and to a lesser

extent the top Ni-Ni spacing and adsorption site to be varied. Thorough convergence tests have been carried out for the Ni(001)  $c(2 \times 2)$ S surface, and show that the calculations require approximately 150 beams, which is quite manageable on a HP735 computer. This is to be expected as S is not a particularly heavy atom and the photoelectron energy at 1085eV is relatively high. The calculations are therefore on roughly the same scale as the Ni(001)  $c(2 \times 2)$ O system, for which convergence tests were demonstrated in chapter 4, which gives a guide as to the CPU time required.

### 5.3.1 Non-Structural Parameters

The non-structural parameters in the calculation are associated with corrections to the Doyle-Turner potential [48]. The volume-average potential can be defined as the average with respect to the  $z$  co-ordinate of the zeroth Fourier component of the potential. This usually needs to be adjusted for RHEED calculations as it does not correctly reproduce Bragg peaks in experimental rocking curves. The RHEED program accounts for this by adding a constant correction term to the zeroth Fourier component of the potential, and the correction allowed to approach zero at the surface as a Gaussian. Such a procedure changes the wavelength of the electrons in the solid, and hence the Bragg condition. In RHEED calculations, the size of the correction (typically  $\pm$ few eV) is determined by aligning calculated peak positions with experiment. For the XPD calculation, the correction to the volume-average potential can be treated as an adjustable parameter to improve the fit between experimental and theoretical curves.

To account for absorption, an imaginary part is added to the potential, taken to be proportional to the real part. This has been discussed in more detail in

chapter 3. The constant of proportionality can be expected to depend on the energy of the electrons, reflecting the inelastic mean free path. This constant is taken to be around 0.1 for calculations at RHEED energies, but can be treated as an adjustable parameter to improve agreement with data. Thermal motion of the atoms is accounted for by Debye-Waller factors, also discussed in chapter 3.

Trial calculations for the present system have shown that the overall agreement with experiment is improved with a constant correction to the volume-average potential of  $-3\text{eV}$ . Significant improvements in the fits were not observed by increasing the size of the imaginary potential, so the calculations were performed with the constant of proportionality set at 0.1. Bulk Debye-Waller factors from the literature [54] were used for both bulk and surface atomic layers. Strictly, the surface layers should incorporate different Debye-Waller factors than the bulk, but trial calculations performed with larger Debye-Waller factors for the surface yielded results almost indistinguishable from those using bulk factors.

### 5.3.2 Adsorption Height

The first set of calculations are to determine the optimum adsorption height with no relaxations in the bulk layers. Previous studies of this system have indicated that the most likely adsorption site is the fourfold hollow, so the S atoms in these calculations have been fixed in such sites. Calculations using the non-structural parameters described above have been performed for all four polar angles,  $\theta = 6^\circ, 10^\circ, 12^\circ$  and  $16^\circ$ . For each take-off angle, the overlayer height has been varied from  $z=1.20\text{\AA}$  to  $z=1.50\text{\AA}$  in steps of  $0.05\text{\AA}$ , encompassing the  $1.30\text{-}1.40\text{\AA}$  range which previous studies have shown to be the most likely height.

Figs. 5.2 - 5.5 show for each take-off angle some calculated curves with overlayer

height varied in steps of  $0.1\text{\AA}$ , along with the experimental curves taken from [18]. A first remark about the calculations, which applies to all four take-off angles is that even though the calculated curves are separated by quite large steps of  $0.1\text{\AA}$ , only subtle changes are observed. This is due to the weak sensitivity of XPD to the substrate for relatively high adsorbates, as discussed earlier, and displays very clearly the need for high resolution experimental work in order to study such systems.

The lowest take-off angle of  $\theta = 6^\circ$  (Fig. 5.2) contains by far the most fine structure of the four, due to the stronger scattered signal at grazing take-off angles. All four calculated curves are very similar despite the low take-off angle. Much of the fine structure has been predicted, especially between  $30 - 60^\circ$  for  $z=1.30\text{\AA}$  and  $z=1.40\text{\AA}$ , where agreement is very good. The features in the  $0 - 20^\circ$  range can be clearly identified in the theoretical curves, although the relative intensities are not in full agreement. None of the calculations correctly predict the doublet observed experimentally between  $20 - 30^\circ$ , all predicting a single peak across this angular range.

The calculations at  $\theta = 10^\circ$  (Fig. 5.3) show more variations with adsorption height  $z$ . All of the features of the experimental curve are correctly reproduced by the curves, and are in the correct positions. As the adsorption height is varied, it is the relative heights of the features rather than their position which change. The peak at approximately  $27^\circ$  can be seen to increase with  $z$  and the depth of the trough at  $45^\circ$  becomes less pronounced. When the height has reached  $z=1.50\text{\AA}$ , the theoretical curve can clearly be seen to be an inferior match to the data than the other three.

Excellent agreement can be seen for the curves calculated at  $z=1.20\text{\AA}$  and

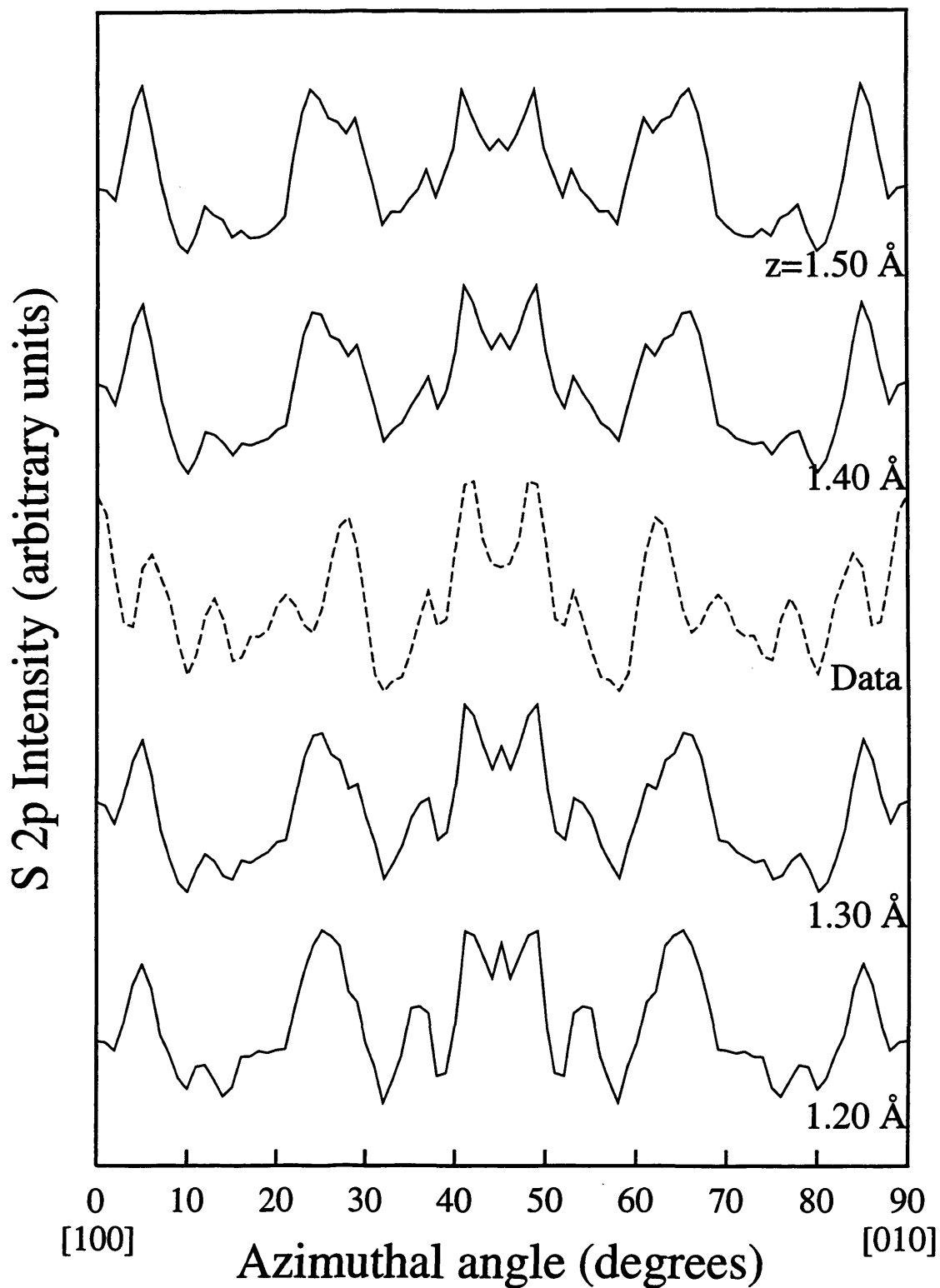


Figure 5.2: Theoretical XPD curves (solid lines) for different adsorption heights of the  $c(2 \times 2)S$  overlayer on a bulk terminated Ni(001) substrate at take-off angle  $\theta = 6^\circ$ . Experimental data is from ref. [18].

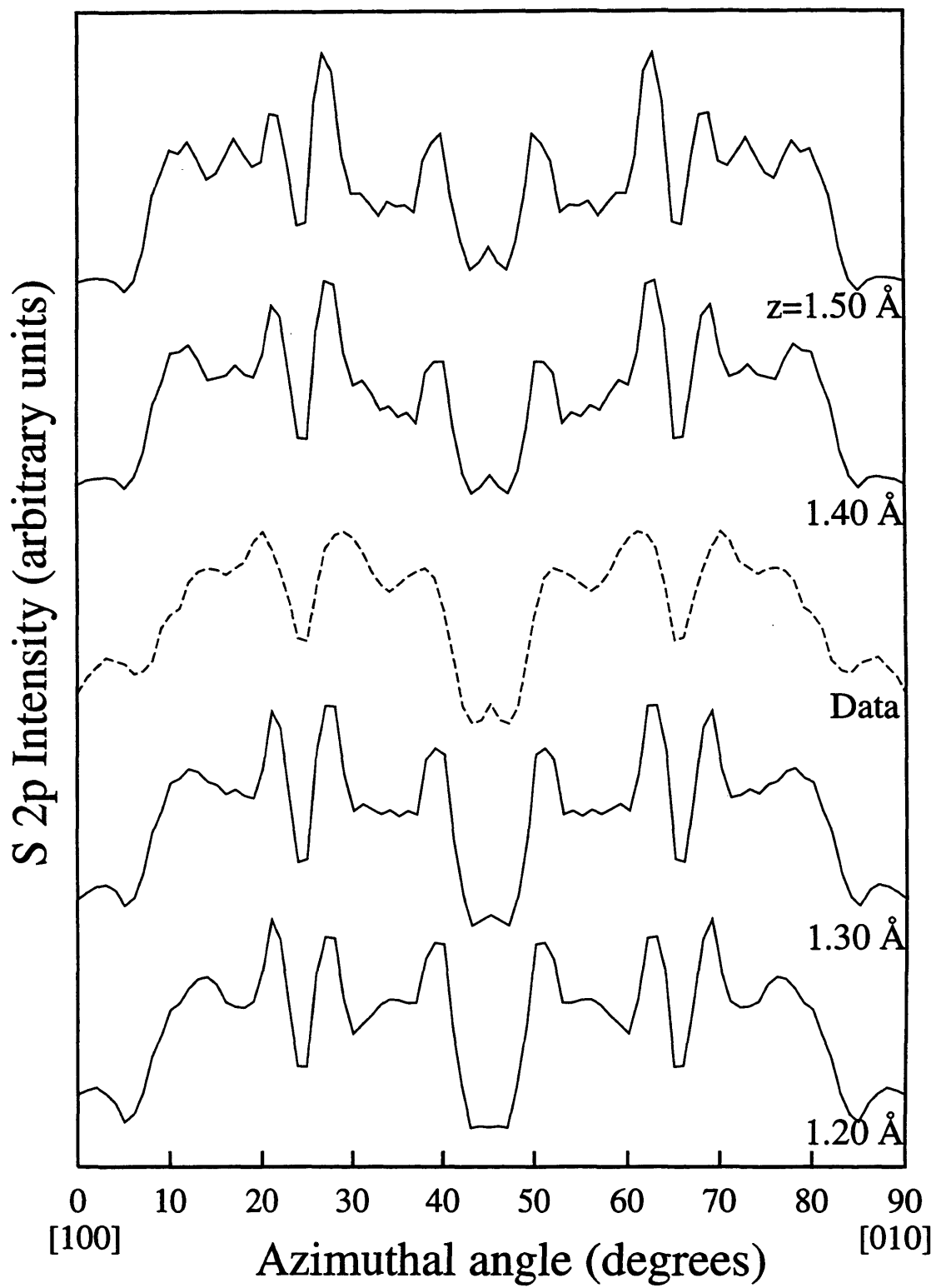


Figure 5.3: Same as Fig. 5.2 but for take-off angle  $\theta = 10^\circ$ .

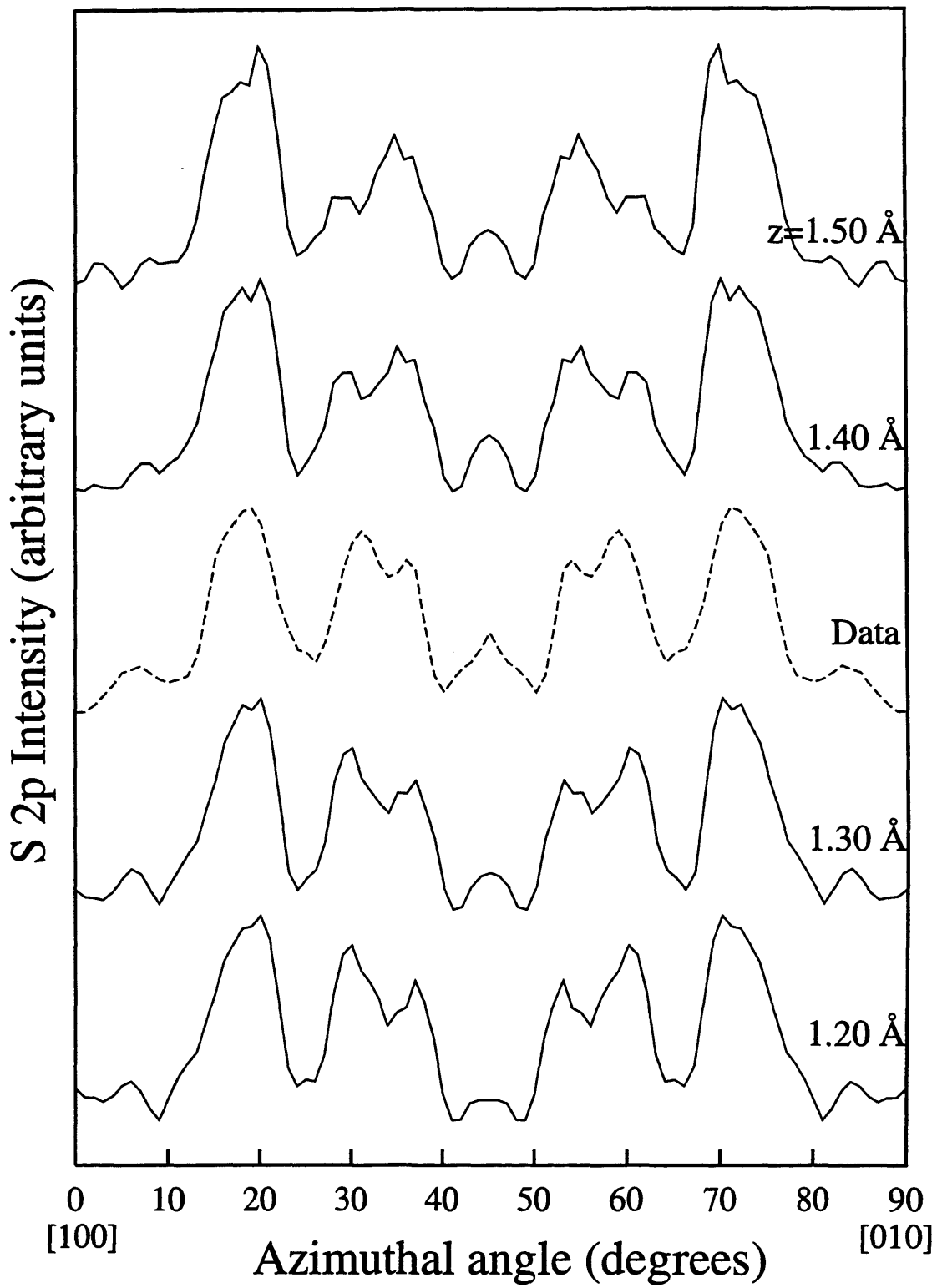


Figure 5.4: Same as Fig. 5.2 but for take-off angle  $\theta = 12^\circ$ .

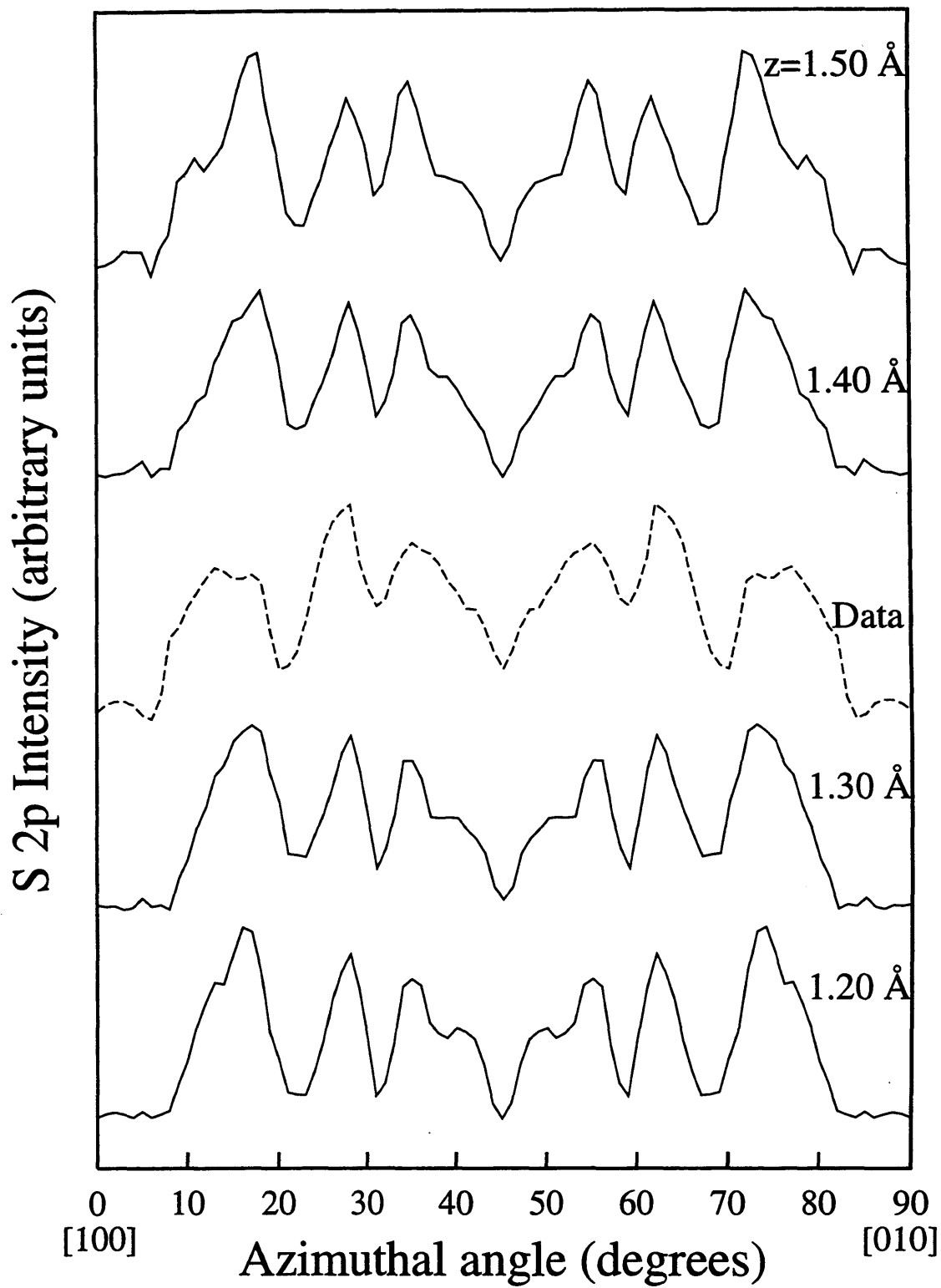


Figure 5.5: Same as Fig. 5.2 but for take-off angle  $\theta = 16^\circ$ .

$z=1.30\text{\AA}$  at  $\theta = 12^\circ$  (Fig. 5.4). All the features observed experimentally have been correctly predicted by these two curves, although the doublet centred at approximately  $32^\circ$  is predicted to be slightly wider than that in the data. The calculations performed at  $z=1.40\text{\AA}$  and  $z=1.50\text{\AA}$  are visibly poorer fits to the data, the main discrepancy coming in the heights of the aforementioned doublet.

It has been noticed that the previous calculations have displayed only small variations with adsorption height, and this is especially true for the calculations at  $\theta = 16^\circ$  (Fig. 5.5). All the calculated curves are seen to be remarkably similar. This is due to the larger scattering angles involved with a take-off angle of  $16^\circ$  weakening even more the sensitivity to the substrate position. All four theoretical curves are in good general agreement with the data, even though this particular take-off angle is potentially the most difficult to attain good agreement. Experimental data is usually less reliable at higher take-off angles: the anisotropy is usually much smaller due to the weak scattered signal, meaning experimental noise plays a greater role.

The R1 - R5 of Van Hove *et al.*, as defined earlier in the chapter have been calculated using the curves shown in Figs. 5.2-5.5, and the calculations at intermediate bonding heights not shown. The resulting R-factors are shown in Fig. 5.6, where they have been moved to be on the same vertical scale for clarity. Calculations at all four polar angles have contributed to the curves in Fig. 5.6. Individual R-factors were calculated for each polar angle and then averaged to give a point on the curve.

Factors R1 - R4 all display clear minima in their curves. Perhaps the least convincing of the four is R3, which is the percentage of points where the theoretical and experimental gradients do not agree in sign. As such, R3 is

sensitive to the additional fine structure which is displayed in the theoretical curves. For example, consider the set of curves calculated at  $\theta = 10^\circ$  in Fig. 5.3. The calculated curve at  $1.30\text{\AA}$  displays fine structure between the peaks at approximately  $27^\circ$  and  $39^\circ$ , where although the magnitude of the structure is small, the gradient changes sign many times. This structure is not present in the experimental curve, the gradient changing sign just once in the corresponding angular range. The result is a poor R3 for the calculated curve, despite being a visibly good fit to the data. This could also prove to be a problem with R4 and R5. The theoretical curves will naturally predict fine structure that cannot be resolved experimentally despite the steps taken to simulate finite angular resolution. Any resulting gradient discrepancies could lead to misleadingly poor values of R4 and R5. Nonetheless it is encouraging that all R1 - R5 in Fig. 5.6 show steep increases at adsorption heights greater than  $1.35\text{\AA}$ , and only R5 does not show an increase at adsorption heights less than  $1.30\text{\AA}$ . The minima of the curves in Fig. 5.6 indicate that an overlayer height of  $1.30\text{\AA}$ - $1.35\text{\AA}$  gives best agreement with the data.

For most XPD analyses of this type, the R-factors used tend to take the form of R1 or R2 [18, 26, 16], using the absolute difference between the experimental and normalised theoretical data points rather than the gradients of the curves. Saiki *et al.* [19] have found that structural conclusions based on R1 are in good agreement with conclusions based on the other R-factors. For the remainder of the comparisons between theory and experiment, R1 will be used. This has the obvious advantage that R1 concentrates on the positions and relative sizes of the features in two curves rather than the fine structure, removing the worry about enhanced fine structure in the theoretical curves giving poor values of R3 -

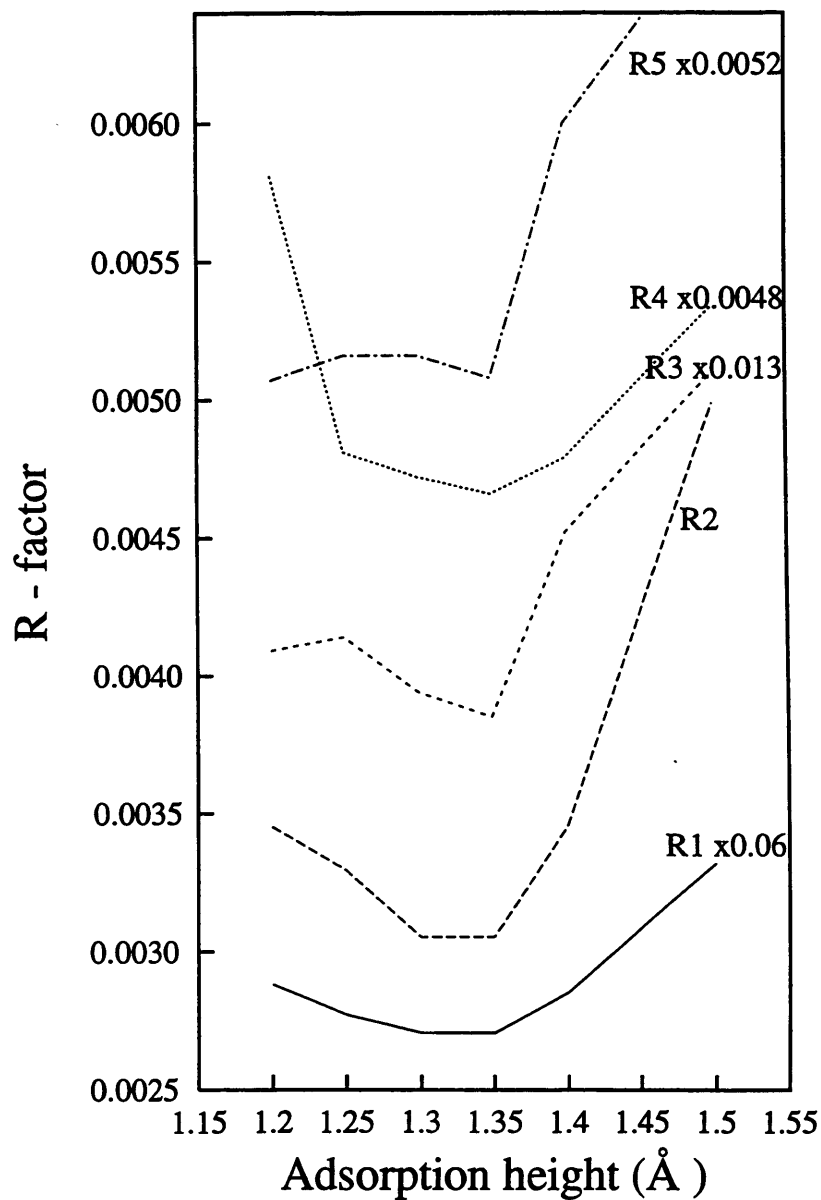


Figure 5.6: Reliability factors R1 - R5 for calculations on Ni(001)c(2×2)S. Points on each curve are the average R-factor for the four take-off angles. The curves indicate that the an overlayer height of 1.30Å-1.35Å gives best agreement with the data. Note the multiplying factors which have been used to display all five curves on the same range as R2

R5. Another advantage is that the calculations accompanying the XPD data in ref. [18] have been analysed using R1, allowing some form of comparison with the present calculations.

### 5.3.3 Adsorption Site

The previous calculations assumed the S atoms occupied fourfold hollow sites and the most favourable adsorption height determined to be 1.30Å-1.35Å. The S atoms are now fixed at this height (1.35Å), and the S atoms moved in-plane. As it is generally agreed that the S atoms are bonded in the hollow site, a full set of calculations has not been performed. To demonstrate that the calculations are sensitive to lateral displacements of the S atoms, calculations have been performed for two alternative sites, the on top and the bridge. All three sites are schematically illustrated in Fig. 5.7. The calculated curves are shown in Fig. 5.8, where all three are for a take-off angle of 10°.

The experimental curve has been shown with each calculated curve for direct comparison, and the R1 factor shown to quantitatively indicate the degree of agreement between theory and experiment. It is clear by a simple visual comparison that the hollow site does indeed give the best agreement of the three with the experimental data. This is supported by the significantly lower R1 for this site of 0.043 compared with 0.056 (bridge) and 0.058 (top). The top site calculation shows poor agreement with the experimental curve in the 30-60° range, and the bridge site displays many smaller discrepancies over the whole angular range. The general shapes of all three calculated curves can be seen to be quite similar. This indicates a large contribution to the signal by scattering within the overlayer, a feature which has been described earlier. The scattering

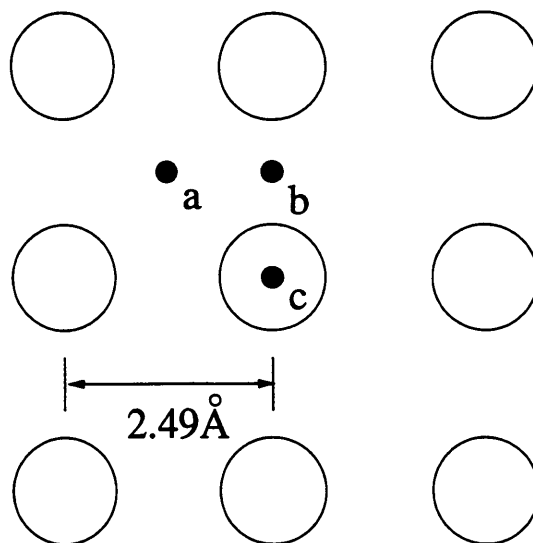


Figure 5.7: The three different bonding sites for which calculations have been performed. Large circles represent the top layer of Ni(001). Position (a) is the hollow site, (b) the bridge site and (c) the on top site.

from the substrate however is still an important factor which clearly affects the results of the calculations, even at such high adsorption heights.

#### 5.3.4 Substrate Relaxation

All of the calculations shown so far have been performed with no relaxations in the underlying nickel layers. Previous studies on the system have reported an increase in the outer Ni-Ni layer spacing [66, 18]. To investigate this, a further set of calculations have been performed with the outer Ni-Ni layer spacing ( $d_{12}$ ) increased from 1.76 Å to 1.86 Å, an expansion of 5.7%, with the S atoms occupying the preferred hollow sites. The earlier calculations at the higher polar angles of  $\theta = 12^\circ$  and  $\theta = 16^\circ$  were less sensitive to variations in the overlayer height than those at  $\theta = 6^\circ$  and  $\theta = 10^\circ$ , they are expected to be even less sensitive to variations in  $d_{12}$ . Therefore to save computer time, calculations with the relaxed

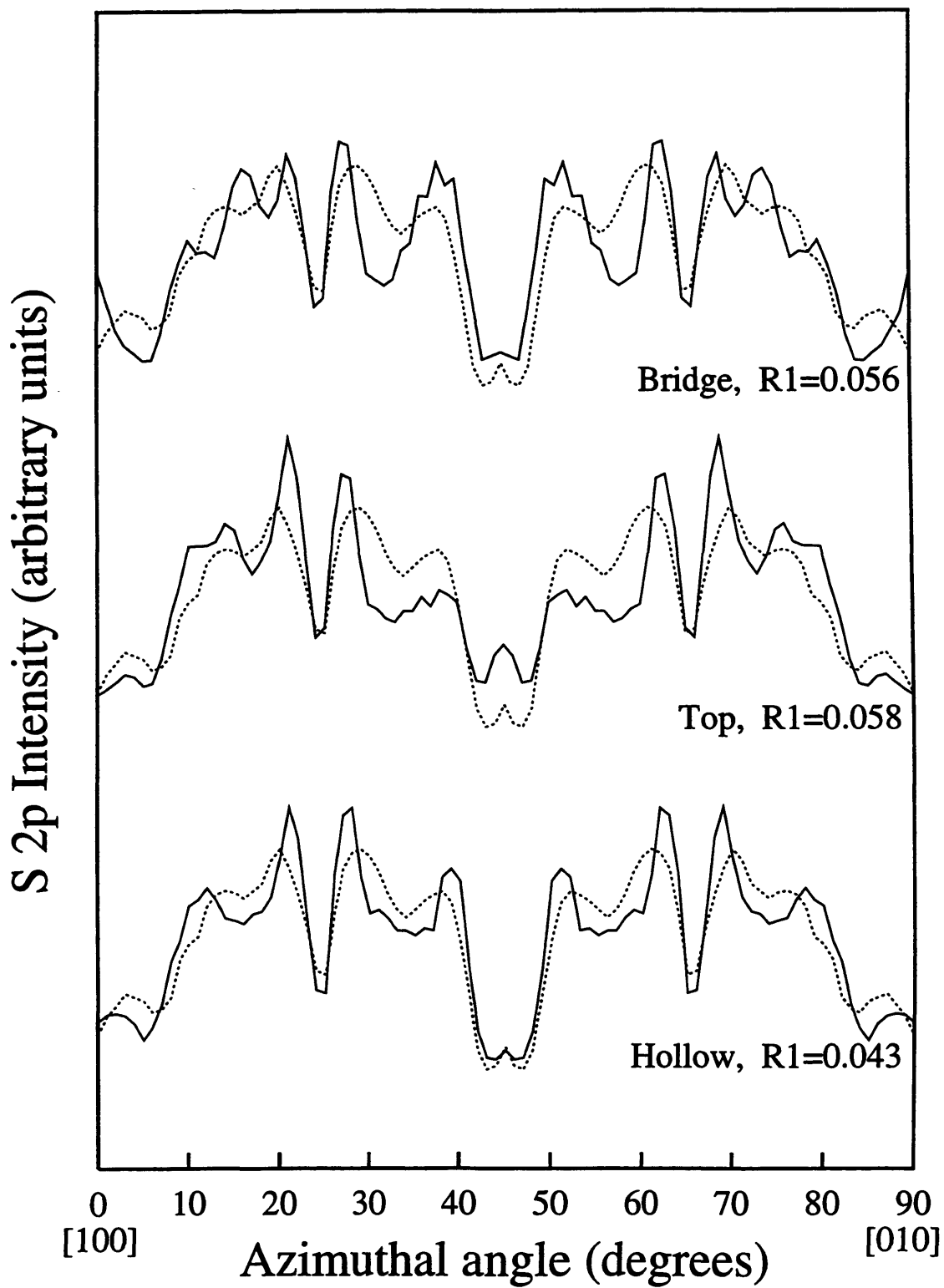


Figure 5.8: Results of a calculation at a fixed adsorption height of  $1.35\text{\AA}$ , for three different adsorption sites. The solid lines are calculated curves, the dotted lines the same set of experimental data. The values of  $R1$  are shown for each site as an indication of the agreement.

substrate have been performed for  $\theta = 6^\circ$  and  $\theta = 10^\circ$  only. The same procedure as before has been followed, that is to repeat the calculation varying the height of the S overlayer. The summed R1 for these calculations is presented in Fig. 5.9, along with the R1 for the unrelaxed substrate using only the  $\theta = 6^\circ$  and  $\theta = 10^\circ$  calculations. A first remark is regarding the R1 calculated for the unrelaxed substrate. When all four take-off angles are considered, from Fig. 5.6 it can be seen that the same minimum R1 occurs at both  $z=1.30\text{\AA}$  and  $z=1.35\text{\AA}$ . When R1 is calculated using just the lowest two take-off angles, the  $z=1.30\text{\AA}$  height is clearly favoured over  $z=1.35\text{\AA}$ . This indicates that the calculations at  $\theta = 12^\circ$  and  $\theta = 16^\circ$  have an effect on the R1 analysis despite being less sensitive the overlayer height.

From Fig. 5.9 it can be seen that the outward relaxation in  $d_{12}$  the minimum R1 is lowered from 0.0428 to 0.0413. This is only a small difference, but it is comparable to changes observed by moving the overlayer height. The minimum in R1 remains at  $1.30\text{\AA}$  when the substrate relaxation is included, but the general shape of the curve appears to have shifted to a slightly lower adsorption height, as the R1 obtained at  $z=1.25\text{\AA}$  is only a little higher than that at  $1.30\text{\AA}$  and there is a sharper increase between  $z=1.30\text{\AA}$  and  $z=1.35\text{\AA}$ .

In summary, a full set of calculations for allowing the S overlayer to vary and keeping the Ni substrate unrelaxed gives an optimum height of  $z=1.30\text{\AA}$ - $1.35\text{\AA}$ . Further calculations for  $\theta = 10^\circ$  supported the hollow bonding site above the on top and bridge geometries, both of which had much larger values of R1. The fact that R1 can be decreased by moving the top Ni-Ni spacing outwards by  $0.1\text{\AA}$  provides evidence that there is some relaxation, but it is difficult to be fully quantitative as calculations were only performed for this one value. The most

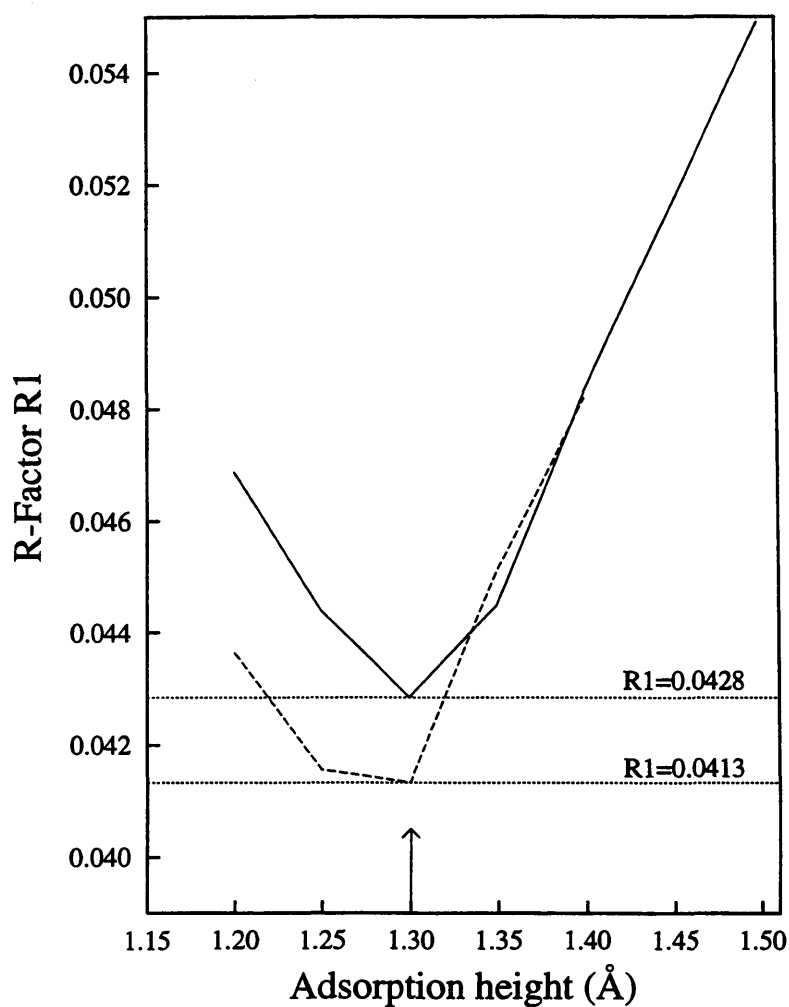


Figure 5.9: Summed R1 factors using calculations at  $\theta = 6^\circ$  and  $\theta = 10^\circ$ , for various adsorption heights. The solid line is with  $d_{12}$  having the bulk spacing of  $1.76 \text{ \AA}$  and the broken line is with  $d_{12}$  relaxed to  $1.86 \text{ \AA}$ . The arrow at  $1.30 \text{ \AA}$  indicates the minimum of both curves.

favourable adsorption height when the relaxation is included remains the same as for the unrelaxed substrate at  $z=1.30\text{\AA}$ , although the general shape of the R1 curve appears to shift to favour slightly a lower adsorption height. Again, it is difficult to be fully quantitative as only the two lowest take-off angles were used to perform this analysis, and from calculations on the unrelaxed substrate, it seems that including the higher angles may affect these results. Overall, the results are in very good agreement with other studies of the system, and provides evidence of the applicability of this new scheme for XPD calculations.

### 5.3.5 Comparison with Single Scattering Theory

In this section the multiple scattering (MS) calculations which have been performed in this chapter are compared with the single scattering (SS) analysis of Saiki *et al.* [18]. Accurate spherical wave treatments of XPD require large amounts of CPU time, and so some SS approaches have either used plane wave scattering or assumed *s*-emission. In the second approximation, instead of the initial photoelectron (angular momentum quantum number  $l_i$ ) being emitted into final interfering  $l_i + 1$  and  $l_i - 1$  channels, it is assumed that  $l_i = 0$  (*s*-state) and final angular momentum  $l_f = 1$  (*p*-state). The SS approach employed by Saiki is therefore a relatively sophisticated calculation as it includes full spherical wave scattering and the correct  $p \rightarrow$  interfering  $s + d$  final states involved with  $2p$  photoemission.

The MS calculations in this chapter for the lowest two take-off angles gave the lowest value of R1 at  $1.30\text{\AA}(\pm 0.05\text{\AA})$  for S bonded in fourfold hollow sites. There was some evidence for a small outward relaxation ( $0.1\text{\AA}$ ) in  $d_{12}$ , although only this one relaxation was tried. The SS analysis of the same data resulted in an

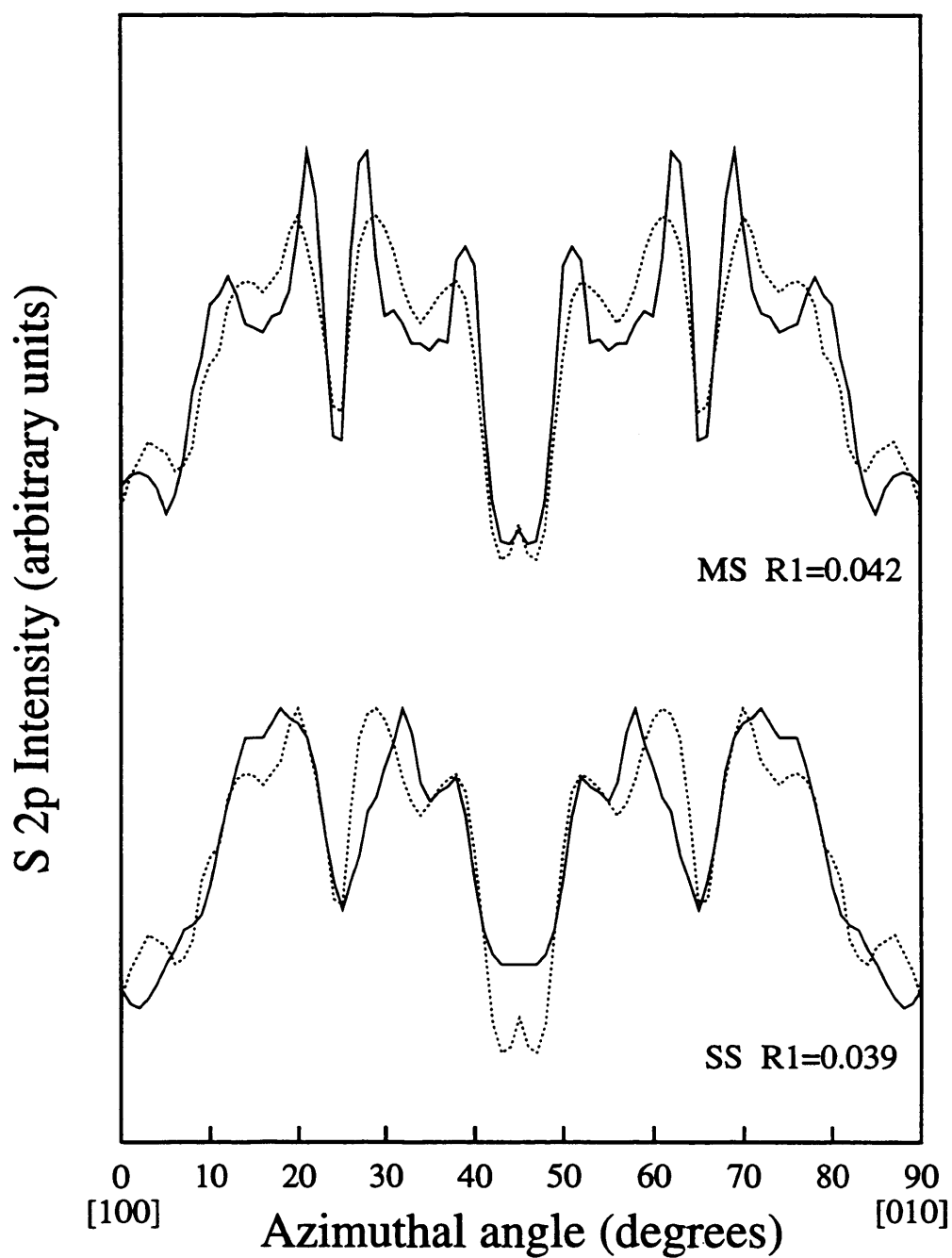


Figure 5.10: The best fit single scattering (SS) calculation of Saiki, and the best fit multiple scattering (MS) calculation using the present method at take-off angle  $\theta = 10^\circ$ . Solid lines are the calculated curves, the dotted lines the same set of experimental data.

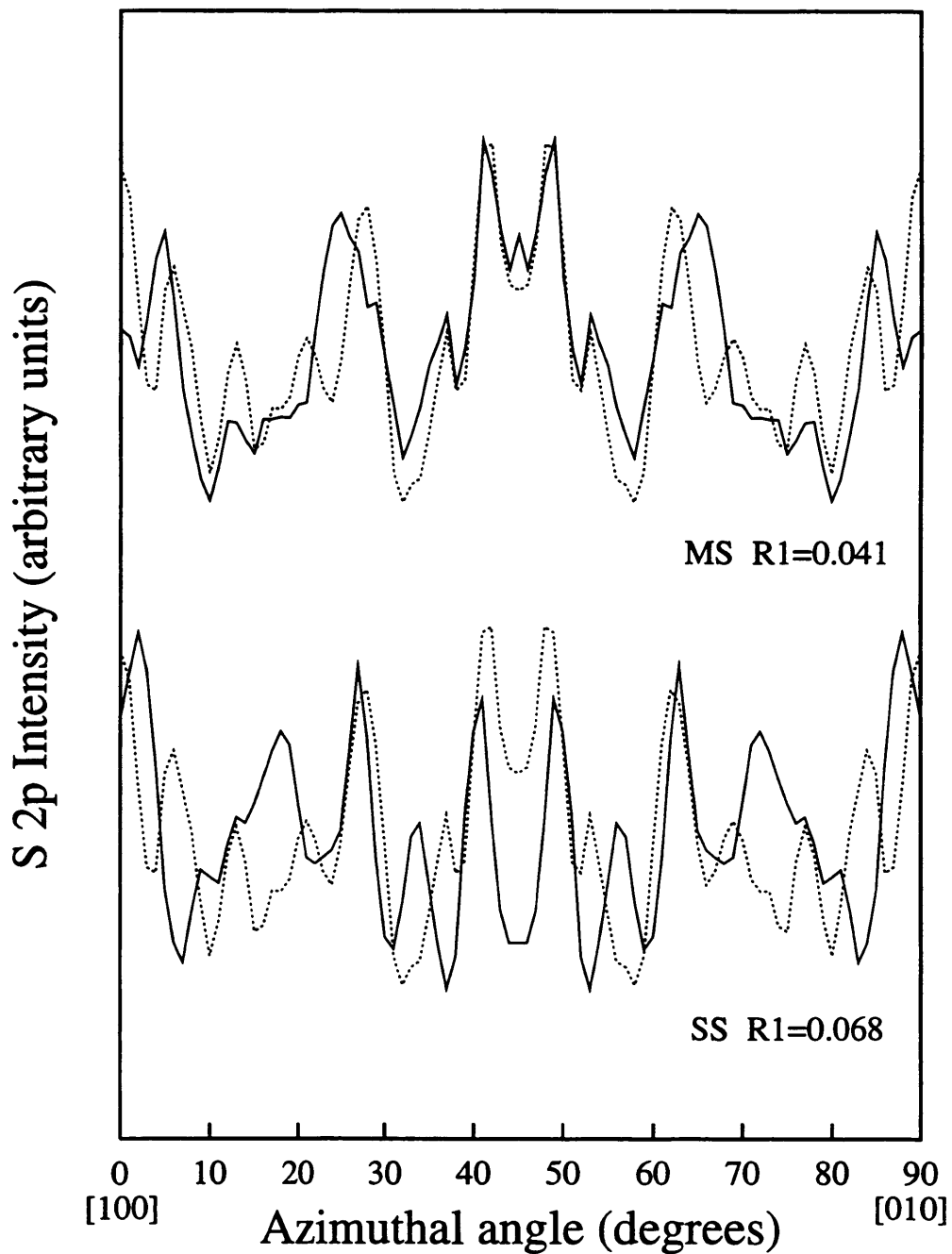


Figure 5.11: The best fit single scattering (SS) calculation of Saiki, and the best fit multiple scattering (MS) calculation using the present method at take-off angle  $\theta = 6^\circ$ . Solid lines are the calculated curves, the dotted lines the same set of experimental data. The MS calculation can be seen to be a far superior fit to the data than the SS calculation, resulting a significantly lower value of R1.

optimum structure which has the S overlayer bonded in the same geometry at  $1.39\text{\AA}(\pm 0.05\text{\AA})$  above the Ni substrate. Again there was evidence for relaxation in  $d_{12}$ . This SS analysis used only the highest two take-off angles to arrive at the optimum  $d_{12}$  spacing, as no minimum was found in the  $\theta = 6^\circ$  and  $\theta = 10^\circ$  R1 curves. Intuitively one would expect the lowest take-off angles to provide more sensitivity to this parameter, and a possible reason given for the null R1 analysis was that multiple scattering was important. It is possible to assess this by direct comparison between the present MS calculations at the low take-off angles and the SS curves published in ref. [18].

The same normalisation procedure and R-factor analysis as Saiki *et al.* has been used to allow this comparison between calculations. Fig. 5.10 shows comparison with the experimental data for the best fit SS and MS calculations. Both can be seen to reproduce the experimental data very well, in fact the SS calculation displays a slightly value of R1, 0.039 compared with 0.042 for the MS calculation. The MS calculation displays far more structure than both the SS calculation and the data, and suggests broader angular averaging could reduce the MS value of R1. It is not really possible from these curves to conclude that SS is not adequate to model the data.

The very lowest take-off angle shows conclusively the failure of SS theory. Fig. 5.11 shows the SS and MS for  $\theta = 6^\circ$ . It is quite clear that the MS approach is a far superior calculation: almost all of the fine structure is reproduced with the relative intensities in good agreement with the data. The only major discrepancy is the failure to predict the doublet centred around  $25^\circ$ , and its symmetry related counterpart around  $65^\circ$ , a single broad peak being predicted instead. The SS calculation is poor at predicting both peak positions and peak intensities, which

is reflected in its R1 factor of 0.068 compared to the MS value of 0.041.

In summary then, it has been shown that, at least at the lowest take-off angle (Fig. 5.11), the experimental data cannot be reproduced with a SS theory, even with the refinements described above. This suggests the presence of multiple scattering events caused by the photoelectron travelling almost parallel to the surface. The MS calculations using the present method reproduce the experimental data far better than the SS calculations, and therefore represents a more reliable means of analysing such data. Even at higher take-off angles (Fig. 5.10), although good agreement between SS and experiment may be obtained, it is no guarantee that MS effects are not present. As all orders of scattering are not included in SS calculations, it may be that the best agreement with the data is found using incorrect structural parameters. The validity of SS calculations can only be completely verified by obtaining the same structural parameters from more accurate MS calculations.

## Chapter 6

# A Study of Ni(001) $c(2 \times 2)$ O

### 6.1 Introduction

The interaction of oxygen with clean nickel surfaces has been studied in depth over recent years. Such studies include adsorption geometries [13,17,19,78-83], the kinetics of the interaction [73, 74], and of the electronic structure [75, 76]. A comprehensive review of the interaction of oxygen with nickel surfaces can be found in ref. [77]. This chapter is concerned with the  $c(2 \times 2)$ O adsorption system on the (001) surface of nickel. This system in itself has been the subject of many studies in the literature, largely due to the uncertainty as to its structure, as many, often conflicting models have been proposed for location of the O atoms.

As will be discussed in the next section, it is difficult to form an ideal  $c(2 \times 2)$ O overlayer structure on Ni due to the relative ease of oxygen to diffuse into the bulk, and the early onset of oxide formation. This poses a problem, as a particular technique may be sensitive to sub-surface O and lead to results different to those from an ideal overlayer, possibly resulting in incorrect structural conclusions being drawn from the data. XPD studies of the  $c(2 \times 2)$  surface utilising O emission are clearly affected by the presence of buried oxygen contributing to the observed

signal. The approach taken to reduce the signal from sub-surface emitters is to take measurements at grazing angles of emission. This increases the probability of inelastic scattering for sub-surface emitters due to the increased distance required for a photoelectron to travel in the solid before it escapes. The observed signal then largely originates from the overlayer. It was shown in chapter 5 however that single scattering analysis of XPD data can break down at low emission angles, requiring a multiple scattering approach to reproduce the experimental data. Grazing emission XPD data from the  $c(2 \times 2)$  surface previously analysed by a single scattering approach will be analysed by the present multiple scattering theory.

The chapter is structured as follows. The next section will describe some of the problems which can be encountered when forming the  $\text{Ni}(001)c(2 \times 2)\text{O}$  surface. Some previous analyses of the system will then be described, followed by details of the XPD experiment from which the data is taken for the present calculations. A set of calculations is presented for the hollow site and the optimum overlayer height determined by an R1 analysis. Similar calculations are then presented for a site with the O atoms displaced laterally from the hollow and compared with those for the hollow site. Finally, the effect of relaxing the top Ni-Ni layer spacing outwards will be investigated and the results discussed.

## 6.2 The $\text{Ni}(001)c(2 \times 2)\text{O}$ Surface

### 6.2.1 Problems

Upon exposure of a clean  $\text{Ni}(001)$  surface to oxygen, sub-monolayer adsorption with no disruption of the crystal lattice initially occurs. This leads to the formation of the  $p(2 \times 2)$  and the  $c(2 \times 2)$  structures, which have ideal coverages

of 0.25 monolayers (ML) and 0.5 ML respectively. Oxygen can penetrate into low index Ni surfaces quite easily. The onset of penetration occurs at coverages less than 0.5 ML (the ideal  $c(2 \times 2)$  coverage) at 300K, and thin islands of NiO are formed immediately. Atomic oxygen can also diffuse into the bulk at temperatures of between 450-600K. This means the practice of annealing the surface to intensify the LEED spots corresponding to the overlayer can actually worsen the surface, as it causes any excess surface oxygen to be dissolved into the bulk. Hence, it is possible to have a mixture of chemisorbed oxygen, dissolved oxygen and isolated nuclei of NiO present at coverages less than 0.5 ML. Structural studies of the  $c(2 \times 2)$  surface are therefore very problematic: a particular technique may be sensitive to sub-surface oxygen and affect structural conclusions drawn from the measurements. As NiO nuclei and buried oxygen are difficult to completely avoid, steps should be taken to minimise their contribution in order to deduce information about the overlayer structure.

### 6.2.2 Proposed Models

There has been some controversy in the literature as to the structure of the  $c(2 \times 2)$ O surface, and a number of different structures proposed. A reason for this may be due to the presence of unwanted sub-surface oxygen in some studies, causing problems which have been outlined above. A brief review of some of the proposed models will be given here.

Most early studies of the system were done by comparison of dynamical LEED I-V calculations with experiment. The O atoms were assumed to occupy a four-fold hollow site and the overlayer height  $z$  varied to find the best fit with the data. Andersson *et al.* [78] in 1973 found a best fit of  $z=1.5\text{\AA}$  by this method,

although only the energy range 20-60eV was considered. A subsequent LEED analysis by Demuth *et al.* [79] used a larger energy range and found the optimum  $z$  to be 0.9Å, a figure also supported by the LEED calculations of Van Hove and Tong [80]. In 1980 however, an XPD study by Petersson *et al.* [13] found the most favoured bonding site to be in the same plane as the top layer of Ni atoms ( $z=0.0\text{Å}$ ). Although this in-plane geometry was in conflict with the previous LEED studies, a later theoretical paper by Upton and Goddard [81] gave a value of  $z=0.26\text{Å}$ , only slightly above the in-plane geometry. A further LEED study by Tong and Lau in 1982 [82] considered a wide range of values of  $z$ , and found that the data could be fitted equally well for  $z=0.0\text{Å}$  and for  $z=0.90\text{Å}$ . In another LEED study in 1983, Demuth *et al.* [83] proposed that the O layer had  $z=0.80\text{Å}$ , and that the O atoms were displaced laterally from the fourfold hollow site by 0.30Å in the [110] direction. Bonding away from the fourfold hollow had not been considered previously, and this new proposed position was termed the "pseudobridge" bonding site. In an XPD study by Saiki *et al.* [17] in 1987, the fourfold hollow site at  $z=0.80-0.95\text{Å}$  gave better agreement with the data than the corresponding pseudobridge site, and in a tensor LEED analysis by Oed *et al.* [84] in 1989, the fourfold hollow was again favoured, at a slightly lower bonding height of  $z=0.77\text{Å}$ . In this latter study, buckling and relaxation in the outer two Ni layers were also considered, and sites displaced from the fourfold hollow by more than 0.2Å were ruled out. A later XPD study by Saiki *et al.* [19] supported the lower bonding height proposed by Oed *et al.*, finding optimum agreement at  $z=0.75\text{Å}$ , again favouring the fourfold hollow site rather than the pseudobridge site.

### 6.2.3 XPD Studies

Several studies of the system have been performed using XPD, primarily by the Fadley group. In the paper of Saiki *et al.* [19], XPD was used to study the interaction of oxygen with the Ni(001) surface from the  $c(2 \times 2)$  phase through to the saturated NiO phase at higher O exposures. The study of the  $c(2 \times 2)$  surface in this work was performed by taking azimuthal scans at four take-off angles ranging from  $8^\circ$  to  $17^\circ$ . Some of this data has also been published in the review by Fadley [31], and similar data has appeared in an earlier paper by Saiki *et al.* [17].

The experiment of refs. [19, 31] will be considered in more detail here. Al  $K\alpha$  ( $h\nu = 1486.6\text{eV}$ ) radiation was used to excite the  $1s$  core level of O, resulting in photoelectrons having energy  $954\text{eV}$  outside the solid. Measurements were taken for the  $c(2 \times 2)$  surface obtained from an O exposure of 30 Langmuir, which corresponded to a coverage of 0.38 ML. Even at this low exposure, it was estimated that 10-15% of the O atoms formed small oxide islands. The photoelectrons were collected with a detector having angular resolution of  $\pm 3^\circ$  and four azimuthal scans were taken at polar angles of  $8^\circ$ ,  $11^\circ$ ,  $14^\circ$  and  $17^\circ$ . Directions of X-ray incidence and electron exit were in the same plane, separated by a polar angle of  $72^\circ$ . In order to reduce the emission from oxide islands and from sub-surface O interfering with the signal from the overlayer, only the lowest two data sets,  $\theta = 8^\circ$  and  $\theta = 11^\circ$  were used to perform the structural analysis. Inelastic scattering is enhanced for sub-surface emission at low take-off angles as described earlier. The single-scattering analysis of the data resulted in a best fit with the O atoms in fourfold hollow sites at an adsorption height of  $z=0.75\text{\AA}$ .

### 6.3 Calculations

The aim of the calculations in this chapter is to determine the optimum bonding height of the O atoms using the multiple scattering program, and to investigate the somewhat controversial pseudobridge bonding site proposed by Demuth *et al.* [83]. The effect of introducing a relaxation in the Ni-Ni layer spacing is also investigated towards the end of the chapter. The data used is taken from the experiment described in refs. [19, 31] at two take-off angles of  $\theta = 8^\circ$  and  $\theta = 11^\circ$ . Although data at higher take-off angles is available [19], it is thought to be less reliable due to enhanced sub-surface O contributions, and was not used in the accompanying SS analysis.

#### 6.3.1 Hollow-Site Calculations

Most recent studies of the system, as described in the previous section, place the O atoms in four-fold hollow sites at a vertical height of between 0.75Å and 1.00Å above the outer Ni layer. The first set of calculations presented are for the O atoms occupying such hollow sites, with the optimum adsorption height to be determined. No relaxation in the outer Ni-Ni layer spacing has been allowed.

Calculations have been performed from  $z=0.60\text{Å}$  through to  $z=0.90\text{Å}$  in steps of  $0.05\text{Å}$  for both take-off angles, and the results are presented in Figs. 6.1-6.2. Calculations have also been performed at the in-plane bonding site, a structure proposed by Petersson *et al.* [13], and the structure ruled out. These calculations are not shown here.

An initial observation from these results is that despite the poorer angular resolution, these results are far more sensitive to the adsorption height  $z$  than the calculations which were presented in chapter 5. This is due to the much

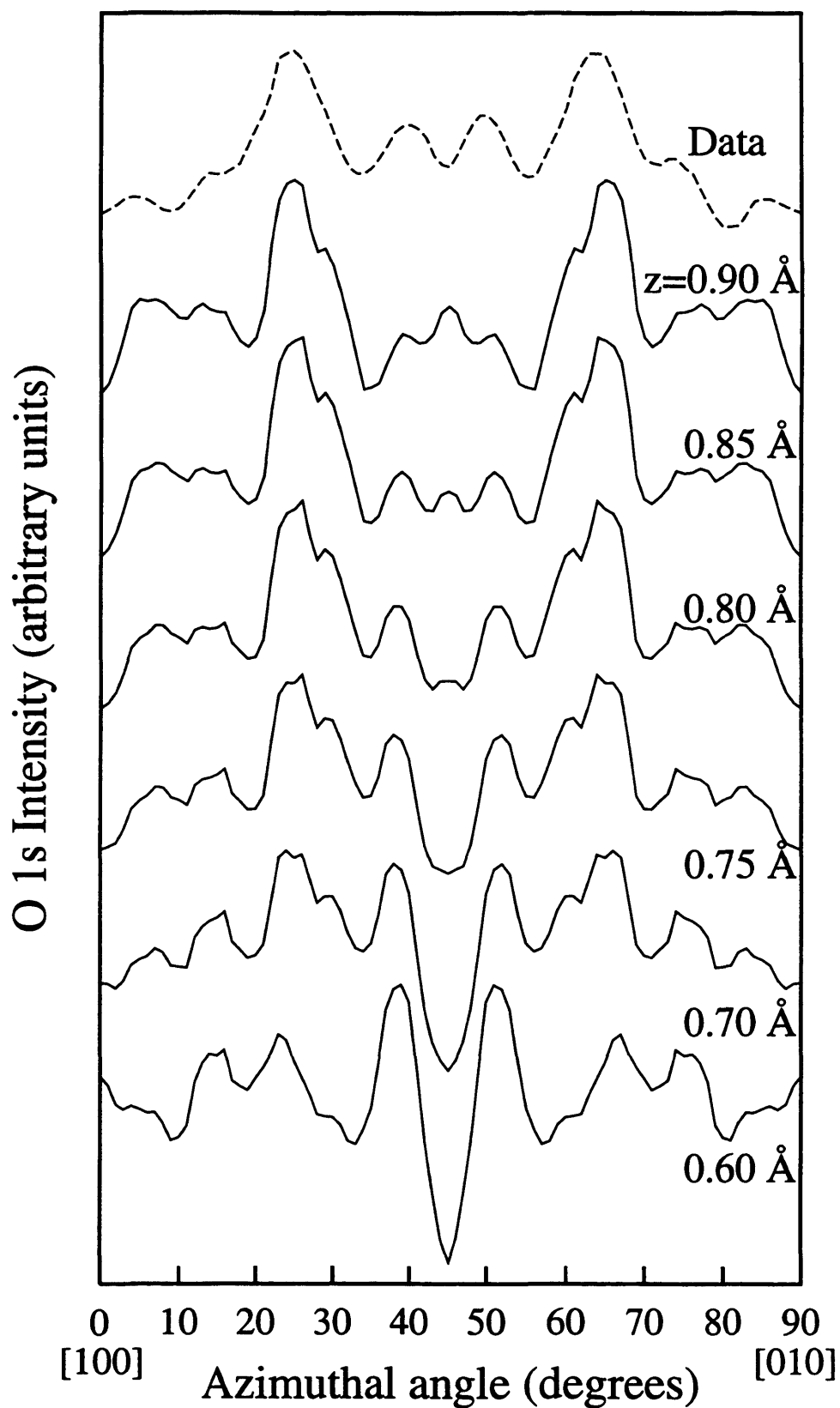


Figure 6.1: Theoretical XPD curves (solid lines) for different adsorption heights of the  $c(2 \times 2)\text{O}$  overlayer on a bulk terminated  $\text{Ni}(001)$  substrate at take-off angle  $\theta = 8^\circ$ . Experimental data (broken line) is from ref. [31]

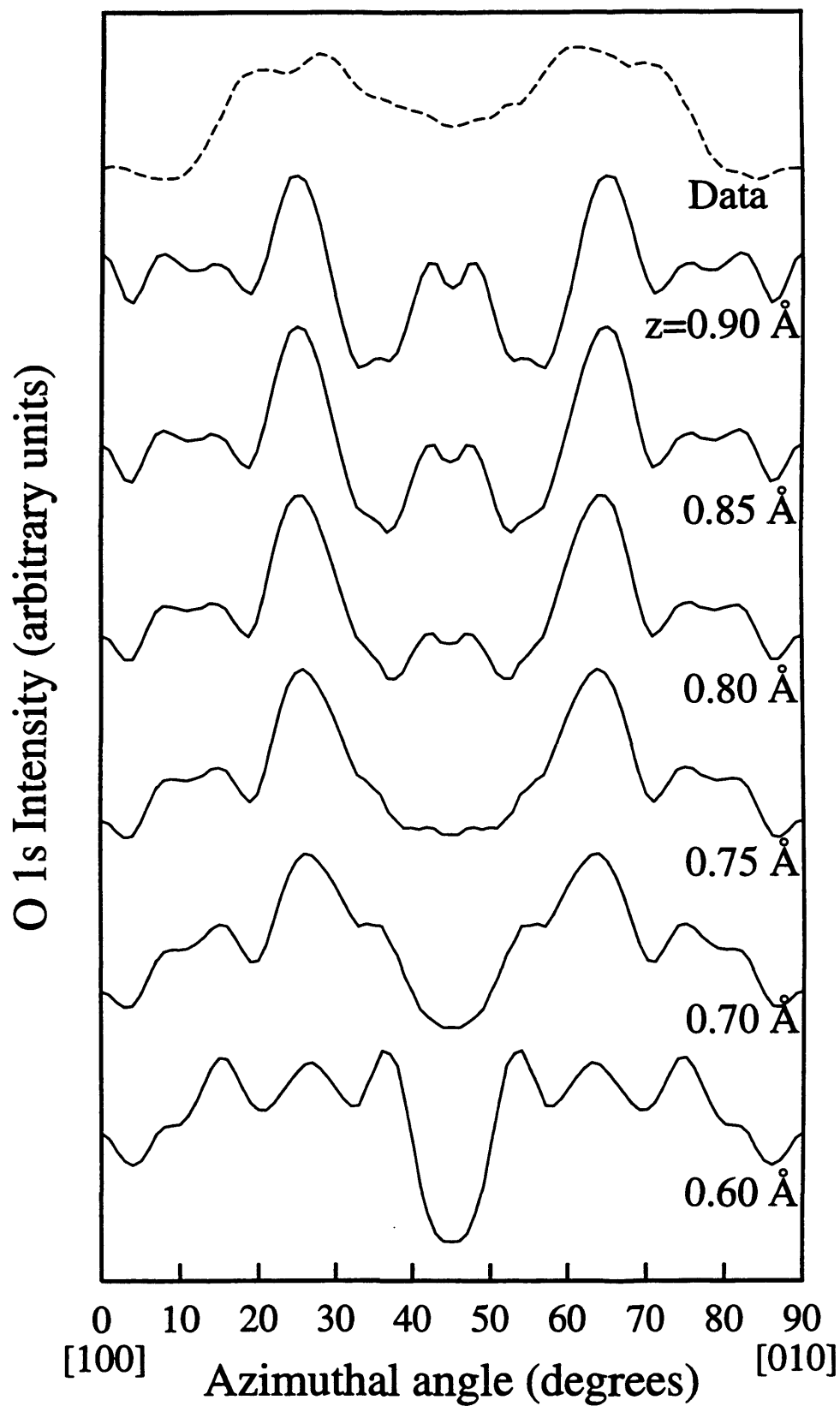


Figure 6.2: Same as Fig. 6.1 but for take-off angle  $\theta = 11^\circ$ .

lower values of  $z$  considered here, meaning the angles involved with scattering from the substrate are lower and the signal consequently stronger. The point has been discussed in chapter 5. For the  $8^\circ$  take-off angle, the calculation at  $z=0.90\text{\AA}$  can be seen to be in poor agreement with the data. Although the peaks at about  $25^\circ$  and  $65^\circ$  are present, the doublet centred around  $45^\circ$  is not, with the calculation predicting a triplet structure with a maximum at  $45^\circ$ . The three calculated curves between  $z=0.85\text{\AA}$  and  $z=0.75\text{\AA}$  are in better agreement with the data. For  $z=0.85\text{\AA}$ , small peaks at about  $40^\circ$  and  $50^\circ$  have developed, although there is still a small peak at  $45^\circ$ . This peak has practically vanished for the  $z=0.80\text{\AA}$  calculation, which is in very good agreement with the data. The  $z=0.75\text{\AA}$  calculation is also in good agreement, although the trough predicted at  $45^\circ$  has become deeper than that in the data, and the peaks at  $25^\circ$  and  $65^\circ$  become slightly smaller. These trends continue as  $z$  is reduced, causing the calculations at  $z=0.70\text{\AA}$  and  $z=0.60\text{\AA}$  to be rather less convincing fits. At  $z=0.60\text{\AA}$ , the curve is dominated by the two peaks at  $40^\circ$  and  $50^\circ$ , and the peaks which were at  $25^\circ$  and  $65^\circ$  hardly recognisable.

A notable feature of the calculations at  $11^\circ$  is the amount of structure on the calculated curves compared with the data. The experimental curve is largely featureless, with two broad peaks which appear to be doublets. On the other hand, the calculated curves, even with averaging to account for the resolution of the experiment display much more structure. None of the calculated curves in Fig. 6.2 reproduce the data as well as for the  $8^\circ$  calculations, however the trends seen in those calculations are present again here. At  $z=0.90\text{\AA}$ , there is quite a prominent doublet at  $45^\circ$  which is not seen in the data. Despite having large peaks at  $25^\circ$  and  $65^\circ$ , there are deep troughs at about  $35^\circ$  and  $55^\circ$  and some

structure in the 10-20° and 70-80° ranges which are also not seen in the data, causing the fit to be poor. At  $z=0.80\text{\AA}$ , the doublet at 45° has become smaller, and has disappeared at  $z=0.75\text{\AA}$ , making this calculation the best visual fit to the data. Agreement is quite good between about 25-65°, although the depth of the valley is predicted to be deeper than observed experimentally. There is still structure predicted in the 10-20° and 70-80° ranges however. The curve at  $z=0.70\text{\AA}$  is quite similar to the  $z=0.75\text{\AA}$  curve, but the valley centred around 45° has become deeper and some shoulder features can be seen at about 37° and 53°. These features can also be seen in the  $z=0.75\text{\AA}$  calculation, but are much weaker. There are hints of such shoulder features in the data, especially the one at 53°, suggesting there is structure which has not been resolved in the experiment. The calculation at  $z=0.60\text{\AA}$  is a poor fit to the data, with the aforementioned shoulders having developed into peaks, and the valley around 45° has become even steeper.

An R1 analysis has been performed on these calculations, R1 having been defined in chapter 5. The average R1 from the  $\theta = 8^\circ$  and  $\theta = 11^\circ$  calculations is shown in Fig. 6.3, and can be seen to display a clear minimum at an adsorption height of  $z=0.75\text{\AA} \pm 0.05\text{\AA}$ . Although this height is lower than the height determined by the majority of studies of the system (0.80-0.90Å), the figure is in good agreement with the XPD study of Saiki *et al.* [19] which gave  $z=0.75\text{\AA}$ , and with the LEED analysis of Oed *et al.* [84] which gave  $z=0.77\text{\AA}$ .

There is some concern about the calculations performed at  $\theta = 11^\circ$ , since they do not produce as good agreement with the data as the calculations at  $\theta = 8^\circ$ . There are several possible reasons for this. It should be remembered that the calculation is for an ideal overlayer system, consisting of a perfectly

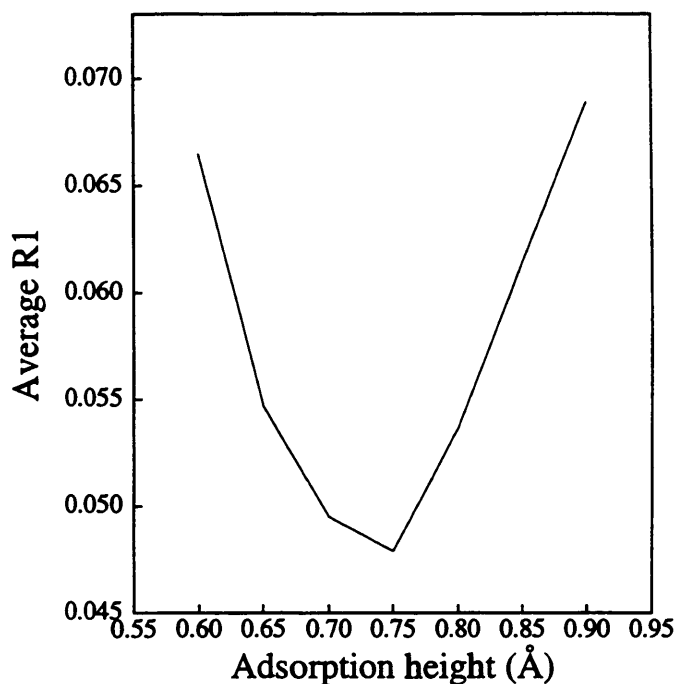


Figure 6.3: The R1 analysis of the calculations in Figs. 6.1 and 6.2

ordered  $c(2 \times 2)$  O layer on a pure Ni substrate. As has been discussed earlier, creating a good overlayer is difficult for this particular system, especially with the tendency for O to diffuse into the bulk or to form pockets of NiO. Any sub-surface O emission picked up in the experimental signal is not accounted for in the calculations, and the contribution will be greater for higher take-off angles. Also, the angular resolution of the experiment is quite low, quoted as  $\pm 3^\circ$ , meaning more averaging of points is needed to produce the theoretical curves.

In summary then, this set of calculations, in which the O atoms were placed in four-fold hollow bonding sites and the Ni substrate was not allowed to relax, give a best fit to the data at  $z=0.75\text{\AA}$  ( $\pm 0.05\text{\AA}$ ). The best fit at  $\theta = 11^\circ$  is not as good as the best fit at  $\theta = 8^\circ$ , which may be due to the greater effects of buried O in the data at  $\theta = 11^\circ$ , or some other non-ideal surface effects.

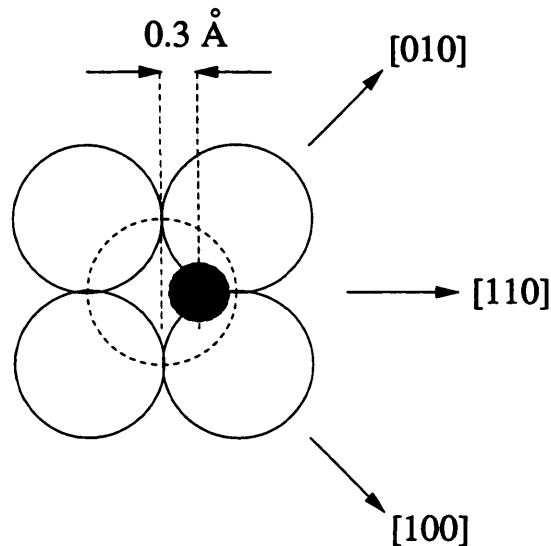


Figure 6.4: Schematic diagram of the pseudobridge geometry proposed by Demuth *et al.* [83]. The O atom (filled circle) is displaced from the hollow site by  $0.30\text{\AA}$  in the [110] direction.

### 6.3.2 The Pseudobridge Site

Most studies of the  $\text{Ni}(001)c(2 \times 2)\text{O}$  system have placed the O atoms in four-fold hollow sites. A LEED study in 1983 by Demuth *et al.* [83] however concluded the hollow site is a local "saddle point" and that an asymmetric pseudobridge site is preferred. This site is illustrated in Fig. 6.4: the O atom, represented by the filled circle, is displaced by  $0.30\text{\AA}$  in the [110] direction.

A set of XPD calculations have been performed for the pseudobridge site in the same way as for the hollow site. The Ni substrate has not been allowed to relax, and the O overlayer has been varied between  $0.70\text{\AA}$  and  $0.95\text{\AA}$  in steps of  $0.05\text{\AA}$ . The calculations, again for the two take-off angles  $\theta = 8^\circ$  and  $\theta = 11^\circ$ , are shown in Figs. 6.5 and 6.6.

The curves at  $\theta = 8^\circ$  in Fig. 6.5 can be seen to be very different to the corresponding calculations for the hollow site. Whereas the best agreement for the hollow site was at  $0.75\text{\AA}$ , the best pseudobridge site is somewhat higher than

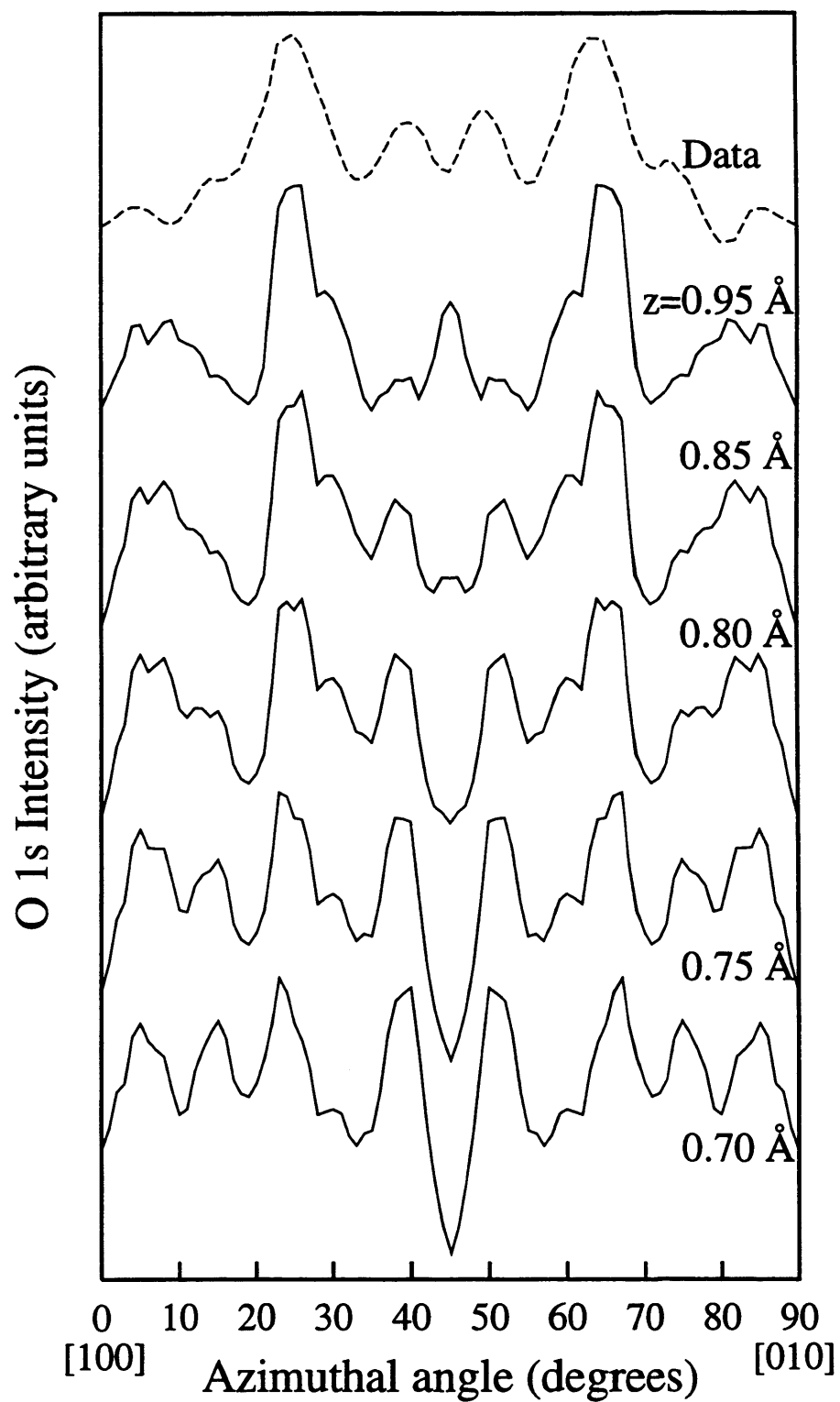


Figure 6.5: Theoretical XPD curves (solid lines) for different adsorption heights of the  $c(2 \times 2)\text{O}$  overlayer, with the O atoms occupying the pseudobridge sites as shown in Fig. 6.4. The take-off angle is  $8^\circ$ .

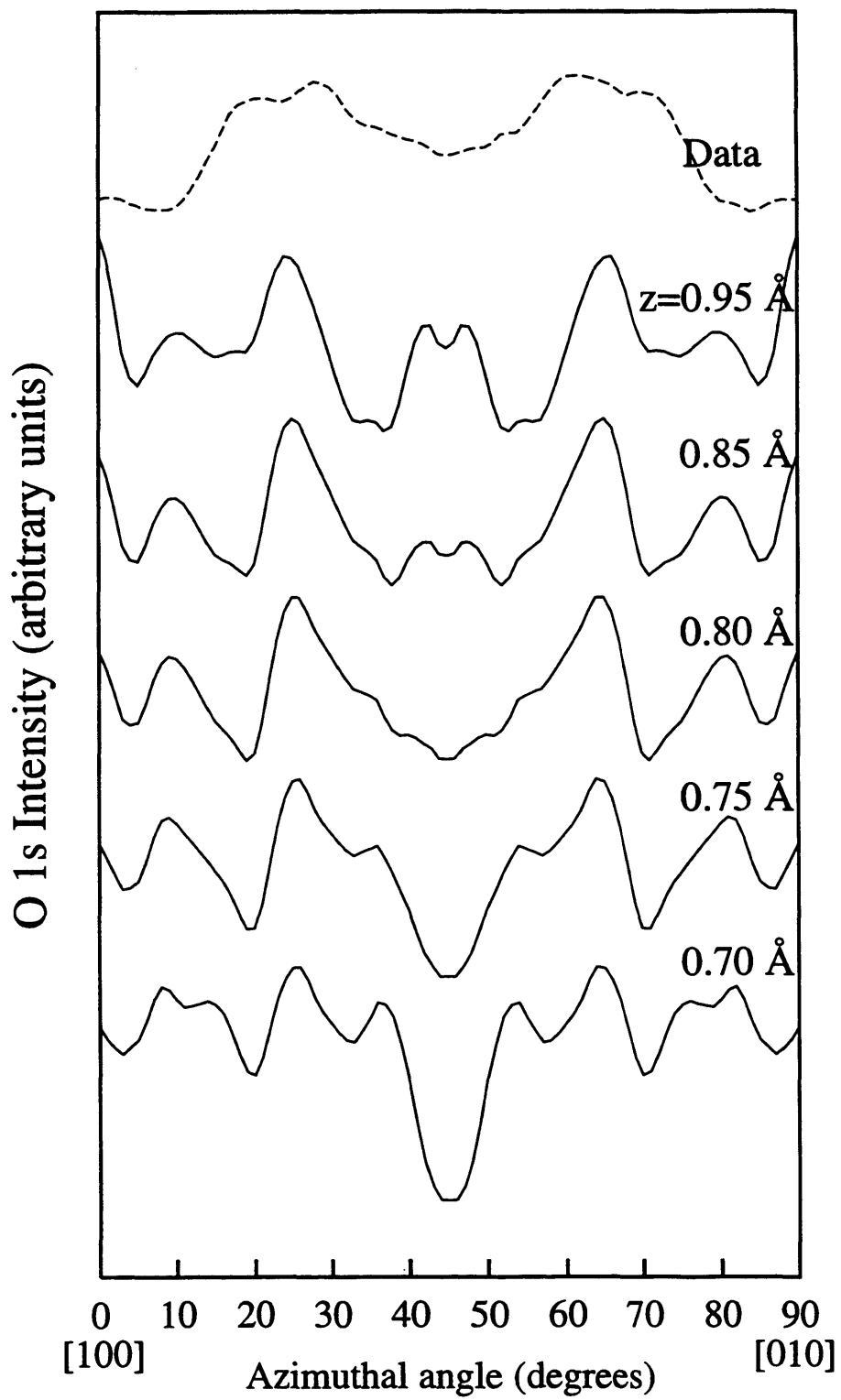


Figure 6.6: Same as Fig. 6.5, but at a take-off angle of  $11^\circ$ .

this at about 0.80-0.85Å. The  $z=0.95\text{Å}$  curve displays a peak at  $45^\circ$ , but this has largely disappeared at  $z=0.85\text{Å}$ , giving excellent agreement with the data in the  $20\text{-}70^\circ$  range. The agreement in the  $0\text{-}20^\circ$  and  $70\text{-}90^\circ$  ranges is decidedly worse however. The shoulders in the data at about  $18^\circ$  and  $72^\circ$  are not predicted, and broad peaks at about  $10^\circ$  and  $80^\circ$  seen which are much larger than in the experiment. The curve at  $z=0.80\text{Å}$  is similar to the  $z=0.85\text{Å}$  curve, except the trough at  $45^\circ$  is slightly more pronounced and the peaks at about  $25^\circ$  and  $65^\circ$  smaller. Again, agreement in the  $0\text{-}20^\circ$  and  $70\text{-}90^\circ$  ranges is poor. These trends are continued as  $z$  is lowered to  $0.75\text{Å}$  and  $0.70\text{Å}$ , with the development of the trough at  $45^\circ$  and the diminishing peaks at  $25^\circ$  and  $65^\circ$  making agreement with the data visibly poorer.

Similar behaviour can be seen for the calculations at  $\theta = 11^\circ$  in Fig. 6.6, in that better agreement with the data occurs at higher  $z$  than for the hollow site. In the hollow calculations of Fig. 6.2, a broad doublet centred upon  $45^\circ$  meant agreement with the data at  $z=0.80\text{Å}$  and above was not good. In the pseudobridge calculations, the same doublet can be seen to have practically disappeared by  $z=0.85\text{Å}$ , giving good agreement in the  $25\text{-}65^\circ$  range for  $z=0.85\text{Å}$  and  $z=0.80\text{Å}$ . At heights below  $z=0.80\text{Å}$ , a pronounced trough develops which is not seen in the data. Again, general agreement with the data of all the pseudobridge calculations at this angle is worse than for  $\theta = 8^\circ$ , as for the hollow calculations. All curves predict structure in the  $0\text{-}20^\circ$  which is not present in the data. Such behaviour was seen in Fig. 6.6 for the hollow site, but the disagreement is far worse for the pseudobridge site.

The R1 analysis of the calculations in Figs. 6.5 and 6.6 is shown in Fig. 6.7. Again the average of the R1 from each polar angle is plotted against adsorption

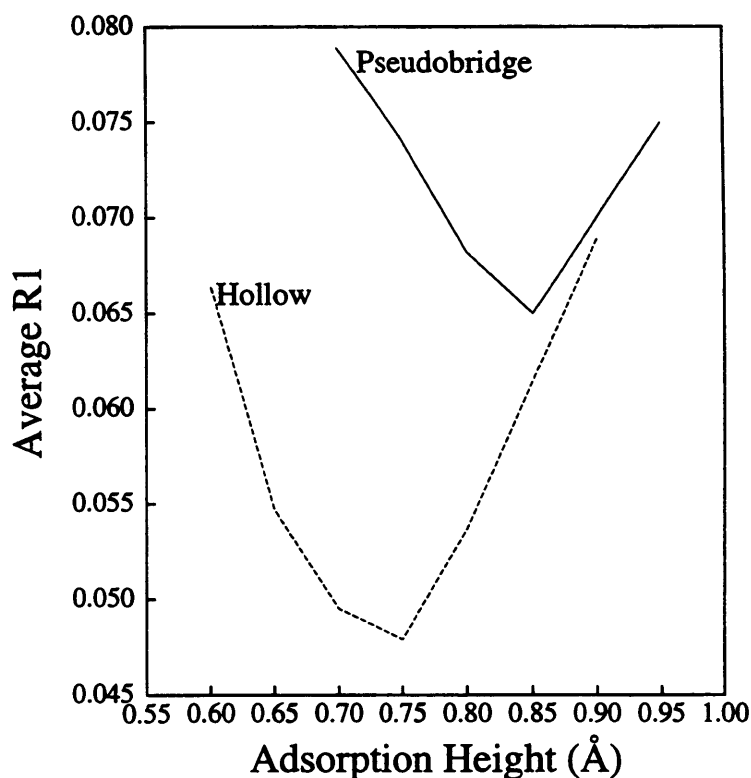


Figure 6.7: The R1 analysis of the calculations in Figs. 6.5 and 6.6. The best pseudobridge site is at  $0.85\text{\AA}$ , but has a far higher minimum R1 compared with the hollow site.

height. From this it is quite clear that although the pseudobridge geometry displays a minimum at  $0.85\text{\AA}$ , the corresponding R1 is much higher than that of the optimum hollow site. These calculations indicate that simple fourfold hollow bonding at an adsorption height of  $0.75\text{\AA}(\pm 0.05\text{\AA})$  provides a far better fit to the data than any height in the pseudobridge geometry of Fig. 6.4.

### 6.3.3 Substrate Relaxation

In the calculations so far, the top Ni-Ni layer spacing ( $d_{12}$ ) has remained at the bulk value of  $1.76\text{\AA}$ . A further set of calculations has been performed in which  $d_{12}$  relaxed outwards from  $1.76\text{\AA}$  to  $1.86\text{\AA}$ , and the overlayer height varied between  $z=0.70\text{\AA}$  and  $0.95\text{\AA}$ . The average R1 factors from the  $8^\circ$  and  $11^\circ$  have

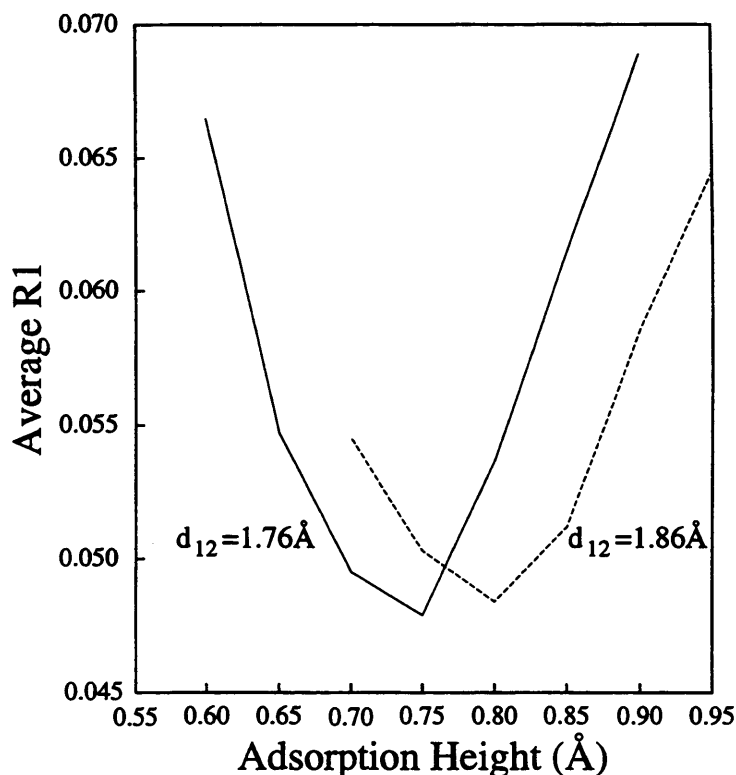


Figure 6.8: R1 curves for  $d_{12}=1.76\text{\AA}$  (bulk value) and  $d_{12}=1.86\text{\AA}$  (5.7% expansion). Both are for the O atoms occupying hollow sites. The two curves have approximately the same minimum R1, occurring at different  $z$  values

been calculated giving the curve shown in Fig. 6.8. The R1 curve from the calculations with  $d_{12}=1.76\text{\AA}$  is also shown in this figure. It can be seen from Fig. 6.8 that both curves display a clear minimum at approximately the same R1 value:  $R1=0.0479$  for the  $d_{12}=1.76\text{\AA}$  calculations and  $R1=0.0484$  for  $d_{12}=1.86\text{\AA}$ . The minimum is shifted to a higher  $z$  value of  $0.80\text{\AA}$  when  $d_{12}=1.86\text{\AA}$  however. Given the low angular resolution of the data, the problems associated with a non-ideal experimental surface and the limited data set, it is not possible to conclude that the structure with the slightly lower R1 is favoured. These calculations cannot distinguish between the two structures.

What is clear from Fig. 6.8 however is that the calculations are very sensitive

to  $d_{12}$ , more so than for similar calculations on the S/Ni system (Fig. 5.9), where the S atoms adsorbed at a much higher  $z$ . Hence with increased experimental resolution, as seen in the previous chapter and a larger set of reliable experimental data, the two best-fit structures above should be able to be separated, and  $z$  and  $d_{12}$  accurately determined for this system.

#### 6.4 Discussion

An extensive set of calculations have been performed for the Ni(001) $c(2 \times 2)$ O system. The fourfold hollow site has proved to be more favourable than the pseudobridge geometry of Demuth *et al.* [83], with an optimum adsorption height of 0.75Å. This is in good agreement with results of the single scattering XPD analysis of Saiki *et al.* [19] and the LEED analysis of Oed *et al.* [84]. A further set of calculations for the hollow site have been performed with the top Ni-Ni layer spacing ( $d_{12}$ ) relaxed outwards to 1.86Å. A minimum in the R1 curve is seen at an overlayer height of 0.80Å, this minimum being only slightly higher than the minimum in the unrelaxed R1 curve. Previous studies have found better agreement with such an outward relaxation in  $d_{12}$  [84].

The quality of reproduction of the experimental curves was in general not as good as for the S/Ni system dealt with in the previous chapter. Calculations for the lowest take-off angle of 8° are in better agreement with the data than those at 11°. There are several possible reasons for this. The calculations are for a surface possessing perfect translational symmetry: effects such as surface roughness and finite domain size are not accounted for. There are also the problems surrounding unwanted sub-surface O contributing more to the signal at higher take-off angles. Such effects are also not accounted for.

A notable feature of the calculations in this chapter is that despite the increased amount of broadening required, they are far more sensitive to variations in the structural parameters than the calculations in the previous chapter. The XPD study of Ni(001) $c(2 \times 2)$ S [18] in chapter 5 has shown that high resolution experiments reveal enhanced fine structure in the data, especially at the lower take-off angles. The use of such equipment to collect data for the  $c(2 \times 2)$ O surface would clearly allow a more accurate study of the system to be performed, especially from a theoretical point of view, since it would involve less broadening of the calculations in order to compare with the data. This would allow far more accurate determination of adsorption height, substrate relaxation and possible off-centre displacement of the O atoms than has been possible with the present data.

## Chapter 7

### Summary and Conclusions

In this thesis, a new theoretical approach to X-ray photoelectron diffraction (XPD) is developed. Although kinematic scattering theories of XPD have been developed, some being quite sophisticated, they do not describe the full multiple scattering of the photoelectron and have been shown to be inadequate in certain cases. To be completely general, a fully dynamical theory is required.

Most of such contemporary theories use a partial wave expansion of the photoelectron wave function, subsequent scattering by the surrounding ion cores being described by an associated set of phase shifts. This approach is similar to that used in LEED calculations, and at energies around 200eV and below, only a few partial waves are needed. This number rises rapidly with electron energy, as the scattering becomes more asymmetric. Most XPD studies utilise electrons in the 500-1500eV range, and so multiple scattering theories based on the partial wave expansion require the retention of many waves. Typically, CPU time for cluster calculations as described in chapter 2 scales as the fourth power of  $l$ , the number of angular momentum states retained. At high photoelectron energies, the partial wave approach can require vast amount of CPU time, even supercomputer facilities in order to perform fully converged calculations.

Whereas other methods apply low energy scattering techniques to the XPD energy range, the present method approaches the multiple scattering problem from the other extreme. For reflection high energy electron diffraction (RHEED), which utilises energies of 10keV and above, a plane wave expansion of the wave function provides the most efficient solution, with only a few waves being required for the most simple surfaces. At XPD energies, more waves need to be included in the wave function expansion, but the approach remains more efficient than the partial wave approach above approximately 1000eV.

In chapter 2, the theoretical framework for the calculation is set up. The intensity is calculated from a dipole matrix element between an initial core state and a fully dynamical final state. The final state is taken to be a time-reversed RHEED wave function, which requires the surface have translational symmetry so that it may be expanded in terms of the reciprocal mesh vectors. The initial state is expressed analytically as a linear combination of Slater orbitals, with the relevant parameters taken from the literature. No assumptions are made about how the final state is calculated, just that it takes a certain mathematical form. From here, the integrals over the  $x$  and  $y$  co-ordinates (parallel to the surface) are performed analytically, reducing the calculation to an integral over the  $z$  (perpendicular) co-ordinate. Different types of emitter, magnetic sub-shells and the polarisation of the X-ray beam are all fully accounted for.

The remaining integration over the  $z$  co-ordinate is addressed in chapter 3. This is done numerically by the modification of a RHEED computer program. The program uses scattering matrices to describe the scattering properties of two-dimensional slices of the structure, and they are combined via the layer doubling algorithm to calculate the RHEED intensities. The problem encountered

when converting the program to perform the XPD calculation is extracting the  $z$ -dependent components of the wave function from the scattering matrix calculations. These components are never explicitly calculated in the program, and the problem is further complicated by the limited numerical integration range allowed in the program to retain numerical accuracy when strong evanescent waves are present. The strong localisation of the initial core state allows a convenient solution by separating the relatively small  $z$  range which contributes to the matrix element integration. A method is devised whereby the integration may be performed over this smaller range.

There are some limitations to this approach to the XPD calculation. The method is applicable to periodic surfaces only, and from a computational point of view, it is difficult to achieve convergence at energies below about 900eV. The XPD program is approximately 25% slower than the original RHEED program because of the extra calculations involved. It also requires more memory in order to store the matrices needed to perform the matrix element integration. The angular resolution of the experiment is another limiting factor, as extra calculations are always required to simulate broadening in the polar ( $\theta$ ) direction for azimuthal scans. The limitations of the calculation are demonstrated in chapter 4. For the Ni(001) $c(2 \times 2)$ O surface with photoelectron energy 954eV, convergence is shown to occur with about 150 beams. Calculations for the Si(111)- $\sqrt{3} \times \sqrt{3}$  Sb surface with photoelectron energy 738eV and a slightly larger unit cell, are shown to require about 230 beams to converge. Computer time scales approximately as  $n^3$ , where  $n$  is the number of beams, and this second system is beyond the capabilities of the present method with the computing resources available, especially when coupled with the rather poor angular resolution of the

experimental data. As noted in chapter 4, methods based on the partial wave expansion are applied to the high energy range using supercomputing facilities. Similar facilities would certainly allow this method to be applied to systems which prove difficult to converge, either because of the low energies or the presence of strong scattering atoms.

The method has been compared with experimental data in chapters 5 and 6. In chapter 5, calculations are performed for the Ni(001) $c(2 \times 2)$ S system, for which an excellent set of high resolution XPD data is available from the literature. The system has been studied at length previously and the structure is quite well understood. Calculations have been performed for all four polar angles available and are in good agreement with the data. Quantitative comparison with the data is performed via an R-factor analysis. Despite the weak sensitivity of the calculations to surface parameters because of the high adsorbate-substrate registry, the R-factors considered give best agreement with the S atoms in fourfold hollow sites at a vertical height of 1.30-1.35Å above the underlying Ni, in good agreement with other studies. A further set of calculations indicate that R-factor can be improved by relaxing the top Ni-Ni spacing outwards slightly. The calculations are compared with single scattering calculations for the same system and are clearly superior at the lowest take-off angle.

The XPD program is applied to Ni(001) $c(2 \times 2)$ O in chapter 6. The system is not as well defined as for the previous system, with many often conflicting structures having been proposed in the literature. Although data is available for four take-off angles, calculations are performed the two lowest only since they are thought to be the most reliable. The calculations display far more sensitivity to surface parameters than for the previous S/Ni system due to the lower adsorption

height. Calculations are again in good agreement with the data despite having to be broadened more to simulate the lower angular resolution of the data. Optimum agreement is with the O atoms occupying fourfold hollow sites at  $0.75\text{\AA}$  above the unrelaxed Ni substrate. Allowing the top Ni layer to relax outwards by  $0.1\text{\AA}$ , fourfold hollow bonding with the O atoms  $0.80\text{\AA}$  above the top Ni layer gives an equally good fit to the data. The pseudobridge site proposed in the literature, in which the O atoms are displaced by  $0.3\text{\AA}$  from their hollow sites is considered and ruled out.

The limitations outlined above could be relaxed somewhat with more efficient RHEED calculations for large beam sets. Maksym [52] has recently described a fast Fourier transform method in which for large  $n$ ,  $n$  being the number of beams, computer time scales as  $16n^2\log(n)$ . For calculations involving more than about 75 beams, this new program is more efficient than the  $n^3$  program. A new method is being developed [60] in which several thousand beams can be routinely and efficiently handled. An interesting prospect for future work would be to use a RHEED program capable of handling enormous beam sets. The general method to perform the XPD calculation using a RHEED wave function has been established in chapter 2, where only the mathematical form of the wave function was used. Some further work would be required to modify the program should the approach to calculating the RHEED intensities be different than that given in chapter 3, but this may be easier if the wave function in the surface layers is more readily accessible. This would also relieve the memory requirements of the current method used to extract the wave function. With the prospect of many thousands of beams being routinely handled, convergence at lower energies could be straightforwardly achieved, limited only by the accuracy of the Doyle-Turner

potential. The subject of the Doyle-Turner potential is discussed in chapter 4. Surface disorder is usually treated by defining a very large unit cell and simulating the disorder within that cell. The large real space translation vectors mean a very dense reciprocal mesh and consequently a very large beam set. This restricts the present XPD calculation to ordered surfaces, but this restriction would be eased by a similarly modified RHEED program capable of handling enormous beam sets. Hence, in principle, the limitations of the present program could be largely removed, resulting in a much wider range of applications.

## APPENDIX A

### Evaluation of Integral $\mathcal{I}$

The derivation of photoemission formulae in chapter 2 requires the evaluation of an integral  $\mathcal{I}$  which takes the form

$$\mathcal{I} = \int \exp(i\mathbf{k}\cdot\boldsymbol{\rho}) \exp(-\beta r) d\boldsymbol{\rho}, \quad (\text{A.1})$$

where  $\mathbf{k}$  is the vector  $(k_x, k_y)$ ,  $\boldsymbol{\rho}$  is the vector  $(x, y)$  and  $d\boldsymbol{\rho}$  is the element of area  $dx dy$ . This appendix shows how  $\mathcal{I}$  may be evaluated analytically.

First, the aim is to find an expression for  $\exp(-\beta r)$  in terms of a three dimensional vector  $\mathbf{r}$ . Define the pair of Fourier transforms  $\Phi(\mathbf{r})$  and  $\tilde{\Phi}(\mathbf{q})$  by

$$\Phi(\mathbf{r}) = \frac{1}{(2\pi)^3} \int \tilde{\Phi}(\mathbf{q}) \exp(-i\mathbf{q} \cdot \mathbf{r}) d\mathbf{q} \quad (\text{A.2})$$

$$\tilde{\Phi}(\mathbf{q}) = \int \Phi(\mathbf{r}) \exp(i\mathbf{q} \cdot \mathbf{r}) d\mathbf{r}. \quad (\text{A.3})$$

Substituting (A.2) into (A.3) gives

$$\Phi(\mathbf{r}) = \frac{1}{(2\pi)^3} \int \left\{ \int \Phi(\mathbf{r}') \exp(i\mathbf{q} \cdot \mathbf{r}') d\mathbf{r}' \right\} \exp(-i\mathbf{q} \cdot \mathbf{r}) d\mathbf{q}. \quad (\text{A.4})$$

By now setting  $\Phi(\mathbf{r}) = \exp(-\beta r)$ , (A.4) becomes

$$\exp(-\beta r) = \frac{1}{(2\pi)^3} \int \left\{ \int \exp(-\beta r') \exp(i\mathbf{q} \cdot \mathbf{r}') d\mathbf{r}' \right\} \exp(-i\mathbf{q} \cdot \mathbf{r}) d\mathbf{q}. \quad (\text{A.5})$$

The parenthesised integral in (A.5) over  $\mathbf{r}'$  can be evaluated by standard methods, the result being

$$\int \exp(-\beta r') \exp(i\mathbf{q} \cdot \mathbf{r}') d\mathbf{r}' = \frac{8\pi\beta}{(\beta^2 + q^2)^2}, \quad (\text{A.6})$$

and hence  $\exp(-\beta r)$  may be written in integral form as

$$\exp(-\beta r) = \frac{4\beta}{(2\pi)^2} \int \frac{\exp(-i\mathbf{q} \cdot \mathbf{r})}{(\beta^2 + q^2)^2} d\mathbf{q}. \quad (\text{A.7})$$

Eq. (A.7) is the expression required,  $\exp(-\beta r)$  written in terms of the three dimensional vector  $\mathbf{r}$ . This can be used to simplify the required integral, Eq. (A.1).

Direct substitution of this integral representation of  $\exp(-\beta r)$  in (A.1) gives

$$\mathcal{I} = \frac{4\beta}{(2\pi)^2} \int \frac{\exp(i\mathbf{k} \cdot \boldsymbol{\rho}) \exp(-i\mathbf{q} \cdot \mathbf{r})}{(\beta^2 + q^2)^2} d\mathbf{q} d\boldsymbol{\rho}, \quad (\text{A.8})$$

which can be more conveniently re-written as

$$\mathcal{I} = \frac{4\beta}{(2\pi)^2} \int \frac{\exp[i(\mathbf{k} - \mathbf{q}_{\parallel}) \cdot \boldsymbol{\rho}] \exp(-iq_z z)}{(\beta^2 + q^2)^2} d\mathbf{q} d\boldsymbol{\rho}, \quad (\text{A.9})$$

where  $\mathbf{q}_{\parallel}$  is the two dimensional vector  $(q_x, q_y)$ . The integral over  $\boldsymbol{\rho}$  in (A.9) can be seen to be a two dimensional delta function

$$\int \exp[i(\mathbf{k} - \mathbf{q}_{\parallel}) \cdot \boldsymbol{\rho}] d\boldsymbol{\rho} = (2\pi)^2 \delta(\mathbf{k} - \mathbf{q}_{\parallel}), \quad (\text{A.10})$$

and using this result in (A.9) gives

$$\mathcal{I} = 4\beta \int_{-\infty}^{\infty} \frac{\exp(-iq_z z)}{(\beta^2 + k^2 + q_z^2)^2} dq_z. \quad (\text{A.11})$$

In reaching (A.11), the relation  $q^2 = \mathbf{q}_{\parallel}^2 + q_z^2$  has been used, and then  $\mathbf{q}_{\parallel}$  replaced by  $\mathbf{k}$  following the result (A.10). This can be simplified by writing (A.11) as

$$\mathcal{I} = -4\beta \frac{\partial}{\partial(k^2)} \int_{-\infty}^{\infty} \frac{\exp(-iq_z z)}{\beta^2 + k^2 + q_z^2} dq_z, \quad (\text{A.12})$$

which removes the square from the denominator of the integrand. The integral in (A.12) is more straightforward than that in (A.11) since it has simple poles at  $q_z = \pm i(\beta^2 + k^2)^{1/2}$ . Let the integral in (A.12) be denoted by  $J$ .  $J$  can be evaluated in the complex plane, closing the contour in the lower half-plane for positive  $z$ , and in the upper half-plane for negative  $z$ . The two results are

$$J(z > 0) = \frac{\pi \exp[-z(\beta^2 + k^2)^{\frac{1}{2}}]}{(\beta^2 + k^2)^{\frac{1}{2}}}, \quad (\text{A.13})$$

$$J(z < 0) = \frac{\pi \exp[+z(\beta^2 + k^2)^{\frac{1}{2}}]}{(\beta^2 + k^2)^{\frac{1}{2}}}. \quad (\text{A.14})$$

These two results can be combined by recognising that the sign of the exponent is negative in both cases, and hence

$$J = \frac{\pi \exp[-|z|(\beta^2 + k^2)^{\frac{1}{2}}]}{(\beta^2 + k^2)^{\frac{1}{2}}}. \quad (\text{A.15})$$

Integral  $\mathcal{I}$  can now be evaluated by using result (A.12),

$$\mathcal{I} = -4\beta \frac{\partial J}{\partial(k^2)}. \quad (\text{A.16})$$

The differentiation can be performed using Eq. (A.15), giving

$$\frac{\partial J}{\partial(k^2)} = -\frac{\pi}{2(\beta^2 + k^2)^{\frac{3}{2}}} \left[ 1 + |z|(\beta^2 + k^2)^{\frac{1}{2}} \right] \exp[-|z|(\beta^2 + k^2)^{\frac{1}{2}}], \quad (\text{A.17})$$

and hence the desired result

$$\mathcal{I} = 2\pi\beta \frac{\exp(-|z|b)}{b^3} (1 + |z|b), \quad (\text{A.18})$$

where the parameter  $b$  is defined by

$$b^2 = \beta^2 + k^2. \quad (\text{A.19})$$

## Bibliography

- [1] M. Prutton, *Surface Physics, 2nd Ed.* (Oxford University Press, Oxford 1983)
- [2] A. Zangwill, *Physics at Surfaces* (Cambridge University Press, Cambridge 1988)
- [3] A. Leibsch, *Phys. Rev. Lett.* **32** (1974) 1203
- [4] D. P. Woodruff, D. Norman, B. W. Holland, N. V. Smith, H. H. Farrell and M. M. Traum, *Phys. Rev. Lett.* **41** (1978) 1130
- [5] S. Kono, S. M. Goldberg, N. F. T. Hall and C. S. Fadley, *Phys. Rev. Lett.* **41** (1978) 1831
- [6] S. D. Kevan, D. H. Rosenblatt, D. Denley, B-C Lu and D. A. Shirley *Phys. Rev. Lett.* **41** (1978) 1565
- [7] D. P. Woodruff, A. L. D. Kilcoyne, C. F. McConville, Th. Lindner, J. Somers *et al.*, *Vacuum* **38** (1988) 305
- [8] D. P. Woodruff, C. F. McConville, A. L. D. Kilcoyne, Th. Lindner, J. Somers *et al.*, *Surf. Sci.* **201** (1988) 228
- [9] Th. Lindner, J. Somers, A. M. Bradshaw, A. L. D. Kilcoyne and D. P. Woodruff, *Surf. Sci.* **203** (1988) 333

- [10] O. Schaff, G. Hoss, V. Fernandez, K.-M. Schindler, A. Theobald, Ph. Hoffman, A. M. Bradshaw, V. Fritzsche, R. Davis and D. P. Woodruff, *J. Electron Spectrosc. Relat. Phenom* **75** (1995) 117
- [11] K.-U. Weiss, R. Dippel, K.-M. Schindler, P. Gardner, V. Fritzsche, A. M. Bradshaw, A. L. D. Kilcoyne and D. P. Woodruff, *Phys. Rev. Lett.* **69** (1992) 3196
- [12] S. Kono, S. M. Goldberg, N. F. T. Hall and C. S. Fadley, *Phys. Rev. B* **22** (1980) 6085
- [13] L.-G. Petersson, S. Kono, N. F. T. Hall, S. Goldberg, J. T. Lloyd, C. S. Fadley and J. B. Pendry, *Mater. Sci. Eng.* **42** (1980) 111
- [14] H. Takahashi, M. Sasaki, S. Suzuki, S. Sato, T. Abukawa, S. Kono and J. Osterwalder *Surf. Sci* **304** (1994) 65
- [15] X. Chen, T. Abukawa, J. Tani and S.Kono *Phys. Rev. B* **52** (1995) 12380
- [16] X. Chen, T. Abukawa and S.Kono *Surf. Sci.* **356** (1996) 28
- [17] R. S. Saiki, A. P. Kaduwela, J. Osterwalder, M. Sagurton, C. S. Fadley and C. R. Brundle, *J. Vac. Sci. Technol. A* **5** (1987) 932
- [18] R. S. Saiki, A. P. Kaduwela, Y. J. Kim, D. J. Friedman, J. Osterwalder, S. Thevuthasen and C. S. Fadley, *Surf. Sci.* **279** (1992) 305
- [19] R. S. Saiki, A. P. Kaduwela, M. Sagurton, J. Osterwalder, D. J. Friedman, C. S. Fadley and C. R. Brundle, *Surf. Sci.* **282** (1993) 33
- [20] A. L. D. Kilcoyne, D. P. Woodruff, Th. Lindner, J. Somers and A. M. Bradshaw, *J. Vac. Sci. Technol. A* **7** (1989) 1926

- [21] M. E. Davilla, M. C. Asensio, D. P. Woodruff, K.-M. Schindler, Ph. Hoffman, S. Bao, V. Fritzsche and A. M. Braddshaw, *Surf. Sc.* **359** (1996) 185
- [22] W. N. Mei and S. Y. Tong, *Phys. Rev. B* **33** (1986) 1408
- [23] B. Sinkovic and C. S. Fadley, *Phys. Rev. B* **31** (1985) 4665
- [24] V. Fritzsche, *J. Phys. Condens. Matter* **2** (1990) 1413
- [25] D. J. Friedman and C. S. Fadley, *J. Electron Spectrosc. Relat. Phenom.* **51** (1990) 689
- [26] D. K. Saldin, G. R. Harp and X. Chen, *Phys. Rev. B* **48** (1993) 8234
- [27] A. P. Kaduwela, D. J. Friedman and C. S. Fadley, *J. Electron Spectrosc. Relat. Phenom.* **57** (1991) 223
- [28] M. Fink and J. Ingram, *At. Data Nucl. Data Tables* **4** (1972) 129
- [29] D. P. Woodruff, *Surf. Sci.* **299/300** (1994) 183
- [30] D. P. Woodruff and A. M. Bradshaw, *Rep. Prog. Phys.* **57** (1994) 1029
- [31] C. S. Fadley, chapter in *Synchrotron Radiation Research: Advances in Surface and Interface Science Vol. 1* (Plenum, New York 1992) and references therein
- [32] W. F. Egelhoff Jr., chapter in *Ultrathin Magnetic Structures I: An Introduction to Electronic, Magnetic and Structural Properties* edited by J. A. C. Bland and B. Heinrich (Springer-Verlag, Berlin 1994)
- [33] J. J. Barton, *Phys. Rev. Lett.*, **61** (1988) 1356

- [34] L. J. Terminello, B. L. Petersen and J. J. Barton, *J. Electron Spectrosc. Relat. Phenom.* **75** (1995) 299
- [35] P. A. Lee and J. B. Pendry, *Phys. Rev. B* **11** (1975) 2795
- [36] H. S. Poon and S. Y. Tong, *Phys. Rev. B* **22** (1984) 6211
- [37] M-L Xu and M. A. Van Hove, *Surf. Sci.* **207** (1989) 215
- [38] J. B. Pendry, *Surf. Sci.* **57** (1976) 679
- [39] C. H. Li, A. R. Lubinsky and S. Y. Tong, *Phys. Rev. B* **17** (1978) 3128
- [40] G. D. Mahan, *Phys. Rev. B* **2** (1970) 4334
- [41] P. J. Fiebelman and D. E. Eastman, *Phys. Rev. B* **10** (1974) 4932
- [42] J. E. Inglesfield and E. W. Plummer in *Angle Resolved Photoemission, Theory and Current Applications (Studies in Surface Science and Catalysis 74)* edited by S. D. Kevan (Elsevier 1992)
- [43] D. J. Spanjaard, D. W. Jepsen and P. M. Marcus, *Phys. Rev. B* **15** (1977) 1728
- [44] L. E. Schiff, *Quantum Mechanics (2nd Ed.)* (McGraw-Hill, New York 1955)
- [45] E. Clementi and C. Roetti, *At. Data Nucl. Data Tables* **14** (1974) 177
- [46] P. A. Maksym and J. J. Beeby, *Surf. Sci.* **110** (1981) 423
- [47] P. A. Maksym in *Thin film Growth Techniques for Low Dimensional Structures*, edited by R. F. C. Farrow, S. S. P. Parkin, P. J. Dobson, J. H. Neave and A. S. Arrott (Plenum, New York 1987)

- [48] P. A. Maksym, *Surf. Sci.* **149** (1985) 157
- [49] A. Ichimiya, *Jpn. J. Appl. Phys.* **22** (1983) 176
- [50] H. Marten and G. Meyer-Ehmsen, *Surf. Sci.* **151** (1985) 570
- [51] T. C. Zhao, H. C. Poon and S. Y. Tong, *Phys. Rev. B* **38** (1988) 1172
- [52] P. A. Maksym, *Surf. Rev. Lett.* to be published
- [53] P. A. Doyle and P. S. Turner, *Acta. Cryst.* **A24** (1968) 390
- [54] S. L. Dudarev, L. M. Peng and M. J. Whelan, *Surf. Sci.* **330** (1995) 88
- [55] G. H. Smith and R. E. Burge, *Acta. Cryst.* **15** (1962) 182
- [56] G. Radi, *Acta. Cryst.* **A26** (1970) 41
- [57] D. M. Bird and Q. A. King, *Acta. Cryst.* **A46** (1990) 202
- [58] J. B. Pendry, *Low Energy Electron Diffraction* (Academic, New York 1974)
- [59] The program MUF POT, written by J. B. Pendry including some modifications by S. J. Gurman.
- [60] P. A. Maksym, private communication
- [61] S. Kono, private communication
- [62] J. Oudar in *Metal Support and Metal Additive Effects in Surface Science and Catalysis* edited by B. Imelik, c. Naccache, G. Coudourier, H. Praulaud, P. Meriaudeau, P. Gallezot, G. A. Martin and J. C. Vedrine (Elsevier, Amsterdam 1982)

- [63] M. MacLaren, J. B. Pendry, D. D. Vvedensky and R. W. Joyner, *Surf. Sci.* **162** (1985) 322
- [64] U. Starke, F. Bothe, W. Oed and K. Heinz, *Surf. Sci.* **232** (1990) 56
- [65] W. Oed, U. Starke, F. Bothe and K. Heinz, *Surf. Sci.* **234** (1990) 72
- [66] W. Oed, U. Starke, K. Heinz, K. Müller and J. B. Pendry, *Surf. Sci.* **251/252** (1991) 488
- [67] D. H. Rosenblatt, S. D. Kevan, J. G. Tobin, R. F. Davis, M. G. Mason, D. R. Denley, D. A. Shirley, Y. Huang and S. Y. Tong, *Phys. Rev. B* **26** (1982) 1812
- [68] A. Partridge, G. J. Tatlock, F. M. Leibsle, C. F. J. Flipse, G. Hörmandinger and J. B. Pendry, *Phys. Rev. B* **48** (1993) 8267
- [69] F. Sette, T. Hashizume, F. Comin, A. A. MacDowell and P. H. Citrin, *Phys. Rev. Lett.* **61** (1988) 1384
- [70] J. J. Barton, S. W. Robey and D. A. Shirley, *Phys. Rev. B* **34** (1986) 778
- [71] J. Osterwalder, E. A. Stewart, D. Cyr, C. S. Fadley, J. Mustre de Leon and J. J. Rehr, *Phys. Rev. B* **35** (1987) 9859
- [72] M. A. Van Hove, S. Y. Tong and M. E. Elconin, *Surf. Sci.* **64** (1977) 85
- [73] P. H. Holloway and J. B. Hudson, *Surf. Sci.* **43** (1974) 123
- [74] P. H. Holloway and R. A. Outlaw, *Surf. Sci.* **111** (1981) 300
- [75] P. R. Norton, R. L. Tapping and J. W. Goodale, *Surf. Sci.* **65** (1977) 13
- [76] C. R. Brundle and H. Hopster, *J. Vac. Sci. Technol.* **18** (1981) 663

- [77] C. R. Brundle and J. Q. Broughton in *The Chemical Physics of Solid Surfaces and Heterogeneous Catalysis* Vol. 3a, edited by D. A. King and D. P. Woodruff (North-Holland, Amsterdam, 1991)
- [78] S. Andersson, B. Kasemo, J. B. Pendry and M. A. Van Hove, *Phys. Rev. Lett.* **31** (1973) 595
- [79] J. E. Demuth and T. N. Rhodin, *Surf. Sci.* **45** (1974) 249
- [80] M. A. Van Hove and S. Y. Tong, *J. Vac. Sci. Technol.* **12** (1975) 230
- [81] T. Upton and W. A. Goddard III, *Phys. Rev. Lett.* **46** (1981) 1635
- [82] S. Y. Tong and K. H. Lau, *Phys. Rev. B* **25** (1982) 7382
- [83] J. E. Demuth, N. J. DiNardo and G. S. Cargill III, *Phys. Rev. Lett.* **50** (1983) 1373
- [84] W. Oed, H. Lindner, U. Starke, K. Heinz, K. Müller and J. B. Pendry, *Surf. Sci.* **224** (1989) 179